Copyright Warning & Restrictions

The copyright law of the United States (Title 17, United States Code) governs the making of photocopies or other reproductions of copyrighted material.

Under certain conditions specified in the law, libraries and archives are authorized to furnish a photocopy or other reproduction. One of these specified conditions is that the photocopy or reproduction is not to be "used for any purpose other than private study, scholarship, or research." If a, user makes a request for, or later uses, a photocopy or reproduction for purposes in excess of "fair use" that user may be liable for copyright infringement,

This institution reserves the right to refuse to accept a copying order if, in its judgment, fulfillment of the order would involve violation of copyright law.

Please Note: The author retains the copyright while the New Jersey Institute of Technology reserves the right to distribute this thesis or dissertation

Printing note: If you do not wish to print this page, then select "Pages from: first page # to: last page #" on the print dialog screen

NJIT New Jersey's Science & Technology University

The Van Houten library has removed some of the personal information and all signatures from the approval page and biographical sketches of theses and dissertations in order to protect the identity of NJIT graduates and faculty.

ABSTRACT

FIRST-PRINCIPLES DENSITY FUNCTIONAL THEORY STUDIES ON PEROVSKITE MATERIALS

by
Aneer Lamichhane

Perovskites are a family of materials with a diverse combination of different elements. As a consequence, they exhibit numerous functionalities such as pyroelectric, piezoelectric, ferroelectric, and ferromagnetic with applications in photovoltaic cells, LEDs, superconductivity, colossal magneto-resistance, and topological insulators. After 2009, perovskites have gained notoriety as suitable materials for solar cells and alternative candidates to silicon-based conventional solar cells. Generally, oxide perovskites exhibit good dielectric properties, halide perovskites display good photonic qualities, and chalcogenide perovskites are used in applications in solid-state lighting, sensing, and energy harvesting. In this dissertation, various types of perovskites ranging from oxide to halide are investigated along with their structural, elastic, electronic, and optical properties. The mode of study is the first-principles calculations performed with density functional theory, implemented in the VASP (The Vienna Ab initio Simulation Package) codes. Energy gap and refractive index are two critical properties, whose prior knowledge is required for designing optoelectronic devices. A model is developed by which these two quantities are correlated in both oxide and halide perovskites. This model is consistent with other well-established models and predicts the refractive index with greater accuracy. A comprehensive study of alkaline earth metal zirconate perovskites $CaZrO_3$, $SrZrO_3$ and $BaZrO_3$ is performed. The effect of the cation size on their overall properties is analyzed using both standard and hybrid functionals. Moreover, this study also shows the comparative efficacy between standard and hybrid functionals. The bond strengths in these zirconate perovskites are studied using the concept of the charge flow, which arises due to the coupling between lattice displacement and electrostatic field. In performing the

study of optical properties, the value of the dimensionless constant in the Penn model is determined to be 0.86. Based on the study of phonons, it is noted that these zirconate perovskites are suitable for thermal coating materials. Likewise, the structural phase study in halide perovskite, $CsPbBr_3$, has predicted the transition temperature as well as the order of phase, in accord with the experimental results. Its two-dimensional (2D) counterparts, Cs_2PbBr_4 and $CsPb_2Br_5$, are also studied in parallel with $CsPbBr_3$. Their higher exciton binding energy is explained based on the screening factor. One of the major problems in perovskite-based solar cells is their unpredictability in behavior due to external conditions such as moisture, temperature, etc. In order to address such an issue, it is better to maintain the system under isosymmetric stress. A detailed concept of imposing isosymmetric stress with hydrostatic compression is discussed. This notion is applied to various cubic halide perovskites, ABX_3 ($A = K, Rb, Cs$;$B = Ge, Sn, Pb$ and $X = Cl, Br, I$). The influence of cation-anion exchange, together with the effect of spin-orbit coupling, is studied.

FIRST-PRINCIPLES DENSITY FUNCTIONAL THEORY STUDIES ON PEROVSKITE MATERIALS

by
Aneer Lamichhane

A Dissertation
Submitted to the Faculty of
New Jersey Institute of Technology
in Partial Fulfillment of the Requirements for the Degree of
Doctor of Philosophy in Materials Science and Engineering-
Materials Science Option

Department of Physics

May 2021

Copyright © 2021 by Aneer Lamichhane

ALL RIGHTS RESERVED

APPROVAL PAGE

FIRST-PRINCIPLES DENSITY FUNCTIONAL THEORY STUDIES ON PEROVSKITE MATERIALS

Aneer Lamichhane

Dr. Nuggehalli M. Ravindra, Dissertation Advisor — Date
Professor of Physics, NJIT

Dr. Anthony Fiory, Committee Member — Date
Consultant (Former Research Professor of Physics), NJIT

Dr. Cristiano Dias, Committee Member — Date
Associate Professor of Physics, NJIT

Dr. Keun Hyuk Ahn, Committee Member — Date
Associate Professor of Physics, NJIT

Dr. Oktay H. Gokce, Committee Member — Date
Senior University Lecturer of Physics, NJIT

Dr. Chiranjivi Lamsal, Committee Member — Date
Assistant Professor of Physics, SUNY, Plattsburgh, NY

BIOGRAPHICAL SKETCH

Author: Aneer Lamichhane

Degree: Doctor of Philosophy

Date: May 2021

Undergraduate and Graduate Education:

- Doctor of Philosophy in Materials Science and Engineering-
  Materials Science Option,
  New Jersey Institute of Technology, Newark, NJ, 2021
- Master of Science in Physics,
  Bowling Green State University, Bowling Green, OH, 2018
- Master of Science (Technology) in Technomathematics,
  Lappeenranta University of Technology, Lappeenranta, Finland, 2015
- Master of Science in Physics,
  Tribhuvan University, Kathmandu, Nepal, 2010
- Bachelor of Science in Physics and Bachelor of Art in Mathematics,
  Tribhuvan University, Kathmandu, Nepal, 2006

Major: Materials Science and Engineering-Materials Science Option

Presentations and Publications:

Aneer Lamichhane, N.M. Ravindra, "First-principles study of cubic alkaline-earth metal zirconate perovskites," *Journal of Physics Communications, IOP Publishing LtD*, 25 February, 2021.

Aneer Lamichhane, N.M. Ravindra, "Isosymmetric compression of cubic halide perovskites ABX_3 ($A = K, Rb, Cs$;$B = Ge, Sn, Pb$ and $X = Cl, Br, I$)- influence of cation-anion exchange:a first principle study," *SN Applied Sciences, Springer Link*, 18 January, 2021.

Aneer Lamichhane, N.M. Ravindra, "Cesium Lead Bromides- Structural, Electronic and Optical properties," *TMS Annual Meeting and Exhibition*, 25 September, 2020.

Aneer Lamichhane, N.M. Ravindra, "Energy Gap- Refractive Index Relations in Perovskites," *Materials,*, 19 April, 2020.

Keshav Bashyal, Christopher K Pyles, Sajjad Afroosheh, Aneer Lamichhane, Alexey T Zayak , "Empirical optimization of DFT+U and HSE for the band structure of *ZnO*," *Journal of Physics: Condensed Matter, IOP Publishing LtD*, 12 January, 2018.

Dedicated to my beloved daughter, Aayushi

ACKNOWLEDGMENT

I express my sincere gratitude to my advisor Dr. Nuggehalli M. Ravindra for providing me an opportunity in his research group. This research would not have been completed without his guidance, advice, and benevolence. The lessons that I have learned under his guardianship will boost my scientific career.

I thank Dr. Keun Hyuk Ahn, Dr. Cristiano Dias, Dr. Oktay H Gokce, Dr. Anthony Fiory, and Dr. Chiranjivi Lamsal for serving as my dissertation committee members and providing valuable suggestions and comments on the dissertation manuscript.

I am especially thankful to the Department of Physics, NJIT for awarding me the teaching assistantship throughout my study and research.

I would like to thank Ms. Clarisa Gonzalez-Lenahan, Associate Director of Graduate Studies, and Dr. Sotirios G. Ziavras, Vice Provost for Graduate Studies and Dean of the Graduate Faculty for the improvement and formatting of this dissertation.

I acknowledge with thanks the support of the Academic and Research Computing Systems, NJIT, especially, Dr. Glenn (Gedaliah) Wolosh and Dr. Kevin Walsh. I express my thanks to Dr. Alexey T. Zayak and Dr. Elizabeth A. Nowadnick.

My deepest gratitude goes to my father, Ambika P. Lamichhane; mother, Savitra Pokharel Lamichhane; and brother, Saneer Lamichhane. I am thankful to my wife, Bunu Shrestha Lamichhane for supporting me and taking care of our lovely daughter, Aayushi Lamichhane.

TABLE OF CONTENTS

Chapter **Page**

TABLE OF CONTENTS
(Continued)

Chapter Page

TABLE OF CONTENTS
(Continued)

Chapter **Page**

LIST OF TABLES

LIST OF FIGURES

Figure **Page**

LIST OF FIGURES
(Continued)

Figure **Page**

CHAPTER 1

INTRODUCTION

1.1 Survey of Computational Materials Science

Materials science and engineering is an important branch of today's science. One of the major objectives of this discipline is to facilitate a vast acceleration in generating new and advanced materials to meet the demands on energy. The evolution of modern materials science can find its root in crystallography. The early credit goes to mineralogists for finding that many crystals are anisotropic to light. After the discovery of X-rays in 1895 by Wilhelm Röntgen [1], there was a paradigm shift in crystallography. The physical measurements of the geometry of a crystal were replaced by the sophisticated technique of X-ray diffraction. The impact of the X-ray diffraction technique was so revolutionary in the twentieth century that a large number of Nobel prizes were awarded to scientists for their work based on this technique.

Max von Laue was awarded the 1914 Nobel Prize for his discovery of X-ray diffraction in crystals [2, 3]. The work of Paul Ewald on, "The optical properties of a medium consisting of a regular arrangement of isotropic resonators" [4], could be taken as the precursor for Laue to show that the wavelength of X-rays matched the spacing of atoms in the crystals. Despite the success of a crystal as a three-dimensional diffraction grating for X-rays, there was a problem in determining the correct phase of the diffracted X-rays, which hindered in determining space lattices. Later, this difficulty was solved by the father and son team of W.H. Bragg and W.L. Bragg by treating the discovery of Laue's diffraction phenomenon as a reflection by the successive parallel planes within a crystal [5]. The duo proposed the famous Bragg's law- $2dsin\theta = n\lambda$, where d is the inter-planar distance, λ is the incident wavelength and θ is the glancing angle [6]. They were awarded the 1915 Nobel Prize in physics. Bragg's law has tremendous significance

in determining the crystal structure, together with the bond length, lattice parameters, etc. Moreover, this law explains the variation of properties within polymorphs as a result of the relative juxtaposition of atoms within them. In his famous book, "Concerning the Nature of Things", W.H. Bragg wrote, "The properties of metals must depend, in the first place, on the properties of individual atoms, and, in the second place on the atomic arrangement, which is in effect the state of crystallization [7]." After the establishment of the diffraction of X-rays within a crystal, scientists such as Davisson and Germer performed a diffraction experiment using electrons in a single crystal and Thompson did the same experiment with a crystalline film [8]. These experiments were successful in determining the periodic structure of the crystal along with the wave-particle duality of the electrons. The success of the diffraction experiment in determining the structure was amplified by Rosalind Franklin, who discovered the double-helical structure of the DNA molecule, using X-ray diffraction [9].

Solid materials are generally modelled as densely packed atoms, linked together with an interatomic bond. Based on the nature of the interatomic bond, solid materials are not only classified into ionic, covalent or metallic but also their properties such as mechanical, electrical, optical, thermal and magnetic are dependent on it. Historically, the study of heat capacity bears tremendous significance. In the year 1819, two French scientists Pierre Louis Dulong and Alexis Therese Petit had found experimentally that the molar heat capacity of a large number of elements was constant, approximately three times the universal gas constant [10]. A proper theory of heat capacity was formulated by Albert Einstein, 87 years after the formation of Dulong and Petit law. Einstein assumed that the heat capacity of a solid is attributed to vibrations in the atom with the same frequency. This theory was partially successful in predicting the upper limit of the heat capacity, to what was found by Dulong and Petit, and the lower limit to zero, in accordance with the third law of thermodynamics. One of the major shortcomings of Einstein's theory is the exponential variation of heat capacity, instead of linear behavior at low temperature. In

the year 1912, Debye proposed another theory of heat capacity, which agrees not only with Dulong and Petit's law and third law of thermodynamics at the upper and lower temperature respectively, but shows linear variation at the low temperature [11]. However, this theory fails at intermediate temperatures. Einstein modelled his solid as densely packed atoms, vibrating as three-dimensional oscillators whereas Debye modelled his solid as an isotropic continuum medium. These two theories, though successful, have their own limitations- the former valued the properties of atoms and the latter valued the arrangement of atoms in the solid. This kind of issue- properties versus arrangement can also be seen in the Sommerfeld model of metals.

The success of X-ray crystallography and the issue of "properties versus arrangement" forces physicists to consider solid not only as densely packed atoms but also as a periodic arrangement of atoms within it. This picture of solid is realistic in two senses- first, atoms in the solid crystallize in a periodic fashion at low temperature and pressure, and second, the quantum mechanical treatment of solid is plausible only when the Schrödinger equation contains a periodic potential. Moreover, this integration of arrangement allows the classification of solid into crystalline and amorphous, different from the previous classification based on the bonds. In the year 1940, the study of solid then emerged as a separate branch of physics called solid-state physics [12]. As the periodicity allows mathematical modeling accessible, this branch has evolved and diversified quickly since its establishment. Physicists did not limit their study only to solid materials. They have been studying other states such as liquid state, plasma, etc, in parallel with the solid-state. As a result, a separate branch of physics, known as condensed matter physics emerged between the years 1970-80 [13]. This branch, being a superset of solid-state physics, provides a framework for an understanding of the multi-particle systems interacting with well-defined forces. Due to several breakthroughs, this branch is so versatile and diverse that it interacts with other disciplines of science, making it an interdisciplinary subject, with a common name as materials science.

The role of computers in solving mathematical models has gained attention after the second world war. Many-particle interaction involves a series of complex mathematical equations that are cumbersome to solve without the aid of a computer. Further, the application of Schrödinger equation to solve many-particle problems is in practice a difficult task. The use of computer simulation in materials science is pronounced for computing the properties as well as visualizing and mimicking the structure of the materials. Likewise, the cutting edge developments in software and computational tools facilitated theoretical modeling in materials science with great ease. Recent innovations in developing powerful computers and supercomputers have revolutionized the implementation of theories such as Monte Carlo simulation, density functional theory (DFT), etc, in predicting the ideal properties of materials. The formulation of DFT by Hohenberg and Sham, is one of the state-of-the-art methods to solve many-particle problems and calculate electronic structure with ease, even using single computer [14]. Several computer simulation packages such as VASP, ABINIT, SIESTA, etc, are widely used in modeling materials in the atomic domain and predicting their electronic, optical, vibrational, thermal, and magnetic properties. As a result, there is growing interest in materials simulation and a large number of findings are published with the integration of computers in materials science research. Today, computational materials science has evolved from materials science, making it as one of the prime branches of science.

Computational materials science provides a platform for a clean and green way of conducting research, where there is no need for real material and its testing. The functionalities of the materials can be calculated merely from theoretical models. It can also work in the reverse sense, that is, based on the required functionalities, new materials can be created. The triumph of computational materials science lies not only to simulate the physics of materials but also to predict new materials. A few years ago, Ceder et al. were successful in discovering a number of new materials, using computational methods [15]. Their powerful simulation techniques have opened the door for the materials revolution.

Therefore, the emerging computer materials science has the power to deal with upcoming challenges such as energy crisis, efficient production of clean energy, downsizing the excessive use of rare earth elements, and advanced materials production.

1.2 Materials of Study- Perovskites

In 1839, German geologist, Gustav Rose discovered a mineral composed of $CaTiO_3$ in the Ural Mountains of Russia. Extensive study of this mineral was further carried out by another Russian mineralogist, named Count Lev Alexevich von Perovski [16]. In his honor, this mineral is called perovskites. Historically, materials whose structure resembles the structure of $CaTiO_3$ are known as perovskites. The structure of $CaTiO_3$ is quite unstable at room temperature and can distort to a lower symmetry structure. Therefore, it is usually good to consider $SrTiO_3$ as a basis structure for perovskites.

Table 1.1 Structural Configuration of Cubic Perovskites

Atom	*Coordination*	*Wyckoff − Positions*			*Coordinates*
		Site	*Multiplicity*	*Symmetry*	
A	12	*a*	1	$m-3m$	$(0.0, 0.0, 0.0)$
B	6	*b*	1	$m-3m$	$(0.5, 0.5, 0.5)$
X	2	*c*	3	$4/mm.m$	$(0.5, 0.0, 0.5)$ $(0.5, 0.0, 0.5)$ $(0.5, 0.0, 0.5)$

The molecular formula for perovskite compounds is ABX_3, where A and B are cations and X is an anion. Based on X anion, perovskites can be named as oxide perovskite (X=O) and halide perovskite (X=Cl, Br, I). Again, the halide perovskite system can further be classified into alkali halide perovskite and organo metal perovskite (popularly known as hybrid perovskite) depending on the cation A. The cation A is usually larger than the cation B and their pairing can be understood by the charge balancing or stoichiometry of perovskite. In the case of oxide perovskite, three combinations $A^{+1}B^{+5}O_3^{-2}$, $A^{+2}B^{+4}O_3^{-2}$ and $A^{+3}B^{+3}O_3^{-2}$ are usually permitted and for halide perovskite, the most common pairing is $A^{+1}B^{+2}X_3^{-1}$. The bonding <A−X> is ionic and <B−X> is mixed, both ionic and

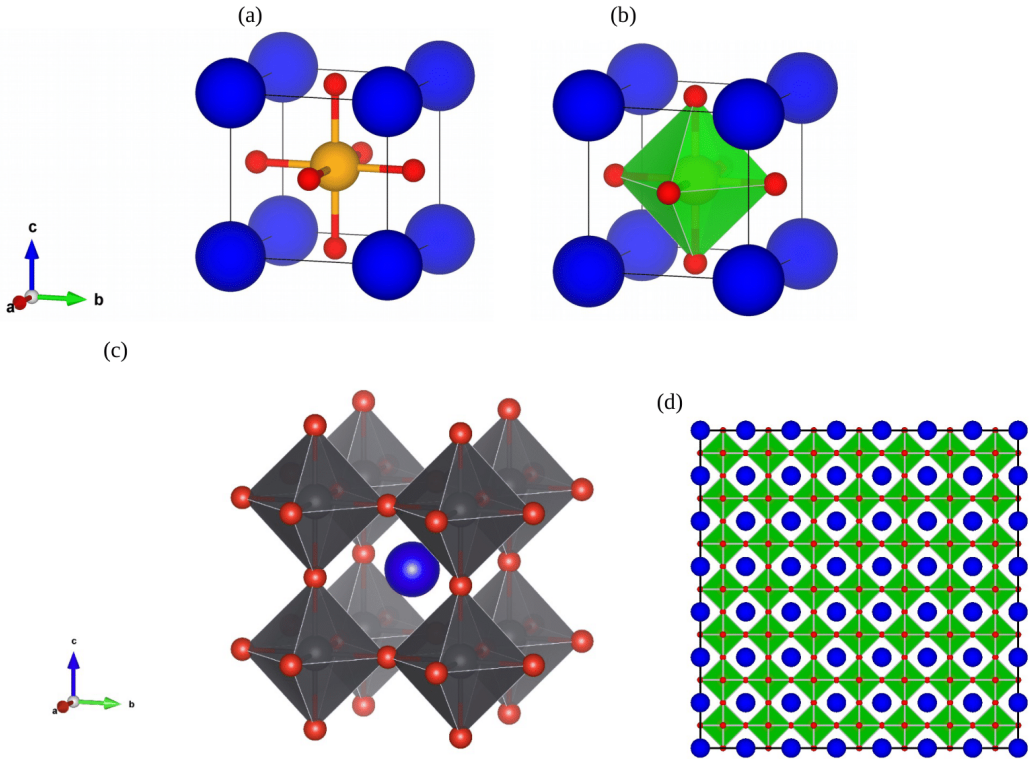

Figure 1.1 The cubic structure of perovskite ABX_3. (a) The purple, yellow and red atoms represent A, B and X, respectively, where B is at $(0.5, 0.5, 0.5)$; (b) The octahedron cage $[BX_6]$; (c) A is at $(0.5, 0.5, 0.5)$ and (d) The cornor sharing X atoms of octahedral cages forming networks- a top view.

covalent. The ideal crystal structure of perovskite is cubic, which is a high symmetric structure (Space group $Pm\bar{3}m$). The high symmetry structures are shown in Figure 1.1 and the corresponding structural parameters are highlighted in Table 5.1. This cubic structure can be thought of as a body-centered cubic (BCC) structure in terms of A and B, and a face-centered cubic (FCC) structure in terms of B and X. The position of A and B can be either $(1/2, 1/2, 1/2)$ or $(0, 0, 0)$ and X sits as $(0, 1/2, 1/2)$, $(1/2, 0, 1/2)$ and $(1/2, 1/2, 0)$. However, by convention or in most cases, the position of A is taken as $(1/2, 1/2, 1/2)$. Independent of the position of A and B, the coordination number of cation A is 12 and B is 6, thus forming the polyhedron $[\mathrm{B{-}X}]_6$ as octahedron and $[\mathrm{A{-}X}]_{12}$ as cuboctahedron. Further, the dimensionality (2D, 1D) in perovskite is governed by its octahedral cages. In 1D, these octahedral cages are discrete and in 2D, they are connected to one another

forming a layer, and intercalated atoms act as a spacer between any two layers, as illustrated in Figure 1.2. This kind of layered perovskites has a formula $A_{n-1}B_nX_{3n+1}$, n being the number of layers. The layered perovskites are common in hybrid perovskites, where large size organic cation A do not fit into the octahedral structure and acts as a barrier or spacer between 3D structures.

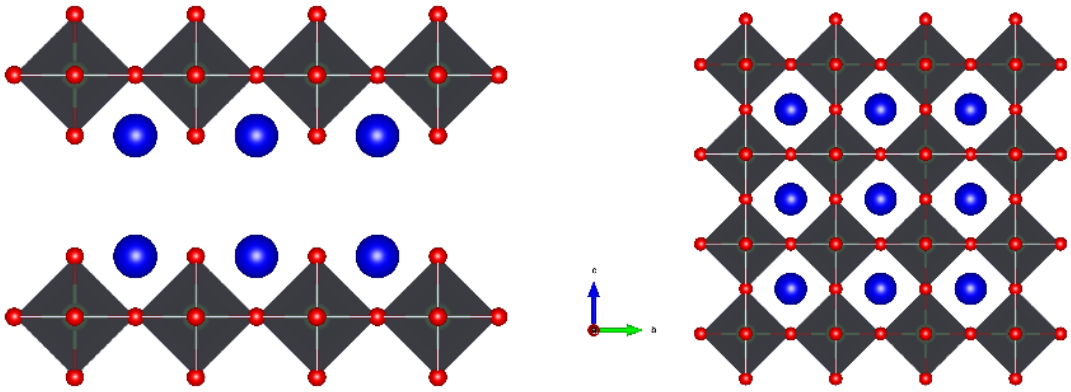

Figure 1.2 Illustration showing the role of intercalated atoms as a spacer between the layer of octahedral cages in 2D (left) perovskites whereas the corner atoms link octahedral cages in all directions in 3D (right) perovskites.

The cubic structure is a perfect or high symmetry structure. Yet, a few cubic structured perovskite compounds are stable below room temperature. This is because the structure of perovskites is sensitive to external conditions such as moisture, temperature, pressure, etc. As a result, high symmetry structure distorts to lower symmetry to gain stability. The distortion from the cubic structure, mostly accompanied by octahedral rotation, leads to a phase transition, resulting in lower symmetry structures such as tetragonal, orthorhombic, and rhombohedral. One classic way of understanding the lattice distortion in ABX_3 is the size effect, that is, the variation in A, B, X atoms in the geometry of its cell. This relation is quantified by the Goldschmidt tolerance factor [17] (t), implying that this value for the ideal cubic structure is one. Mathematically, $t = \frac{(r_A+r_X)}{\sqrt{2}(r_B+r_X)}$, where r_A, r_B, and r_X are the ionic radius of A, B and X. Mostly, the oxide perovskites show cubic symmetry for $0.89 < t < 1$ and halide perovskites for $0.85 < t < 1$ [18, 19]. The properties of perovskite are dependent on its octahedral cages formed by B and X and the role of A is

merely for charge neutrality. The variation in size A results in a change in those properties by distorting the octahedral cages. For $t < 1$ (smaller A ion), the tilting of octahedral cage results in lower symmetry structure such as orthorhombic and rhombohedral, and for $t > 1$ (larger A ion), it results in hexagonal closed packed structures. Besides stability and governing symmetry, the variation of A cation has been widely used in tuning the properties such as band gap, refractive index, etc. It has also been noticed that the suitable change in A cation reduces the structure into modular form, resulting in quantum confinement and thereby dimensional reduction to the two-dimensional (2D) structure. The tolerance factor is not sufficient and an additional condition called the octahedron factor (μ) [19] should be incorporated to account for the stability of the perovskite compounds. This condition conveys that, for the formation of an octahedron, the minimum radius of B cation should be roughly $(\sqrt{2}-1)$ times the radius of X anion, that is, $\mu = r_B/r_X \geq (\sqrt{2}-1)$ and the upper limit is somewhere $(\sqrt{3}-1)$ [19]. The combination of both tolerance factor and octahedron factor can predict the formability of many perovskites. However, these two conditions are necessary but not sufficient conditions. Besides the size effect, the other cause of instability, especially in transition metal perovskites (such as $CsMnF_4$, $LaMnO_3$, $KCuF_3$, $KCrF_3$) could be Jahn-Teller distortion [20]. It is the electronic instability where the octahedron distorts, due to the lowering of the degeneracy and energy. The perovskites with B cation in configuration except for d^3, d^5 (high spin), d^8 (high/low spin), d^6 (low spin), and d^{10} show Jahn-Teller distortion [21]. The other internal cause of distortion could be stoichiometry or composition mismatch (for e.g., $A_{1-x}BO_{3-x}$), defect, void, doping, etc. Moreover, as stated earlier, perovskites are highly sensitive to external stimuli such as pressure, temperature, moisture, humidity, etc, which also accounts for the instability of the structure.

The structural distortions of perovskites from their cubic phase can be explained based on ionic displacements and octahedral tiltings. The tilting of the $[BX_6]$ octahedra about its symmetry axes arises due to compensation of smaller A cation, by optimizing

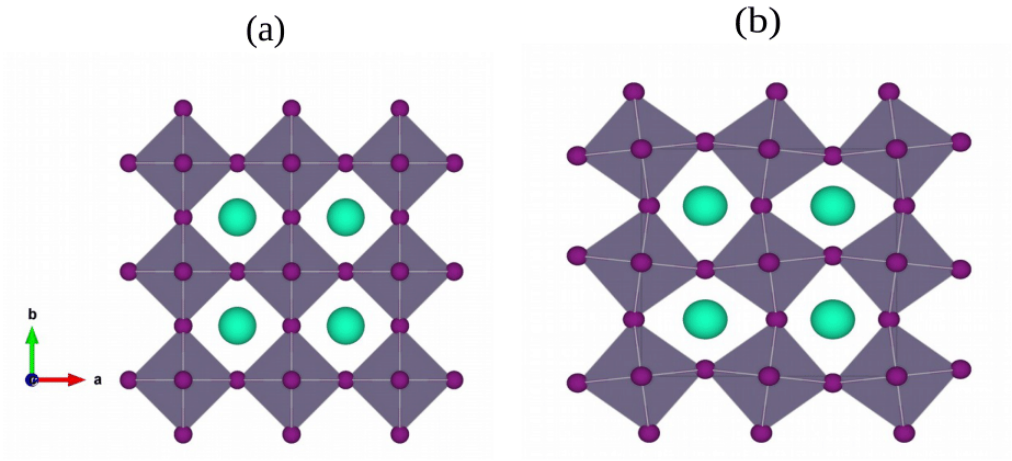

Figure 1.3 (a) The archetype high symmetry cubic phase $a^0a^0a^0$ and (b) the distorted tetragonal phase $a^0a^0c^+$.

$< A-X >$ bonding. In other words, the octahedral tilting occurs when $t < 1$, yielding tensile $< A-X >$ bond and compressive $< B-X >$ bond. In 1972, Glazer developed a standard notation of a tilt system, where $[BX_6]$ octahedra rotate in the orthogonal axes coincident with the three axes of the standard cubic unit cell [22]. In his notation, the letters a, b and c represent unequal tilt about the x, y and z axes; the superscripts '0', '+' and '−' indicate no tilt, in-phase and out of-phase rotation with respect to the first octahedral layer, respectively. For instance, the tilt system $a^0b^-c^+$ denotes that there is no tilt about the x-axis of standard cubic perovskite and unequal tilt about the y-axis and the z-axis having out of phase and in phase rotation respectively. The cubic perovskite is therefore represented as an archetype $a^0a^0a^0$ and the tilting $a^0a^0c^+$ describes the in-phase rotation about the z-axis, yielding the tetragonal phase with space group $P4/mbm$ (127), as illustrated in Figure 1.3. Glazer has identified 23 tilt systems comprising 15 different space groups, which was later corrected by Howard and Stokes [23] to 15 tilt systems with space groups. Using group-theory, they have shown that out of 23 tilt systems, 8 are redundant due to higher symmetry than the corresponding space groups and only 15 tilt systems can occur in real perovskites. These are shown in Table 1.2, taken from [24], where numbers

1, 3, 5, 8, 10, 12, 13, 14, 16, 17, 19, 20, 21, 22 and 23 are the basis for any tilts in real perovskites, as found by Howard and Stokes.

Table 1.2 The Glazer Tilt Systems Found in Perovskites with Symmetry

Number	*Tilting System*	*Symmetry*	*Number*	*Tilting System*	*Symmetry*
3-*tilts*			2-*tilts*		
1	$a^+b^+c^+$	$Immm$ (71)	15	$a^0b^+c^+$	$Immm$ (71)
2	$a^+b^+b^+$	$Immm$ (71)	16	$a^0b^+b^+$	$I4/mmm$ (139)
3	$a^+a^+a^+$	$Im\bar{3}$ (204)	17	$a^0b^+c^-$	$Cmcm$ (63)
4	$a^+b^+c^-$	$Pmmn$ (59)	18	$a^0b^+b^-$	$Cmcm$ (63)
5	$a^+b^+c^-$	$P4_2/nmc$ (137)	19	$a^0b^-c^-$	$C2/m$ (12)
6	$a^+b^+b^-$	$Pmmn$ (59)	20	$a^0b^-b^-$	$Imma$ (74)
7	$a^+a^+a^-$	$P4_2/nmc$ (137)	1-*tilt*		
8	$a^+b^-c^-$	$P2_1/m$ (11)	21	$a^0a^0c^+$	$P4/mbm$ (127)
9	$a^+a^-c^-$	$P2_1/m$ (11)	22	$a^0a^0c^-$	$I4/mcm$ (140)
10	$a^+b^-b^-$	$Pnma$ (62)	0-*tilt*		
11	$a^+a^-a^-$	$Pnma$ (62)	23	$a^0a^0a^0$	$Pm\bar{3}m$ (221)
12	$a^-b^-c^-$	$P\bar{1}$ (2)			
13	$a^-b^-b^-$	$C2/c$ (15)			
14	$a^-a^-a^-$	$R\bar{3}c$ (167)			

Based on the criteria of tolerance factor and octahedron factor, a large number of combinations of A, B, and X can be incorporated into the perovskite structure, making it an extremely diverse family. Perovskite family includes all possible materials with character ranging from insulator, semiconductor, metal, and superconductor. As a consequence, perovskites exhibit distinct variations in electronic properties, electrical properties, mechanical properties, optical properties, dielectric properties, superconductivity, magnetic properties, catalytic properties, etc. Secondly, one can tune these properties not only by varying A, B, and X across the periodic table but also doping A and B site ($A'_yA_{1-y}BX_3/AB'_yB_{1-y}X_3$) with a suitable substitution. Moreover, the structural reformation and phase transition can further tune these properties. Likewise, the change in dimensionality (1D, 2D) can yield different properties than its bulk (3D) counterparts. The chemically reduced 2D perovskites have molecular formula $A'_yA_{n-1}B_nX_{3n+1}$, where y is 2 for monovalent A' cation and 1 for divalent A' cation and n is the number of layers.

In a 2D structure, A' sits in the intercalated regions and acts as a separator between two octahedral cages. The 2D structure not only gives a high stability structure but also yields a plethora of properties simply by varying A' and the number of layers. This is why perovskites are fascinating materials to study as they manifest a wealth of properties, which can be tuned and varied easily. For practical applications, perovskites are used in sensors, fuel cells, electrodes, solar cells, memory devices, LEDs, lasers, and other optoelectronic devices [25]. Among several applications, perovskites as solar cells are the most important ones for the upcoming decades. Their light-harvesting capabilities have been increased from 3.8% in 2009 to over 25% in 2020 [26, 27]. It was projected that perovskite solar cells will replace silicon solar cells and occupy the market worth billions of dollars in the upcoming decades. Moreover, the synthesis and fabrication costs of perovskite solar cells are comparatively inexpensive. Despite these intriguing qualities, the commercial success of these cells is hindered by instability, degradation, durability, unpredictability, and toxicity. The usage of some perovskite materials is shown in Table 1.3, taken from [28].

Table 1.3 Perovskite Materials and Their Properties and Uses

Materials	*Properties*	*Applications*
$BaTiO_3$	*Dielectric*	*Capacitor, Sensor*
$(Ba,Sr)TiO_3$	*Pyroelectric*	*Pyrodetector*
$PbTiO_3$	*Pyroelectric* *Piezoelectric*	*Pyrodetector* *Acoustic transducer*
$Pb(Zr,Ti)O_3$	*Dielectric* *Piezoelectric*	*Nonvolatile memory*, *Pyrodetector*, *Surface acoustic wave device*
$LiNbO_3$	*Piezoelectric*	*Pyrodetector* *Surface acoustic wave device*
$K(Ta,Nb)O_3$	*Pyroelectric* *Electro − optic*	*Pyrodetector* *Waveguide device* *frequencydoubler*
$Pb(Mg_{1/3}Nb_{2/3})O_3$	*Dielectric*	*Memory* *Capacitor*

1.3 Organization

The dissertation is based on the theoretical computations of perovskites using DFT and implemented with VASP codes [29, 30]. The brief description of VASP is provided in the appendix section. These computations rely on various simulation techniques, developed as valid concepts and models, and are integrated with powerful supercomputers for high throughput results. After that, the results are refined and post-processed with several tools before tallying with the corresponding experimental results. In the absence of experimental results, they are used to develop a model, whose validity is tested on different but analogous materials. The remaining part of the dissertation is organized with Chapters 2, 3, 4, 5, 6 and conclusions. Chapter 2 presents the theoretical aspects of DFT, along with a discussion of some key concepts. Chapter 3 provides a theoretical model for band gap and refractive index relations. Chapter 4 is based on the study of structural, elastic, electronic, and optical properties of some alkaline earth zirconate perovskites. Chapter 5 describes the *Cs-Pb-Br* variants and their 2D counterparts. Chapter 6 presents the study of cubic halide perovskites and the effect of isosymmetric compression on their structures. The conclusions section is presented at the end of the dissertation.

CHAPTER 2

METHODOLOGY AND THEORY

2.1 Fundamentals of the Density Functional Theory

2.1.1 Electronic Structure Calculations

The electronic structure calculations of a material are the central task for atomistic simulations. They refer to calculations of the state of electronic motion around stationary nuclei. In a quantum-mechanical sense, they represent calculations of the wave functions or eigenstates and corresponding eigenvalues or energies of electrons. Almost every property of a material can be formulated after knowing its electronic structure. For instance, the knowledge of electronic ground states gives information on stability, vibrational properties with several thermal properties, elastic properties, transport phenomena such as diffusivity, ionic conductivity, dielectric properties, etc. The knowledge of electronic excited states provides information on electronic transport phenomena, optical properties, etc. These properties are known as ground-state properties and excited-state properties. Therefore, it is worthwhile to accurately calculate the electronic structures. Several advanced models and theories have been formulated after the discovery of the electron.

In 1897, J.J. Thomson discovered a negatively charged particle called the electron, while working at the Cavendish Laboratory in Cambridge. He described the electronic structure with a ”Plum pudding model” [31]. This model was unsuccessful and refuted by his own student Ernest Rutherford. In 1910, Ernest Rutherford proposed a planetary model in which the atom contains a central positive charge called a nucleus and electrons revolve around the nucleus making the atom electrically neutral [32]. One of the major pitfalls of the Rutherford model was the violation of Maxwell’s law that the accelerated charged particle radiates electromagnetic radiation and, as a consequence, electrons revolving around the nucleus eventually collapse into the nucleus, making the atom unstable. The

drawback of the Rutherford model was solved by Neil Bohr, who in the year 1913, proposed that the electron revolves only in the allowed orbit, and in such orbit, it does not emit radiation. Bohr's postulation is based on the fact that classical mechanics and electromagnetism are inadequate to explain physics at the atomic scale. Further, this postulate is justified by Planck's theory of black body radiation. The verification of energy absorbed/emitted by an electron attributing it to the difference in the energy levels of orbits yielded a strong foundation for the development of quantum mechanics [33]. The electron soon became the testing grounds for quantum physicists. Whether the search for electronic structure gave birth to quantum mechanics or quantum mechanics is founded to search electronic structure continues to be a paradox. Despite the success of the Bohr model for hydrogen and hydrogen-like atoms, it has several drawbacks and failed for poly-atomic structures. In 1925, Werner Heisenberg formulated quantum mechanics in terms of matrices. After one year, Schrödinger formulated the mathematical language, in which the electron revolving in the orbit is treated as a de Broglie wave and the probability for an electron in a given orbit at a given time is described by mathematical equations containing the wave function. The Schrödinger equation was used successfully in computing the electronic structure of multi-electronic atoms (Heitler and London, 1927) and poly-atomic systems (Bloch, 1928) [34].

However, the shortcomings of Schrödinger lie in the difficulty to solve many-body systems. This makes it impractical to use for real applications. As an example, it requires 66 equations to compute the electronic structure of CO_2, if one neglects nuclear dynamics and electronic spin. In other words, the electronic configuration is represented by the wave function $\psi(r_1, r_2, ..., r_{66})$ making the Schrödinger equation as a 66 dimensional problem. Further, these electrons in space interact among each other making it not only difficult to understand the two body Coulomb interaction but also difficult to separate the wave function, i.e., $\psi(r_1, r_2, ..., r_{66}) \neq \psi(r_1) * \psi(r_2) * ... * \psi(r_{66})$. The exact solution, if found, would have an equation in 66 degrees of freedom. This kind of difficulty is

widely known as quantum many-body problem and to seek the solution of Schrödinger equation in many-body problem must resort to some approximations. In 1927, Max Born and J. Robert Oppenheimer proposed an approximation that atomic nuclei motion and electron motion can be treated separately due to the fact that nuclei are much heavier than electrons [34]. Born-Oppenheimer approximation, therefore, reduces the nuclei factor from the Hamiltonian function and treats the nuclei as a stationary source of an electrostatic field. The next approximation is the Hartree method, which assumes a single electron assumption by considering the same interaction between any two electrons [34]. The Hartree-Fock is another approximation which separates the many-body wave function as the combination of some standard base functions, i.e., $\psi(r_1, r_2, ..., r_N) = \phi(r_1) * \phi(r_2) * ... * \phi(r_N)$, where one can incorporate the antisymmetric conditions of electron wave functions ($\phi(r_1) * \phi(r_2) * ... * \phi(r_N) = -\phi(r_2) * \phi(r_1) * ... * \phi(r_N)$), using Slater determinant [34]. The density functional theory (DFT) is another intriguing approximation that substitutes many-body wave function by electron probability density function. This approximation reduces the N-dimensional problem to a 3-dimensional problem as the electron probability density function is the function of spatial coordinates only. DFT was formulated by Hohenberg-Kohn in 1964 [35] and this theory remained dormant till 1990. After the advent of high performance supercomputers, DFT led to a rapid paradigm shift in material science research, providing the alternate means of investigation, instead of using traditional experimental methods. Today, DFT is a standard procedure in the atomistic simulation of materials.

2.1.2 Many-Body Problem

Many body problem consists of a set of atomic nuclei and electrons interacting via Coulomb forces. The Hamiltonian of such system can be expressed as,

$$H = -\sum_I \frac{\hbar^2}{2M_I}\nabla^2_{R_I} - \sum_i \frac{\hbar^2}{2m_e}\nabla^2_{r_i} + \frac{1}{2}\sum_{I,J_{(I\neq J)}} \frac{Z_I Z_J e^2}{|R_I - R_J|} + \frac{1}{2}\sum_{i,j_{(i\neq j)}} \frac{e^2}{|r_i - r_j|} - \sum_{I,i_{(I\neq i)}} \frac{Z_I e^2}{|R_I - r_i|} \tag{2.1}$$

where, I and J run on nuclei; Z, M and R represent atomic number, nuclear mass and position respectively and correspondingly lower cases for electrons. The first term in the right hand side of Equation (2.1) is the kinetic energy of nuclei, the second term is the kinetic energy of electrons, the third term is the potential energy of the nucleus-nucleus interaction, the fourth term is the potential energy of the electron-electron interaction and the last term is the potential energy of the electron-nucleus interaction. Let us suppose that $\phi(R_I; r_i)$ is the total wave function of the system, then the system is known if one can find the solution of the time-independent Schrödinger equation,

$$H\phi(R_I; r_i) = E\phi(R_I; r_i) \tag{2.2}$$

The wave function $\phi(R_I; r_i)$ can be separated into the wave function of the nuclei (Π) and the wave function of the electrons in the potential of the stationary nuclei (Ω),

$$\phi(R_I; r_i) = \Pi(R_I)\Omega(r_i) \tag{2.3}$$

This Equation (2.3) is the Born-Oppenheimer approximation, and incorporating this approximation, the Schrödinger equation for electrons in the potential of stationary nuclei

can be written as,

$$H_e\Omega(R_I;r_i) = V(R_I)\Omega(R_I;r_i) \tag{2.4}$$

where, H_e is given as,

$$H_e = -\sum_i \frac{\hbar^2}{2m_e}\nabla^2_{r_i} + \frac{1}{2}\sum_{I,J_{(I\neq J)}} \frac{Z_I Z_J e^2}{|R_I - R_J|} + \frac{1}{2}\sum_{i,j_{(i\neq j)}} \frac{e^2}{|r_i - r_j|} - \sum_{I,i_{(I\neq i)}} \frac{Z_I e^2}{|R_I - r_i|} \tag{2.5}$$

The eigenvalue $V(R_I)$ can be known from Equation (2.4), which can be used to construct the Hamiltonian for nuclei,

$$H_n = -\sum_I \frac{\hbar^2}{2M_I}\nabla^2_{R_I} + V(R_I) \tag{2.6}$$

The energy eigenvalue of nuclei E^n can be known from,

$$H_n\Pi(R_I) = E^n\Pi(R_I) \tag{2.7}$$

In this way, Born-Oppenheimer approximation can reduce the complexity of Equation (2.2). The electronic structure calculation in the static potential of the nuclei, as described by Equation (2.4) is the starting point for DFT.

2.1.3 Thomas-Fermi-Dirac Theory

In the earlier section, it has been discussed that the Schrödinger formulation of the wave function is impractical for the many-body problem and the possible solution would be electron density functional representation. DFT, by its name, is based on density functional

representation and the first theory which proposes electron density function to determine the electronic structure in the many-body system is the Thomas-Fermi (TF) model [36]. The TF model was proposed independently by two physicists, Thomas and Fermi, in the year 1927. According to the TF model, the total energy of the electrons in the potential of frozen nuclei is the functional of electron density $n(r)$ and expressed as,

$$E[n(r)] = A_1 \int n(r)^{(5/3)} dr + \int n(r)V(r)dr + \frac{1}{2}\int\int \frac{n(r)n(r')}{|r-r'|} drdr' \tag{2.8}$$

where, the first term in the right hand side of the equation represents the kinetic energy of the non-interacting electrons in a homogeneous electron gas, the second term is the nucleus-electron interaction and the last term is the electron-electron interaction, or Hartree energy [37]. Later, in the year 1930, Dirac added a new term called local exchange term [38], $A_2 \int n(r)^{(4/3)} dr$ in Equation (2.8), i.e.,

$$E[n(r)] = A_1 \int n(r)^{(5/3)} dr + \int n(r)V(r)dr + \frac{1}{2}\int\int \frac{n(r)n(r')}{|r-r'|} drdr' + A_2 \int n(r)^{(4/3)} dr \tag{2.9}$$

Finally, the ground state electron density can be known by minimizing the total energy $E[n(r)]$, under the normalizing conditions, $\int n(r)dr = N$ and $\delta(E[n(r)] - \mu N) = 0$, where N and μ are the total number of electrons and Lagrange multiplier. The final expression after minimization is,

$$\frac{5}{3}A_1 n(r)^{(2/3)} + V(r) + \int \frac{n(r')}{|r-r'|} dr' + \frac{4}{3}A_2 n(r)^{(1/3)} - \mu = 0 \tag{2.10}$$

which can be readily solved to obtain ground state electron density. The primary drawbacks of TF model is that it neglects the shell structures of the atoms and bonding between atoms and molecules.

2.1.4 Hohenberg-Kohn (HK) Theorem

DFT was introduced by Hohenberg and Kohn in 1964. They formulated and proved the theorem, which is the backbone of DFT. This HK theorem states that the energy of the many-body electronic system can be expressed exclusively in terms of its electronic density. This theorem is scrutinized into two parts and the details can be found in [39]:

Theorem 1. *The external potential is uniquely determined by the electronic density, besides the trivial additive constant.*

Proof. The proof follows the contradiction method, i.e., it assumes two different potentials V and V' for the same electronic density n and ends with contradiction. Suppose, ψ and $E_0 = \langle\psi|\widehat{H}|\psi\rangle$ are the ground state wave function and ground state energy of the Hamiltonian $\widehat{H} = \widehat{T} + \widehat{V} + \widehat{U_{ee}}$. Likewise, ψ' and $E_0' = \langle\psi'|\widehat{H'}|\psi'\rangle$ of the Hamiltonian $\widehat{H'} = \widehat{T} + \widehat{V'} + \widehat{U_{ee}}$. According to the variational principle,

$E_0 < \langle\psi'|\widehat{H}|\psi'\rangle$

or, $E_0 = \langle\psi'|\widehat{H'}|\psi'\rangle + \langle\psi'|\widehat{H} - \widehat{H'}|\psi'\rangle$

$$\therefore \quad E_0 = E_0' + \int n(r)[V(r) - V'(r)]dr \tag{2.11}$$

Similarly, for $E_0' < \langle\psi|\widehat{H'}|\psi\rangle$

$$E_0' = E_0 - \int n(r)[V(r) - V'(r)]dr \tag{2.12}$$

By adding Equations (2.11) and (2.12), one obtains $E_0 + E_0' < E_0' + E_0$, which is a contradiction, establishing that there exists one to one correspondence between electronic density and external potential. □

Theorem 2. *The global minimization of the energy functional* $E[n(r)] = \int n(r)V(r)dr + F[n(r)]$ *by the exact ground state density* n_0 *is the exact ground state energy of the system if and only if* $F[n(r)]$ *exists as a universal functional of the density, independent of the external potential* $V(r)$.

Proof. This can be proved by showing $E[n(r)]$ as the unique functional of $n(r)$ provided $E[n(r)] = \int n(r)V(r)dr + F[n(r)]$ where, $F[n(r)]$ is the universal function of the density $n(r)$.

Following the HK theorem 1,

$E[\psi] = \langle\psi|\widehat{H}|\psi\rangle = E[n(r)] = \int n(r)V(r)dr + F[n(r)]$

If ψ_0 is the ground state functional then $E\psi_0 = \int n_0(r)V_0(r)dr + F[n_0(r)]$. Since, $E[\psi] > E[\psi_0]$ which implies $E[n(r)] > E[n_0(r)]$ and $E[n(r)] = E[n_0(r)]$ if and only if $n(r) = n_0(r)$. Therefore, by minimizing the total energy functional $E[n(r)]$, it is possible to obtain the ground state energy of the system. □

Though we have shown the one-to-one correspondence of total energy with density, global minimization of total energy with the ground state density is the ground state energy. However, in this process, there is one hindrance, which is the unknown universal functional $F[n(r)]$. It is usually guessed that $F[n(r)]$ is associated with the sum of the kinetic energy of the electrons and their interaction energy. After one year of HK theorem, Kohn-Sham provided the methods to identify $F[n(r)]$, known as Kohn-Sham (KS) Ansatz [40].

2.1.5 Kohn-Sham (KS) Ansatz

Because of undeterministic universal density function $F[n(r)]$, the K-S ansatz is a good guess in determining the exact ground state energy of the multi-body system. In other words, the KS ansatz utilizes the HK theorems, making DFT calculations possible even in a personal computer. As a result, it has made DFT as a feasible and popular tool for the electronic structure calculations, and for this development, Walter Kohn was awarded the Noble Prize in 1998. The KS ansatz substitutes the real many-body interacting system by

the fictitious system of non-interacting system weighted by the same ground state density. The real potential of interacting system is replaced by KS potential V_{KS} of non-interacting system, expressing the Hamiltonian of the fictitious system as $\widehat{H}_{KS} = -\frac{1}{2}\nabla^2 + V_{KS}$ in atomic units. Then, the resulting Schrödinger like equation is,

$$\widehat{H}_{KS}\psi_i(r) = \varepsilon_i\psi_i(r) \tag{2.13}$$

where, $\psi_i(r)$ is the independent particle KS orbital. The electron density of N electrons is given by

$$n(r) = \sum_i^N |\psi_i(r)|^2 \tag{2.14}$$

which is subject to the condition,

$$\int n(r)dr = N \tag{2.15}$$

Moreover, the kinetic energy $T_s[n(r)]$ of the non-interacting independent particle is,

$$T_s[n(r)] = \frac{1}{2}\sum_i^N \int \psi_i^*(r)\nabla^2\psi_i(r)dr \tag{2.16}$$

Now, the universal functional $F[n(r)]$ is expressed as,

$$F[n(r)] = T_s[n(r)] + E_H[n(r)] + E_{XC}[n(r)] \tag{2.17}$$

where, $E_H[n(r)]$ is the Hartree energy and $E_{XC}[n(r)]$ is the exchange-correlation (XC) energy. Finally, using the HK theorem II and Lagrange minimization technique,

$$\delta F[n(r)] + \int n(r)V(r)dr - \lambda(\int n(r)dr - N) = 0 \tag{2.18}$$

where, the Lagrange multiplier is given as,

$$\begin{aligned}
\lambda &= \frac{\delta F[n(r)]}{\delta n(r)} + V(r) \\
&= \frac{\delta T_s[n(r)]}{\delta n(r)} + \frac{\delta E_H[n(r)]}{\delta n(r)} + \frac{\delta E_{XC}[n(r)]}{\delta n(r)} + V(r) \\
&= \frac{\delta T_s[n(r)]}{\delta n(r)} + V_H(r) + V_{XC}(r) + V(r) \\
&= \frac{\delta T_s[n(r)]}{\delta n(r)} + V_{KS}(r)
\end{aligned} \tag{2.19}$$

where, $V_{KS}(r) = V_H(r) + V_{XC}(r) + V(r)$. In practice, one chooses the initial electron density and find $V_{KS}(r)$. Then by virtue of Equations (2.13) and (2.14), new electron density is calculated. This process iterates till both input and output electron density becomes same, which is the required ground state density. However, this method approximates V_{KS} as $V_{XC}(r)$ is still unknown, giving unknown exchange-correlation (XC) energy, $E_{XC}[n(r)]$. To fix this issue, a number of approximations for the quantity $E_{XC}[n(r)]$ are made. The accuracy of DFT calculations depends on the choice of these approximations.

2.1.6 Approximations to Universal Density Functional

The success of the KS ansatz is the determination of kinetic energy of the non-interacting electrons. This has resolved the unknown universal density functional and the accuracy of determining the ground state density of original interacting system is limited only to the

exchange-correlation energy $E_{XC}[n(r)]$. In short,

$$\begin{aligned} E &= min_{n(r)} \int n(r)V(r)dr + F[n(r)] \\ &= min_{n(r)} \int n(r)V(r)dr + T_s[n(r)] + E_H[n(r)] + E_{XC}[n(r)] \end{aligned} \tag{2.20}$$

Therefore, for the determination of $E_{XC}[n(r)]$, a number of approximations are made. They are as follows:

(i) Local Density Approximation (LDA): The LDA approximation assumes the electron density n(r) to be uniform as in homogeneous electron gas model, i.e., n(r) is same at any point $r = r_1$ or $r = r_2$ inside this gas. In this approximation,

$$E_{XC}[n(r)] = \int n(r)\varepsilon_{XC}(n)dr \tag{2.21}$$

where, $\varepsilon_{XC}(n)$ is the XC energy per particle. The $\varepsilon_{XC}(n)$ can be further decomposed as $\varepsilon_{XC} = \varepsilon_X + \varepsilon_C$, where $\varepsilon_X(n)$ is determined analytically as Dirac functional and $\varepsilon_C(n)$ by Quantum Monte Carlo calculations. In practice, the performance of LDA is good for ionic, covalent and metallic materials, where this method predicts tighter chemical bonding. For hydrogen bonds, Van der Waals bonds and negatively charged materials, the LDA approximation is not sufficient.

(ii) Generalized Gradient Approximation (GGA): The GGA approximation is more advanced than the LDA approximation, where the electronic density n(r) fluctuates in space, implying the non-uniform electron gas. In other words, the XC energy is functional of electron density and its gradient, i.e., $E_{XC} = E_{XC}[n(r), \nabla n(r)]$. There are different parametrizations for exchange and correlation energy and many of them are semi-empirical and derived from fitting the experimental data. However, the most common one is the parameter-free GGA functional developed by Perdew, Burke, Ernzerhof (PBE) [41]. The

E_{XC} in PBE is defined as,

$$E_{XC}[n(r)] = \int n(r)\varepsilon_{XC}X[n(r), \nabla(n(r))]dr \tag{2.22}$$

where X is the enhancement factor, which includes both spatial and gradient factors.

(iii) Hybrid functional: The hybrid functional incorporates some portion of hybrid exchange-correlation functional E_{XC}^{HF} (derived from the Hartree-Fock exact exchange functional), with the exchange-correlation functional of standard DFT. It includes families of functionals such as PBE0, B3LYP and HSE. Generally, the E_{XC} after mixing hybrid functional with the PBE functional is given as,

$$E_{XC} = \alpha E_X^{HF} + (1-\alpha)E_X^{PBE} + E_C^{PBE} \tag{2.23}$$

where, α is the HF mixing parameter. In PBE0 functional, α is 0.25 indicating that HF exchange energy is mixed with PBE exchange energy in the ratio 1:3, with 100% correlation energy from PBE functional. However, in B3LYP functional, the correlation energy is incorporated with LDA and GGA functional. The PBE0 functional is mostly good at structural optimization. One demerit of PBE0 functional is the long range convergence issue of HF exchange. This issue is resolved in HSE functional, where the exchange part of the electron-electron interaction is arbitrarily decomposed into short range (SR) and long range (LR) factors, i.e.,

$$E_{XC}^{HSE} = \alpha E_X^{HF,SR}(\omega) + (1-\alpha)E_X^{PBE,SR}(\omega) + E_X^{PBE,LR}(\omega) + E_C^{PBE} \tag{2.24}$$

where, ω is the screening parameter. For $\alpha = 0.25$ and $\omega = 0$, one gets $E_{XC}^{HSE} = E_{XC}^{PBE0}$. For standard HSE functional (HSE06), the α and ω are 0.25 and 0.2, respectively. Though computationally expensive, the HSE06 functional usually gives good results for many materials.

Besides these exchange-correlation functionals, there are many varieties of functionals, which are not discussed in this dissertation. For example, the family of meta-GGA functionals considers $E_{XC}[n(r), \nabla(n(r)), \nabla^2(n(r))]$. The Hubbard correction U is another approximation, which is incorporated with the standard approximation (LDA, GGA), for strongly correlated systems, where $3d$, $4d$, $4f$ and $5f$ electrons are localized and close to Fermi energy. In short, there are many approximations, put forward for $E_{XC}[n(r)]$ and to determine the correct one is the main challenge for DFT practitioners. The second challenge would be the compromise between the accuracy of the results and computational efficiency. The PBE functional is a good choice in terms of computational efficiency. However, to increase accuracy, one needs to mix a certain amount of Hartree-Fock exchange, that may be at the expense of the computational efficiency.

2.1.7 DFT Implementation in Periodic Systems

The KS ansatz described a self consistent iterative procedure in which the initial density function $n(r)$ is chosen and the KS potential is calculated and by virtue of Equations (2.13) and (2.14), the new density function n' is obtained. This process iterates till $n(r)$ and $n'(r)$ satisfy the given condition yielding the final density function as the ground state density. To implement this procedure computationally, the plane wave pseudo-potential method is used. This method utilizes Bloch's theorem [42] and expresses KS orbital in terms of an infinite sum of plane waves. For the periodic system, the wave function ψ_n of an electron in the n^{th} band can be described as Bloch's electron, containing periodic cell function $u_n(r)$ and a plane wave e^{ikr},

$$\psi_n(r) = u_n(r)e^{ikr} \tag{2.25}$$

where k is the wave vector confined to the first Brillouin zone. The periodic cell function can further be expressed as the linear combination of plane waves in reciprocal space,

$$u_n(r) = \sum_G c_{n,G} e^{iGr} \tag{2.26}$$

where G is the reciprocal lattice vector and $c_{n,G}$ is the coefficient. By combining the above two equations, the KS orbitals can be expressed as the infinite sum of plane waves,

$$\psi_n(r) = \sum_G c_{n,k+G} e^{i(k+G)r} \tag{2.27}$$

In practice, this infinite sum of plane waves is truncated as a finite number by reducing the Brillouin zone sampling using the point group symmetry of the lattice, that is, sampling in the irreducible Brillouin zone. The next step is to choose the cutoff energy E_{cut} for the plane-wave basis in such a way that the plane waves below this cut off are included in the basis, i.e., $E_{cut} \geq \frac{1}{2}|k+G|^2$. For the efficient DFT performance, the number of K-points for IBZ sampling and proper E_{cut} is required. Besides representing the KS orbital as the finite sum of plane-wave basis, the pseudo-potential approximation is implemented to reduce the number of KS orbitals. This is achieved by dividing the electrons as core and valence. Core electrons are closer to the nuclei and can be replaced along with the nuclear field by suitable pseudo-potential. Therefore, in DFT calculations, core electrons are not treated explicitly (frozen core) and only valence electrons are responsible for the physical properties of the system. There are mainly three methods to implement pseudo-potential: norm-conserving, ultrasoft and projector augmented wave (PAW). The norm-conserving pseudo-potential conserves the charge density inside the core region and outside the core region; it behaves as a real wave function producing the same charge distribution and eigenvalues. In ultrasoft pseudo-potential, there is no constraint of the norm conservation

and uses lower cutoff energy for the convergence. The PAW method is quite advanced and solves DFT calculations with greater computational efficiency. It utilizes the rapidly oscillating core wave functions and transfers into smooth wave functions. From these smooth wave functions, electronic properties are then calculated.

Therefore, the KS wave functions can be expressed by the application of Bloch's theorem and KS potential by pseudo-potential approximation. The ground state density is obtained using the KS ansatz. Then, the total energy of a unit cell is obtained by summing over IBZ. IBZ can be unrolled later to cover the entire Brillouin zone. The sampling of the Brillouin zone is usually achieved through the tetrahedron method, in a special K-points grid such as Cunningham K-points, Γ- centered, Monkhorst-Pack grids schemes etc. The non-periodic or less symmetric system can also follow the similar schemes with some reservations, if considered in a large super cell.

2.2 Structural Optimization

Structural optimization is the first and foremost process in computer simulation processing of a material. This is because "structure dictates the properties" and finding the correct configuration of electrons wandering in the positive background of the nuclei has, therefore, paramount significance. Structure can be optimized either by including size, shape, topology or both and therefore relates to many constraint variables. The best way to find the correct structure is to use the X-ray diffraction technique. In the case of crystalline solids, it is often useful to consider geometric optimization for finding the geometry which minimizes the energy and the forces acting on each atom, together with the strain on a given system. The effect of external conditions such as pressure and temperature can be thought as the perturbation from this geometry. Theoretically, geometric optimization can be performed by relaxing the structure at different volumes and finding the global minimum energy and correct pressure. This can be done by fitting the structure with suitable equations of state (EoS). There are various models for fitting energy or pressure

with volume such as Birch's EoS, Murnaghan EoS, Birch-Murnaghan isothermal EoS, Rose-Vinet EoS, etc. One can get equilibrium bulk modulus and its derivative, which can further be compared with the experimental value. It is always good to use EoS fitting and know the volume which has minimum energy. This will be beneficial to reduce local minimization of the structure, which often happens during simulations. Since EoS are analytical equations, these may have limitations for high-pressure structures as in the rocks found in the earth's crust and phase transition induced by temperature and pressure. One of the popular EoS is the third-order Birch-Murnaghan isothermal equation. In terms of pressure-volume (P-V), it is expressed as,

$$P(V) = \frac{3B_o}{2}[(\frac{V_o}{V})^{7/3} - (\frac{V_o}{V})^{5/3}]\{1 + \frac{3}{4}(B'_o - 4)[(\frac{V_o}{V})^{2/3} - 1]\} \tag{2.28}$$

where, B_o and B'_o are the bulk modulus and the derivative of the bulk modulus with respect to pressure. Likewise, in terms of internal energy-volume (E-V),

$$E(V) = E_o + \frac{9V_oB_o}{16}\{[(\frac{V_o}{V})^{2/3} - 1]^3B'_o + [(\frac{V_o}{V})^{2/3} - 1]^2[6 - 4(\frac{V_0}{V})^{2/3}]\} \tag{2.29}$$

2.3 Vibrational Properties

The vibrational study bears tremendous significance as the thermal effects and phase stability of the materials are related to the vibration of atoms around their equilibrium positions. For instance, the phase stability of a material is related to the minimization of free energy, i.e., $G = H - TS$, where, H is the enthalpy and T is the temperature. The basic source of entropy S is the thermal vibration of atoms. Therefore, the vibrational dynamics of materials are crucial to understanding the subtle mechanism of the evolution of properties.

2.3.1 Lattice Dynamics

Atoms in a crystal are not in a static position in their ground states. They are constantly vibrating even at absolute zero (zero-point energy) and respond to external perturbation and thermal energy by an increase in their kinetic energy. At higher temperatures, atoms show different modes of vibration, and as the temperature decreases, they are restricted to vibrate in fewer and fewer ways. From the ground state, the displacement of atoms can be assumed to be smaller than their inter-atomic length. If R_i is the ground state position of an atom in a lattice and u_i is its displacement due to thermal energy, then its position r_i can be written as $r_i = R_i + u_i$. Then, the perturbation in the potential energy $V(R)$ can be expressed as the Taylor series of atomic displacement u_i as,

$$V(R,u_i) = V_0(R) + \sum_i \frac{\partial V}{\partial u_i} + \frac{1}{2}\sum_{ij} \frac{\partial^2 V}{\partial u_i \partial u_j} u_i u_j + \frac{1}{6}\sum_{ijk} \frac{\partial^3 V}{\partial u_i \partial u_j \partial u_k} u_i u_j u_k + \ldots \tag{2.30}$$

The term $V_0(R)$ is the potential at the ground state, the second term represents the sum of all the forces acting on an atom, which is zero by virtue of Newton's law, the third term is due to restoring force and the remaining are higher-order terms. In the harmonic approximation (HA) regime, the higher-order terms are neglected. This leads to,

$$V(R,u_i) = V_0(R) + \frac{1}{2}\sum_{ij} \frac{\partial^2 V}{\partial u_i \partial u_j} u_i u_j \tag{2.31}$$

The term $\frac{\partial^2 V}{\partial u_i \partial u_j}$ is called dynamical matrix D_{ij} and the total restoring force F_i acting on an atom due to displacement of remaining atoms can be written as $F_i = m\ddot{u}_i = -\sum_j D_{ij} u_j$. This gives the differential equation,

$$m\ddot{u}_i + \sum_j D_{ij} u_j = 0 \tag{2.32}$$

whose solution gives the allowed mode of the vibrational frequencies.

2.3.2 Linear Chain Model

Let us consider a crystal lattice containing two kinds of atoms/ions, say A and B. A linear chain model is a 1D description, where A and B atoms are lying alternatively and successively forming a chain. Let the distance between A and B be $\frac{a}{2}$ at rest, which implies the distance between A-A and B-B is a. The force between A and B is considered to be simple harmonic. Suppose U_n is the displacement of the n^{th} A atom, then on its left, the displacement of the n^{th} B atom be u_n and on its right the displacement of the $(n+1)^{th}$ B atom be u_{n+1}. If J is the force constant, then the force acting on n^{th} A atom is $F_n = -J(2U_n - u_n - u_{n+1})$ and n^{th} B atom is $f_n = -J(2u_n - U_n - U_{n-1})$. Newton's II law leads to second order differential equations as,

$$M\frac{\partial^2 U_n}{\partial t^2} = -J(2U_n - u_n - u_{n+1}) \tag{2.33}$$

$$m\frac{\partial^2 u_n}{\partial t^2} = -J(2u_n - U_n - U_{n-1}) \tag{2.34}$$

where, M and m are the masses of A and B atoms, respectively. The solutions of these differential equations in the form of sinusoidal waves are,

$$U_n = \hat{U} exp\{i[k(n+\frac{1}{2})a - \omega t]\} \tag{2.35}$$

$$u_n = \hat{u} exp\{i[kna - \omega t]\} \tag{2.36}$$

where, $\hat{U}$ and $\hat{u}$ are the amplitudes of the A and B atoms, respectively. These sinusoidal solutions when substituted into their respective differential equations yield two equations, which can be combined in matrix form as,

$$\begin{bmatrix} 2J - M\omega^2 & -2Jcos(\frac{ka}{2}) \\ -2Jcos(\frac{ka}{2}) & 2J - m\omega^2 \end{bmatrix} \begin{bmatrix} \hat{U} \\ \hat{u} \end{bmatrix} = 0 \tag{2.37}$$

For non-trivial solution $\begin{bmatrix} \hat{U} \\ \hat{u} \end{bmatrix} \neq 0$, which implies,

$$\begin{vmatrix} 2J - M\omega^2 & -2Jcos(\frac{ka}{2}) \\ -2Jcos(\frac{ka}{2}) & 2J - m\omega^2 \end{vmatrix} = 0 \tag{2.38}$$

After evaluating this determinant, one can get the value of ω^2 as,

$$\omega^2 = J(\frac{1}{M} + \frac{1}{m}) \pm J\sqrt{(\frac{1}{M} + \frac{1}{m})^2 - \frac{4sin^2(\frac{ka}{2})}{Mm}} \tag{2.39}$$

which is known as the dispersion relation. Figure 2.1 shows the dispersion relations when $M = 0.5m$, $M = m$, and $M = 0.1m$. One can easily notice that the dispersion relation is periodic in k, with a period $k = \frac{2\pi}{a}$ and implies that the behavior of the curve is completely described by the region $-\frac{\pi}{a} : k : \frac{\pi}{a}$, which is well known as the Brillouin zone. Furthermore, Equation (2.39) is symmetric with k, i.e., $\omega(k) = -\omega(-k)$. The branch for which $\omega = 0$, when $k = 0$ is an acoustic branch and $\omega \neq 0$ when $k = 0$ is an optical branch and the forbidden gap between them represents the mass difference between the atoms. In the acoustic branch, atoms vibrate in phase with sound wave, i.e., $\omega = c_s k$, whereas the

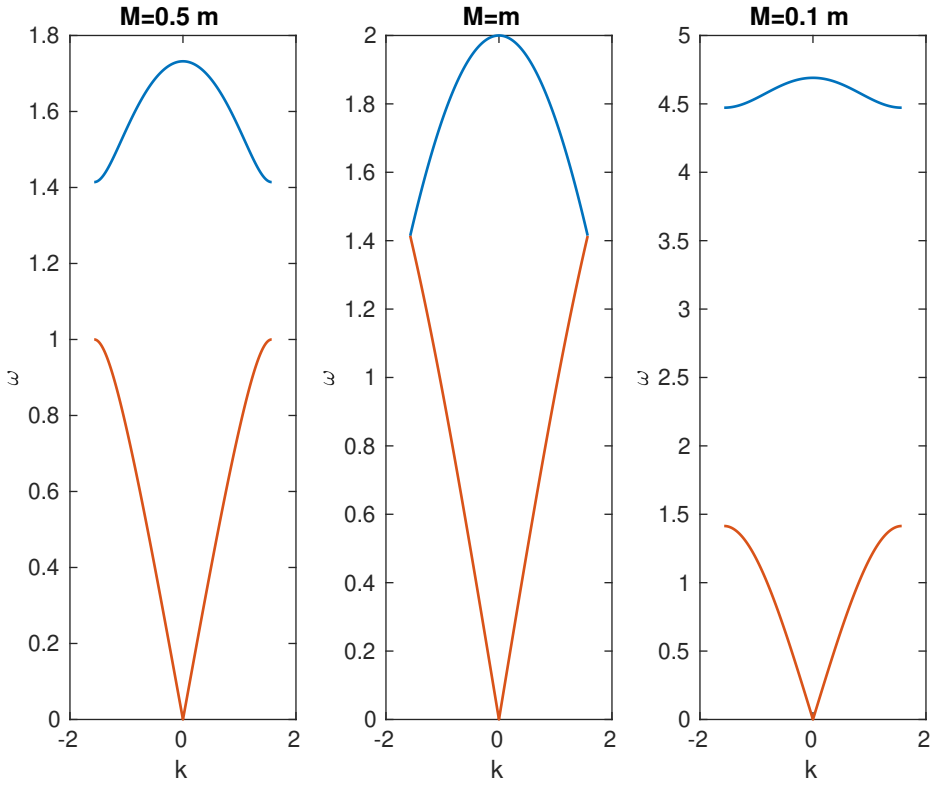

Figure 2.1 The dispersion relation ω versus k, using Equation (2.39).

vibration is not in phase in the optical branch. For charged atoms or ions, the vibration in the optical branch induces electromagnetic radiation of an infrared frequency.

The linear chain model can be generalized to 3D crystals. For instance, if there are s atoms per unit cell of a crystal, then the total number of branches will be the number of the total degree of freedom,i.e., $3s$; one in the direction of k (longitudinal) and two perpendicular to k (transverse). The number of acoustic and optical branches are 3 and $3s-3$, respectively. The coupled harmonic oscillations of the atoms are described by lattice waves. Each lattice wave is independent and has a unique pattern of collective oscillations or modes with a common frequency, known as normal modes. The assumption of the independent nature of normal modes is valid only in the harmonic regime and deviates once the vibration is anharmonic. In the above illustration, $3s$ is the number of normal modes. The quanta of these normal modes of vibrations are called phonons, analogous

to the quanta of electromagnetic waves, the photons. In other words, an electron can be considered as the smallest charge carrier and in the same way, a phonon can be considered as the smallest carrier of heat. The energy of the lattice wave corresponding to the i^{th} normal mode of frequency ω_i can be formulated by the quantum harmonic oscillator model as,

$$E_i = (n_i + \frac{1}{2})\hbar\omega_i \tag{2.40}$$

where, n_i is the number of phonons with frequency ω_i, at temperature T, distributed accordingly to the Bose-Einstein model,

$$n_i(\omega_i, T) = \frac{1}{exp(\frac{\hbar\omega_i}{k_B T}) - 1} \tag{2.41}$$

The total energy E is then the summation of E_i, where i runs from 1 to $3s$. The thermodynamic quantities can be derived from this E. As an example, the heat capacity at constant volume can be found as $c_V = (\frac{\partial E}{\partial T})_V$.

2.3.3 Phonon Density of States

The phonon density of states, D, describes the number of modes or states per frequency range. Mathematically, it is expressed as the number of modes (N) per unit frequency per unit volume (V) of the real space, i.e.,

$$\begin{aligned} D &= \frac{1}{V}\frac{dN}{d\omega} \\ &= \frac{1}{V}\frac{dN}{dk}\frac{dk}{d\omega} \end{aligned} \tag{2.42}$$

The number of modes inside the sphere of radius k can be found by dividing the total volume of the sphere V with the smallest unit cell in the phase space V_s, i.e.,

$$N = \frac{V}{V_s} = \frac{\frac{4}{3}\pi k^3}{(\frac{2\pi}{L})^3} = \frac{k^3 L^3}{6\pi^2} \tag{2.43}$$

this gives,

$$\frac{dN}{dk} = \frac{k^2 L^3}{2\pi^2} \tag{2.44}$$

substituting Equation (2.44) in Equation (2.42) yields,

$$D = \frac{k^2}{2\pi^2}\frac{1}{v_g} \tag{2.45}$$

where, $v_g = \frac{d\omega}{dk}$ is the group velocity. Since the group velocity of an optical phonon is zero, the acoustic phonons are only responsible for the density of states. The group velocity of an acoustic phonon is the sound wave c_s, which further yields,

$$D = \frac{3\omega^2}{2\pi^2 c_s^3} \tag{2.46}$$

The factor 3 implies that there are three acoustic modes per k. The notion of phonon density of states bears tremendous significance. The structural stability of the phase of a material is governed by positive vibrational modes of phonons. The phonons associated with imaginary modes are called soft modes, which is the basis to investigate the different phases of a material. Debye has modelled a solid as a set of phonons in a box and calculated

the total energy as,

$$E = \int_0^{\omega_D} D(\omega) V \hbar\omega \frac{1}{exp(\frac{\hbar\omega}{k_B T}) - 1} d\omega \tag{2.47}$$

where, ω_D is the largest frequency that can be excited at a given temperature, called Debye frequency and the temperature featuring Debye frequency is Debye temperature T_D ($T_D = \frac{\hbar\omega_D}{k_B}$). The thermal conductivity is associated with the product of energy and group velocity of the phonons. Likewise, the coupling among electrons and phonons can give rise to many phenomena that are associated with magnetic and optoelectronic properties.

2.3.4 Anharmonicity

As mentioned earlier, the normal modes are dependent on anharmonic lattice vibration. The common drawbacks of HA are as follows: interatomic distances are kept invariant (no thermal expansion) and as a consequence, there is no distinction between heat capacities at constant pressure and constant volume. The HA is good at low temperature and as temperature rises, atoms begin to vibrate anharmonically. As a result, one is forced to use the higher-order term as mentioned in Equation (2.30). The inclusion of higher-order terms makes the mathematical model more complex and the diagonalization of the dynamical matrix is difficult to compute. Usually, the larger forbidden gap materials are good for HA as the scattering processes rate is low and phonons can be assumed to have a longer lifetime. Some portion of anharmonicity can be addressed by quasi-harmonic approximation (QHA). QHA includes a part of an anharmonic effect with volume dependence of phonon frequencies. Unlike HA, QHA, therefore, includes volume-dependent thermal expansion, and the total energy is computed as,

$$E = \sum_i E_i = \sum_i [n_i(\omega_i, T, V) + \frac{1}{2}] \hbar\omega_i(V) \tag{2.48}$$

where, $n_i(\omega_i, T, V)$ is calculated in the same way as in HA for each lattice volume V. The QHA model is essential to study the thermal expansion and temperature-dependent properties such as phase transition, free energies, etc.

2.4 Elastic Properties

The elastic properties for a linear elastic material can be modelled from the generalized Hooke's law,

$$\begin{bmatrix} \sigma_1 \\ \sigma_2 \\ \sigma_3 \\ \sigma_4 \\ \sigma_5 \\ \sigma_6 \end{bmatrix} = \begin{bmatrix} C_{11} & C_{12} & C_{13} & C_{14} & C_{15} & C_{16} \\ C_{21} & C_{22} & C_{23} & C_{24} & C_{25} & C_{26} \\ C_{31} & C_{32} & C_{33} & C_{34} & C_{35} & C_{36} \\ C_{41} & C_{42} & C_{43} & C_{44} & C_{45} & C_{46} \\ C_{51} & C_{52} & C_{53} & C_{54} & C_{55} & C_{56} \\ C_{61} & C_{62} & C_{63} & C_{64} & C_{65} & C_{66} \end{bmatrix} \begin{bmatrix} \varepsilon_1 \\ \varepsilon_2 \\ \varepsilon_3 \\ \varepsilon_4 \\ \varepsilon_5 \\ \varepsilon_6 \end{bmatrix} \tag{2.49}$$

i.e., {stress vector= stiffness matrix $\times$ strain vector}

In compact notation, $\sigma_m = S_{mn}\varepsilon_n$. The stiffness matrix S_{mn} is the central identity which characterizes the various elastic properties such as bulk modulus, Poisson ratio, etc., of a crystal. It is related to the energy E as,

$$S_{mn} = \frac{1}{V_0}\left(\frac{\partial^2 E}{\partial \varepsilon_m \partial \varepsilon_n}\right) \tag{2.50}$$

where, V_0 is the equilibrium volume of a crystal. The inverse of stiffness matrix is known as compliance matrix, $[C_{mn}] = [S_{mn}]^{-1}$ and the Hooke's law in terms of compliance matrix is $\varepsilon_m = C_{mn}\sigma_n$. Both of these matrices are symmetric and thereby have 21 independent

elastic constants, i.e.,

$$S_{mn} = \begin{bmatrix} C_{11} & C_{12} & C_{13} & C_{14} & C_{15} & C_{16} \\ C_{12} & C_{22} & C_{23} & C_{24} & C_{25} & C_{26} \\ C_{13} & C_{23} & C_{33} & C_{34} & C_{35} & C_{36} \\ C_{14} & C_{24} & C_{34} & C_{44} & C_{45} & C_{46} \\ C_{15} & C_{25} & C_{35} & C_{45} & C_{55} & C_{56} \\ C_{16} & C_{26} & C_{36} & C_{46} & C_{56} & C_{66} \end{bmatrix} \tag{2.51}$$

However, for non-linear problems where stress at a point depends not only on the strain at that point but also on the neighbouring points, the stiffness matrix may not be symmetric. If the stress and strain relation is independent of orientation and is the same in all directions, then the material is isotropic. For isotropic materials, symmetry reduces the number of elastic constants to two, i.e.,

$$S_{mn} = \begin{bmatrix} C_{11} & C_{12} & C_{12} & 0 & 0 & 0 \\ C_{12} & C_{11} & C_{12} & 0 & 0 & 0 \\ C_{12} & C_{12} & C_{11} & 0 & 0 & 0 \\ 0 & 0 & 0 & \frac{(C_{11}-C_{12})}{2} & 0 & 0 \\ 0 & 0 & 0 & 0 & \frac{(C_{11}-C_{12})}{2} & 0 \\ 0 & 0 & 0 & 0 & 0 & \frac{(C_{11}-C_{12})}{2} \end{bmatrix} \tag{2.52}$$

Furthermore, the stiffness matrix also depends on the crystal system. For example, the number of elastic constants in cubic and orthorhombic crystals reduces to 3 and 9,

respectively.

$$S_{mn} = \begin{bmatrix} C_{11} & C_{12} & C_{12} & 0 & 0 & 0 \\ C_{12} & C_{11} & C_{12} & 0 & 0 & 0 \\ C_{12} & C_{12} & C_{11} & 0 & 0 & 0 \\ 0 & 0 & 0 & C_{44} & 0 & 0 \\ 0 & 0 & 0 & 0 & C_{44} & 0 \\ 0 & 0 & 0 & 0 & 0 & C_{44} \end{bmatrix} \longrightarrow cubic \tag{2.53}$$

$$S_{mn} = \begin{bmatrix} C_{11} & C_{12} & C_{13} & 0 & 0 & 0 \\ C_{12} & C_{22} & C_{23} & 0 & 0 & 0 \\ C_{13} & C_{23} & C_{33} & 0 & 0 & 0 \\ 0 & 0 & 0 & C_{44} & 0 & 0 \\ 0 & 0 & 0 & 0 & C_{55} & 0 \\ 0 & 0 & 0 & 0 & 0 & C_{66} \end{bmatrix} \longrightarrow orthorhombic \tag{2.54}$$

The elastic modulus and other properties can be known once the stiffness matrix is computed. For instance, in a cubic crystal, the elastic stability criterion is $(C_{11} - C_{12} > 0)$, $C_{11} > 0$, $C_{44} > 0$, $C_{11} + 2C_{12} > 0$, which is also known as Born stability criteria. The other macroscopic properties such as bulk modulus, shear modulus, Young's modulus, Poisson's ratio, Cauchy pressure, and anisotropy coefficient are suitable for the collection of a number of single crystals. The stress-strain relation is quite complex in polycrystals and suitable approximations should be made. The Voigt approximation assumes the strain to be the same in all grains, the Reuss approximation considers uniform stress, and the Hill approximation takes the Voigt and the Reuss approximation as the upper and the lower bounds for the effective elastic constants of polycrystals and takes the average between these two approximations. Using the Voigt-Reuss-Hill (VRH) approximations, the bulk

modulus B is computed as,

$$\begin{aligned} B_V &= \frac{C_{11}+2C_{12}}{3} \\ B_R &= \frac{C_{11}+2C_{12}}{3} \\ B &= \frac{B_V+B_R}{2} \end{aligned} \tag{2.55}$$

and the shear modulus G as,

$$\begin{aligned} G_V &= \frac{C_{11}-C_{12}+3C_{44}}{5} \\ G_R &= \frac{5C_{44}(C_{11}-C_{12}}{4C_{44}+3(C_{11}-C_{12})} \\ G &= \frac{G_V+G_R}{2} \end{aligned} \tag{2.56}$$

The Young's modulus E and Poisson's ratio v are computed as,

$$E = \frac{9BG}{3B+G} \tag{2.57}$$

$$v = \frac{3B-2G}{2(3B+G)} \tag{2.58}$$

The Cauchy pressure C relates to the nature of atomic bonding and the anisotropy factor A relates to the formation of cracks in the materials; they are computed as follows,

$$C = C_{12} - C_{44} \tag{2.59}$$

$$A = \frac{2C_{44}}{C_{11} - C_{12}} \tag{2.60}$$

The Debye temperature T_D can be calculated from the elastic constants, using average sound velocity v_m,

$$T_D = \frac{hv_m}{k}[\frac{3n}{4\pi}(\frac{N_A\rho}{M})]^{\frac{1}{3}} \tag{2.61}$$

The average sound velocity can be found by,

$$v_m = [\frac{1}{3}(\frac{2}{v_t^3} + \frac{1}{v_l}^3]^{-\frac{1}{3}} \tag{2.62}$$

v_l and v_t are longitudinal and transverse sound velocity and these can be calculated from Navier's equation,

$$\begin{aligned} v_l &= (\frac{B + \frac{4G}{3}}{\rho})^{\frac{1}{2}} \\ v_t &= (\frac{G}{\rho})^{\frac{1}{2}} \end{aligned} \tag{2.63}$$

Similarly, for other crystal systems such as orthorhombic and tetragonal, the stiffness matrix is calculated first for a single crystal, and then using VRH approximations, the elastic properties of a polycrystal can be computed.

2.5 Electronic Properties

Electronic properties describe the state and behavior of electrons in the material. This study is crucial in identifying the materials as conductors, semiconductors, insulators, or superconductors. Furthermore, other properties such as electrical, transport, optical and

magnetic are coupled with the electronic properties for making the latter as the fundamental factor for the subtle evolution of the microscopic phenomena.

2.5.1 Band Structure

In an isolated atom, the electron energy levels are discretely represented by $1s$, $2s$,$2p$,... orbitals and electrons occupy these orbitals from the lowest energy levels first ($s < p < d < f$) with Pauli exclusion rule. When two atoms are brought closer together within their interaction distance, each energy level splits into two energy levels of slightly different energies. In a solid material, the density of atoms (number of atoms per unit cell volume) is in the range of 10^{23} atoms per cm^3. When such N number of atoms approach together to a distance of lattice constant, resulting in the formation of a solid, then each energy level splits into N energy levels forming a continuum. A set of such continuum energy levels is coined as an energy band. Each energy band can be occupied by $2N$ electrons. The probability distribution of electrons in energy levels at a given temperature T is governed by the Fermi-Dirac distribution function,

$$f(E) = \frac{1}{1 + exp[\frac{(\varepsilon - \mu)}{k_B T}]} \tag{2.64}$$

where, μ is the chemical potential and at $T = 0$, $\mu = E_F$, where E_F is the Fermi energy level. All energy levels below E_F are occupied and above E_F are empty, i.e.,

$$f(E) = \begin{cases} 1, & \text{if } E < E_F \\ 0.5, & \text{if } E = E_F \\ 0, & \text{if } E > E_F \end{cases} \tag{2.65}$$

In the lower energy band, the energy levels are tightly packed as they are closer to the nuclei. The width of the energy band for valence electrons is wider, which allows the electrons to be more itinerant and therefore, possess higher energy. This energy band is called the valence band and the conduction band is the next excited band, where the electrons are mobile. Between valence band and conduction band, there is an interval where electrons are forbidden or banned, called an energy gap or band gap. The knowledge of the band gap is important for the categorization of materials. Metals have zero band gap, semiconductors have a wide band gap and insulators have a comparatively wider band gap.

The quantum mechanical formulation yields deep insight into the description of band structure. In the case of free electron propagating in a zero potential, the Schrödinger equation is,

$$\frac{d^2\psi}{dx^2} + \frac{2m}{\hbar^2}E\psi = 0 \tag{2.66}$$

The wave function of $\psi(r) = Aexp(ikr)$ represents the state of a free electron, which yields the energy E as,

$$E(k) = \frac{\hbar^2 k^2}{2m} \tag{2.67}$$

which is a dispersion relation and represents the single band. In the free electron model, the band structure is not periodic, having an infinite Brillouin zone. In the phonon dispersion relation, we have seen that when the mass of the atoms vary, there are acoustic and optical branches. In the same way, adding periodic potential to represent the Coulomb attraction of the positive nuclei in the free electron model results in the origin of bands. The Schröndinger equation of a valence electron moving with a periodic crystal potential V can be written as,

$$\frac{d^2\psi}{dx^2} + \frac{2m}{\hbar^2}(E - V)\psi = 0 \tag{2.68}$$

and the energy level is described by Bloch wave function as shown earlier in Equation (2.25) and the energy as,

$$E(k) = (\frac{\hbar^2}{2m})|k+G|^2 \tag{2.69}$$

where, G is a reciprocal lattice vector. The Schrödinger equation with a periodic potential has been described by the Kronig-Penney model. Another suitable approximation for dispersion relation is obtained by the introduction of the effective mass. Analogous to the free energy model, the dispersion relation for a localized electron is approximated by,

$$E(k) = \frac{\hbar^2 k^2}{2m^*} \tag{2.70}$$

where, m^* is the effective mass. This is also a single band model and therefore, the dispersion relation in the valence band and the conduction band can be approximated as,

$$\begin{aligned} E(k) &= E_v - \frac{\hbar^2 k^2}{2m^*} \\ E(k) &= E_c + \frac{\hbar^2 k^2}{2m^*} \end{aligned} \tag{2.71}$$

where, E_v and E_c are constants and represent the band edges of the valence and the conduction band, respectively. The negative and positive signs describe hole and electron and their respective velocity in the band can be found as,

$$v_k = \frac{1}{\hbar}\frac{\partial E(k)}{\partial k} \tag{2.72}$$

The particle velocity is greater when the slope is higher, implying a greater overlap of the energy levels inside the band and smaller inertia or mass. The electron-hole pairs are collectively known as excitons. Moreover, the position of the band edges E_v and E_c further categorize materials as direct and indirect band gap materials.

In heavy elements, the relativistic consideration of electrons is prominent. The spin-orbit coupling should be taken into account as the total angular momentum of an electron J is the sum of angular momentum L and spin-angular momentum S, i.e., $\vec{J} = \vec{L} + \vec{S}$. The inclusion of spin-orbit coupling can split the band structure and bring degeneracy. The Rashba spin-orbit coupling factor $\alpha(\nabla V) \times p.\sigma$ is added as an extra potential in the Schrödinger equation, where α is the Rashba coupling, p is the momentum and σ is the Pauli matrix.

2.5.2 Density of States

We have seen earlier that the number of energy levels in a band is very large and dependent on the size of a material. Due to this limitation, it is necessary to calculate the number of energy levels or states per unit energy and per unit volume of real space. Analogous to the phonon density of states, the electronic density of states D is defined as the number of states N per unit energy E per unit volume V of the real space,

$$D = \frac{1}{V}\frac{dN}{dE} \tag{2.73}$$

The number of states inside the sphere of radius k in the phase space can be found in Equation (2.43). Instead, a factor of 2 is multiplied for two electronic states- spin up and spin down,

$$N = 2\frac{V}{V_s} = \frac{k^3 L^3}{3\pi^2} \tag{2.74}$$

The dispersion relation in Equation (2.67) yields the value of k as,

$$k = \frac{(2Em)^{\frac{1}{2}}}{\hbar} \tag{2.75}$$

and substituting it in Equation (2.73) gives the value of N as,

$$N = \frac{L^3(2m)^{\frac{3}{2}}E^{\frac{3}{2}}}{3\pi^2\hbar^3} \tag{2.76}$$

Finally, differentiating Equation (2.76) and using the result in Equation (2.73) yields,

$$D = \frac{1}{2\pi^2}(\frac{2m}{\hbar^2})^{\frac{3}{2}}E^{\frac{1}{2}} \tag{2.77}$$

And, the concentration of electrons n in the conduction band and holes h in the valence band can be found by integrating with the Fermi-Dirac distribution function as,

$$\begin{aligned} n &= \int_{E_c}^{\infty} D_c(E)f(E)dE \\ h &= \int_{-\infty}^{E_h} D_h(E)(1-f(E))dE \end{aligned} \tag{2.78}$$

where, D_c and D_h can be found from Equations (2.71) and (2.77) as,

$$\begin{aligned} D_c &= \frac{1}{2\pi^2}(\frac{2m}{\hbar^2})^{\frac{3}{2}}(E-E_c)^{\frac{1}{2}} \\ D_h &= \frac{1}{2\pi^2}(\frac{2m}{\hbar^2})^{\frac{3}{2}}(E_v-E)^{\frac{1}{2}} \end{aligned} \tag{2.79}$$

The product of *nh* gives the equation that is widely used in practical applications,

$$nh = 4(\frac{k_B T}{2\pi\hbar^2})^3 (m_c m_h)^{\frac{3}{2}} exp(\frac{-E_g}{k_B T}) \tag{2.80}$$

2.6 Optical Properties

Optical properties usually deal with the material's ability to respond to the incident electromagnetic radiation (ER). Based on this ability, materials are classified as transparent, translucent, and opaque. Depending on their metallic or non-metallic characters, several interesting properties are evolved due to exposure to ER. Recently, scientists from Tufts University have found new materials that move when exposed to ER [43]. ER is treated with particle nature rather than wave formulation, with quantized packets of energy called photons. The energy E associated with a photon is,

$$E = h\nu = \frac{hc}{\lambda} \tag{2.81}$$

where, symbols have their usual meaning.The interaction of ER with a material can be studied first hand, by determining the change in incident intensity (I_O), which is generally approximated as,

$$I_O = I_A + I_R + I_T \tag{2.82}$$

where, I_A, I_R and I_T are the intensity of absorbed, reflected, and transmitted ER, respectively. In terms of their coefficient, absorptivity ($A = \frac{I_A}{I_O}$), reflectivity ($R = \frac{I_R}{I_O}$) and transmissivity ($T = \frac{I_T}{I_O}$), Equation (2.82) is generally rewritten as,

$$A + R + T = 1 \tag{2.83}$$

On the other hand, the microscopic treatment of this interaction can be explained based on the band structure of materials. Two important phenomena- electronic polarization and electronic transitions may result due to interaction with ER. The electron absorbs energy imparted by the incident photon and as a result, ER gets retarded in velocity leading to another phenomenon called refraction, which is quantified by refractive index. If the absorbed energy is on par or greater than the band gap, then electronic transitions may occur, and the change in energy between unexcited state to the excited state is,

$$\Delta E = h\nu \tag{2.84}$$

The excited electron emits a photon and again comes to its unexcited state, leading to another phenomenon called luminescence. The color of a material is based on the frequency of the emitted ER. The next important quantity is the dielectric function, which is the fundamental microscopic property that associates the electronic structure with the optical phenomena. The incident ER, $E = E_0 exp(i\omega t)$ may cause the bound charges in the material to polarize and the process can be described by classical Maxwell's equations. Two equations that describe the dielectric function ε_r are mentioned here. The first one is,

$$\begin{aligned} D(r,\omega) &= \varepsilon(\omega)E(r,\omega) \\ &= \varepsilon_r(\omega)\varepsilon_0 E(r,\omega) \end{aligned} \tag{2.85}$$

where, D is the displacement vector $D = \varepsilon_0 E + P$, ε_0 is the dielectric constant of the vacuum and P is the polarization vector. The second equation is,

$$\varepsilon_r = n^2 \tag{2.86}$$

n being the refractive index. For a free electron in a uniform gas, the dielectric response can be modelled by solving,

$$m\frac{d^2x}{dt^2} = -eE \tag{2.87}$$

which gives,

$$\begin{aligned}\varepsilon_r(\omega) &= 1 - \frac{ne^2}{\varepsilon_0 m\omega^2} \\ &= 1 - \frac{\omega_p^2}{\omega^2}\end{aligned} \tag{2.88}$$

where, $\omega_p = \frac{ne^2}{\varepsilon_0 m}$ is the plasma frequency and this model is a good approximation for metal, which describes the intraband transition of electron due to ER absorption. However, in real materials, there is a damping effect, and in semiconductor and insulator, the valence electrons are bound or less itinerant than metal. The model shown by Equation (2.87) can be modified as,

$$m\frac{d^2x}{dt^2} + \gamma\frac{dx}{dt} + kx = -eE \tag{2.89}$$

where, γ is the damping parameter and k is the spring constant. It is interesting to note that the inclusion of the damping parameter changes the dielectric function as a complex variable, i.e., $\varepsilon_r = \varepsilon_1 - i\varepsilon_2$. Equation (2.89) can yield the real ε_1 and the imaginary ε_2 part of ε_r as,

$$\varepsilon_1 = 1 + \frac{ne^2}{\varepsilon_0 m}\frac{\omega_0^2 - \omega^2}{(\omega_0^2 - \omega^2)^2 + \gamma^2\omega^2} \tag{2.90}$$

$$\varepsilon_2 = \frac{ne^2}{\varepsilon_0 m}\frac{\gamma\omega}{(\omega_0^2 - \omega^2)^2 + \gamma^2\omega^2} \tag{2.91}$$

where, $\omega_0 = \sqrt{\frac{k}{m}}$. It should be noted that ε_1 converges to Equation (2.88), when $\omega_0 = 0$. This means that the incident photon with energy greater than $\hbar\omega$ will make the electrons less bound and shows an optically metallic character. Similarly, the refractive index function can be expressed as,

$$\hat{n} = n - ik \tag{2.92}$$

where, the real part n is refractive index and k is extinction coefficient. By virtue of Equation (2.86),

$$\begin{aligned} n(\omega) &= \{\frac{[\varepsilon_1^2(\omega) + \varepsilon_2^2(\omega)]^{\frac{1}{2}} + \varepsilon_1(\omega)}{2}\}^{\frac{1}{2}} \\ k(\omega) &= \{\frac{[\varepsilon_1^2(\omega) + \varepsilon_2^2(\omega)]^{\frac{1}{2}} - \varepsilon_1(\omega)}{2}\}^{\frac{1}{2}} \end{aligned} \tag{2.93}$$

The real part $\varepsilon_1(\omega)$ and imaginary part $\varepsilon_2(\omega)$ are related by the Kramers-Kronig relation,

$$\varepsilon_1(\omega) = 1 + \frac{2}{\pi}\int_0^\infty \frac{\omega'\varepsilon_2(\omega')}{\omega'^2 - \omega^2} d\omega' \tag{2.94}$$

CHAPTER 3

ENERGY GAP AND REFRACTIVE INDEX RELATIONS

This chapter presents a model which connects the energy gap with the refractive index in perovskites. The work has been published in Materials and can be available at " https://doi.org/10.3390/ma13081917". In less than a year, the article was read by more than one thousand people and cited more than half a dozen times.

3.1 Introduction

Perovskites are materials having the crystal structure of strontium titanate at room temperature ($SrTiO_3$) with a general formula for the oxide analogs of ABX_3, where A is a cation, generally a rare-earth- or alkali-type element, B is a transition metal cation, and X is an oxide or halide anion [18, 44, 45]. In recent years, there has been a growing interest among material scientists in the study of perovskites [46–48]. This is because perovskites exhibit a variety of functions such as piezoelectric, pyroelectric, ferroelectric, photovoltaic cells, LEDs, superconductivity, and topological insulators [49–52]. Generally, oxide perovskites exhibit good dielectric properties, and halide perovskites show excellent photonic properties [53, 54]. Since the discovery of calcium titanium oxide, $CaTiO_3$, by Gustav Rose in 1839, the research on perovskites remained dormant until the 21st Century [55,56]. The first paper on lead halide perovskites was published in 1892 [57]. The structure of $CsPbI_3$, cesium plumbo iodide, was studied in 1959 [58]. It is only in the last decade that perovskites have gained notoriety as materials for photovoltaic conversion. The paper "Organometal Halide Perovskites as Visible-Light Sensitizers for Photovoltaic Cells" by Kojima and Miyasaka et al. [26] has been the catalyst for the exponential growth of research on perovskite solar cells. Due to their inherent direct energy gap that matches the solar spectrum, halide perovskites continue to perform well as photonic materials [59, 60].

Moreover, the crystal structures of perovskites show different polymorphs [61–63], which further contribute to significant changes in their dielectric and photonic properties.

It is, therefore, crucial to understand the electronic and optical properties of perovskites to predict the behavior of these functionalities. Such predictions are useful to engineer these materials for various applications. Among several properties, the energy gap and the refractive index are fundamental entities whose correlation is vital for the understanding of the optoelectronic behavior of materials, as well as band-gap engineering [64–67]. While the threshold wavelength for the absorption of photons in semiconductors is determined by the energy gap, the transparency to incident spectral radiation is quantified by the refractive index. Such a correlation between these two fundamental properties is critical for the determination of the choice of semiconductors for applications in electronics and photonics [68]. Several studies about the relationship between the energy gap and the refractive index have been proposed for semiconductors and examined in the past, yielding various theories in this field [68–70]. There has been renewed interest in these studies in recent years [71–78]. While several manuscripts have reported on the studies of the energy gap and refractive index of perovskites [79–82], Blessing N. Ezealigo et.al. [83] performed a detailed experimental investigation into their research entitled "Method to control the optical properties: Band gap energy of mixed halide Organolead perovskites", and the results obtained have been interpreted by utilizing the single-oscillator model of Wemple–DiDomenico.

To the best of our knowledge and understanding, a detailed study of the correlations between the refractive index and energy gap for all inorganic perovskites is lacking in the literature. This is the first study of its kind being reported here. A comprehensive study of the fundamental properties such as the energy gap and refractive index is of paramount importance for the study of materials, in particular perovskites, since they are the basis for determining their applications in electronics and photonics. Furthermore, computational frameworks in materials science such as "propnet" [75] require pre-knowledge of the

database of these material properties. As materials informatics begins to grow, investigations such as these that relate two fundamental macroscopic properties will pave the way for new applications of perovskites.

3.2 Background

From a fundamental point of view, the refractive index of a material is simply defined as the ratio of the speed of light in a vacuum to that in the material. In general, the refractive index of a material is a function of (a) frequency and (b) doping, although studies in the literature report on the dependence of the refractive index on thickness [84], voids [85], grain boundaries [86], etc. In order to minimize such variation, it is good practice to consider a static refractive index, which is obtained from the time-independent electric field or the field at a zero wave vector. In 1950, Moss [87, 88] proposed the general relationship between the energy gap (E_g) and the refractive index (n) as,

$$n^4 E_g = 95eV \tag{3.1}$$

This model is based on the Bohr's atomic model of hydrogen. The assumption was that all energy levels in a solid are scaled down by a factor of $\frac{1}{\varepsilon_\infty^2}$, where ε_∞ is the optical dielectric constant satisfying the relation [89],

$$\varepsilon_\infty = n^2 \tag{3.2}$$

Since energy levels in a solid are quite complex and involve band structure theory, this gives rise to a structural restriction on Moss's relation. Based on the band structure, in 1962, Penn [90] proposed a model for an isotropic semiconductor by modifying Callaway's approximation of the dielectric constant with the inclusion of the Umklapp process and

showed the relation,

$$\varepsilon_\infty = 1 + (\hbar\omega_p/E_g)^2, \tag{3.3}$$

where ω_p is the plasma frequency [91]. Almost, in all semiconductors, the trajectories of valence and conduction bands are more or less parallel with each other, at least along the symmetry directions. With these considerations, Gupta and Ravindra [92] proposed that the difference between the Penn gap and the energy gap is constant and showed the linear relationships between the energy gap and the refractive index as [93],

$$n = 4.084 - 0.62E_g(eV) \tag{3.4}$$

However, Equation (3.4) puts an upper limit on the refractive index. In order to account for both the structural and the refractive index restriction of the Moss relation and the Ravindra relation, respectively, several empirical relations have been presented by various authors [70, 94, 95]. Based on the oscillatory theory, Herve and Vandamme [96] presented the relation,

$$n = \sqrt{1 + (\frac{A}{E_g + B})^2} \tag{3.5}$$

where $A = 13.6$ eV and $B = 3.4$ eV are the constants. Though this relation is quite superior and agrees satisfactorily for most optoelectronic materials, it has shortcomings for materials of the IV-VI group [97].

In light of these drawbacks, this study examines the correlations between the energy gap and the refractive index in perovskites. Utilizing the Wemple–DiDomenico single electron oscillator approximation [98] and based on the structure of perovskites, a simple relation is proposed for such ternary systems. Later, this model is compared with the

Moss (Equation (3.1)), Ravindra (Equation (3.4)), and Herve–Vandamme (Equation (3.5)) models, as well as the reported experimental values of the refractive indices of perovskites in the literature.

3.3 Theory

The dependence of the refractive index (n) on the wavelength (λ) or frequency (ν) has been well described by dispersion relations. The first dispersion relation was developed by Cauchy [99],

$$n(\lambda) = A + \frac{B}{\lambda^2} + \frac{C}{\lambda^4} \tag{3.6}$$

where A, B, and C are constants. The Cauchy dispersion relation is simply an empirical fitting and bears no physical significance. A more significant dispersion model was given by Sellmeier [100],

$$n^2(\lambda) = 1 + \Sigma_i \frac{A_i \lambda^2}{\lambda^2 - \lambda_i^2} \tag{3.7}$$

where, A_i is a constant and subscript i denotes the multiple resonant wavelengths. The Sellmeier dispersion relation represents a more realistic model as whenever the electric field is impinged on a material, the electron clouds get disturbed by it, and the nuclei exert a restoring force, yielding the possibilities of multiple excitation. Since both of these Cauchy and Sellmeier relations are empirical, the concrete formulation for the dispersion relation was given by the Drude–Lorentz electronic theory [101]. This theory assumes that the electric field applied on an electron bound to the nucleus exerts Hooke's force. Based on this model, it was found that the refractive index is associated with the oscillator strength (C_i) by [102],

$$n^2(\omega) = 1 + \frac{Ne^2}{2\pi m} \Sigma_i \frac{C_i}{\omega_i^2 - \omega^2} \tag{3.8}$$

where, N is the particle density, e and m are the charge and mass of the electron, and ω_i and ω are the absorption and incident frequency, respectively. For a single oscillator, Wemple and DiDomenico introduced the semi-empirical relationship of the form [103, 104],

$$n^2(\nu) - 1 = \frac{E_d E_o}{E_o^2 - (h\nu)^2} \tag{3.9}$$

where, ν is the frequency, h is the Planck constant, E_o is the single oscillator energy, and E_d is the dispersion energy. The dispersion energy measures the average strength of interband optical transitions and is given by [103, 104],

$$E_d = \beta N_c N_e Z_a (eV), \tag{3.10}$$

where, N_c is the coordination number of the cation, N_e is the effective number of valence electrons per anion, Z_a is the formal charge of the anion, and β is a constant having the value 0.26 $\pm$ 0.04 eV for ionic compounds and 0.37 $\pm$ 0.05 eV for covalent compounds. Furthermore, based on the experimental data tested on several materials, it has been estimated empirically that the oscillator energy is related to the lowest energy gap by [103, 104],

$$E_o \approx 1.5 E_g \tag{3.11}$$

where, E_g is the lowest direct band gap. Using the values of N_c, N_e, Z_a, and β for the perovskite structure in Equations (3.9), (3.10) and (3.11), the Wemple and DiDomenico

form for the static refractive index ($n(0)$ or simply n) can be written as,

$$n = \sqrt{1 + \frac{16.64eV}{E_g}} \tag{3.12a}$$

$$n = \sqrt{1 + \frac{8.32eV}{E_g}} \tag{3.12b}$$

for oxide perovskites and halide perovskites, respectively.

These Equations, (3.12a) and (3.12b), are based on the fact that the optoelectronic properties of perovskites are dependent on the ionic nature of the bonds or by simply treating perovskites as ionic solids. It is unambiguously known today that the octahedral cage in perovskites is formed by the heteropolar bonds (mixed ionic/covalent interactions) among the B cation and X anions, whereas the cation A shows electrostatic interaction with this cage [21, 105]. A majority of the school of thought claims that the properties of perovskites are dependent on the octahedral cage built from the interaction of $B-X$ ions, and the role of cation A is merely for the charge neutrality of the final stable structure [106, 107]. In other words, the properties of perovskites evolve from the octahedral frame of $B-X$ ions, and the cation A affects those properties by distorting this frame. Moreover, this claim can be justified by the Pauling rule [108], as in a multication system, cations with high valency and a small coordination number (CN) form polyhedra with the anion and the cation with low valency and a high coordination number (CN) adjusting their positions for final stability. The cation/anion ratio, as suggested by Pauling, determines the coordination number (CN), which in turn determines the structure of the polyhedra. In the case of perovskites, we take the cation/anion ratio as the average ratio for two cations, i.e., $\frac{(\frac{r_A}{r_X}+\frac{r_B}{r_X})}{2}$, where r_A, r_B, and r_X are the ionic radii of A, B, and X at CNs 12, 6, and 2, respectively [109].

Henceforth, one can paraphrase that the properties of perovskites are dependent on the octahedral cage created by $B-X$ ions, and the adjustments of cation A for the final

stable structure may lead to distorting this octahedral frame, which in turn influences these properties. Furthermore, the distortion of the octahedral cage induced by cation A may depend on the covalent nature of the $B-X$ bond [110, 111]. The greater the covalent $B-X$ bond, the less is the distortion of the structure of ABX_3. Finally, incorporating the covalent nature of the $B-X$ bond with the adjustment of A for the final stable structure, we propose the following modification of the Wemple and DiDomenico form,

$$n = \sqrt{1 + \frac{(r_A + r_B)}{r_X} \frac{11.84eV}{E_g}} \tag{3.13a}$$

$$n = \sqrt{1 + \frac{(r_A + r_B)}{r_X} \frac{5.92eV}{E_g}} \tag{3.13b}$$

for oxide perovskites and halide perovskites, respectively.

3.4 Results and Discussion

I. Validity of the model: Based on Equations (3.13a) and (3.13b), we calculated the refractive index values of various oxide perovskites and halide perovskites. The results were then compared with the literature values obtained from various sources as shown in Table 3.1, and the resulting data are further plotted in Figure 3.1. One can notice that the computed results using Equations (3.13a) and (3.13b) were in agreement with the corresponding literature values. These could further be compared with the values obtained from the Wemple–DiDomenico relation, Moss relation, Ravindra relation, and Herve–Vandamme relation. It must be noted that the reference values of the refractive index were not homogeneous in terms of the wavelength used, whereas the refractive index calculated by Equations (3.13a) and (3.13b) corresponded to the static or low-frequency values. Thus, this factor may contribute to some error during the comparison. Furthermore, we calculated the absolute accuracy error ($AAE = |X_{standard} - X_{calculated}|$) and mean absolute error ($MAE = average(AAE)$) to reckon the deviation of the proposed relation

along with the other established relations with their corresponding refractive indices. It can be seen that the proposed model showed a mean absolute error of 0.07, which was the smallest of all the other established models.

II. Consistency of the model: As mentioned above, the experimental values of the direct energy gap and the refractive index values at low frequency are not frequently available for various perovskite materials. Moreover, the searched values were not as unique as they depended on the experimental methods used in the literature. Further, a few papers mentioned the phases and distortion of the structure before measuring the energy gap. Such inconsistency may impede the validity of the model. In order to remove such inconsistency, the energy gap values were taken from one common source [112] obtained from density functional theory (DFT) using the HSE (Heyd–Scuseria–Ernzerhof) functional. The results are shown in Tables 3.2 and 3.3. We also included some available values of the refractive index in the last columns of these tables. They can serve as a reference and may be used with caution in comparing with other computed values.

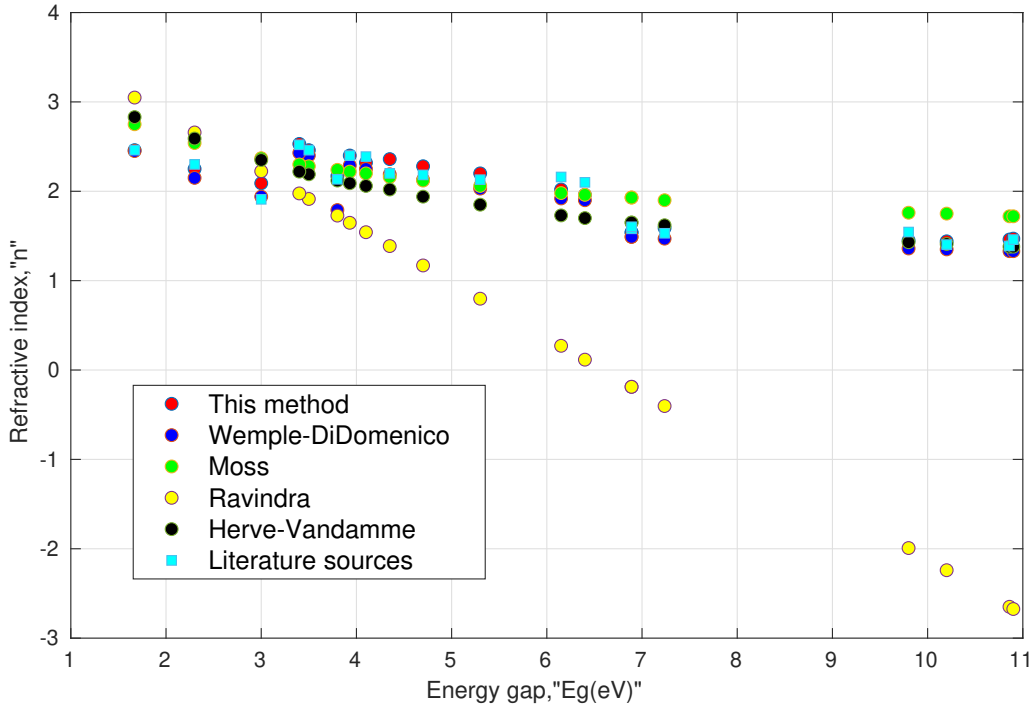

Figure 3.1 Comparison of various models with available literature data for perovskites, shown in Table 3.1.

This is because of the fact that all the computed values of the refractive indices are a function of their respective energy gaps, and it is well known that the computed energy gaps using HSE underestimate the actual energy gaps [113]. Moreover, their structural phases may not be the same. For instance, in Table 3.3, the value of the refractive index (as shown by the last column) for orthorhombic (Pnma) $CsNaF_3$ is 4.56, whose energy gap is 0.019 eV as calculated by DFT using the GGA (generalized gradient approximation) functional, whereas the energy gap for cubic (Pm3m) $CsNaF_3$ is 0.26 eV using the HSE functional. Our model predicted a higher value of the refractive index for the energy gap close to zero, which was consistent for conducting materials. These results can be seen in Figures 3.2 and 3.3. At higher energy gaps, this model converged with the Wemple–DiDomenico, Moss, and Herve–Vandamme models. One can notice that the prediction of the refractive index by the Ravindra relation showed negative values when the corresponding energy gaps were above 6.6 eV.

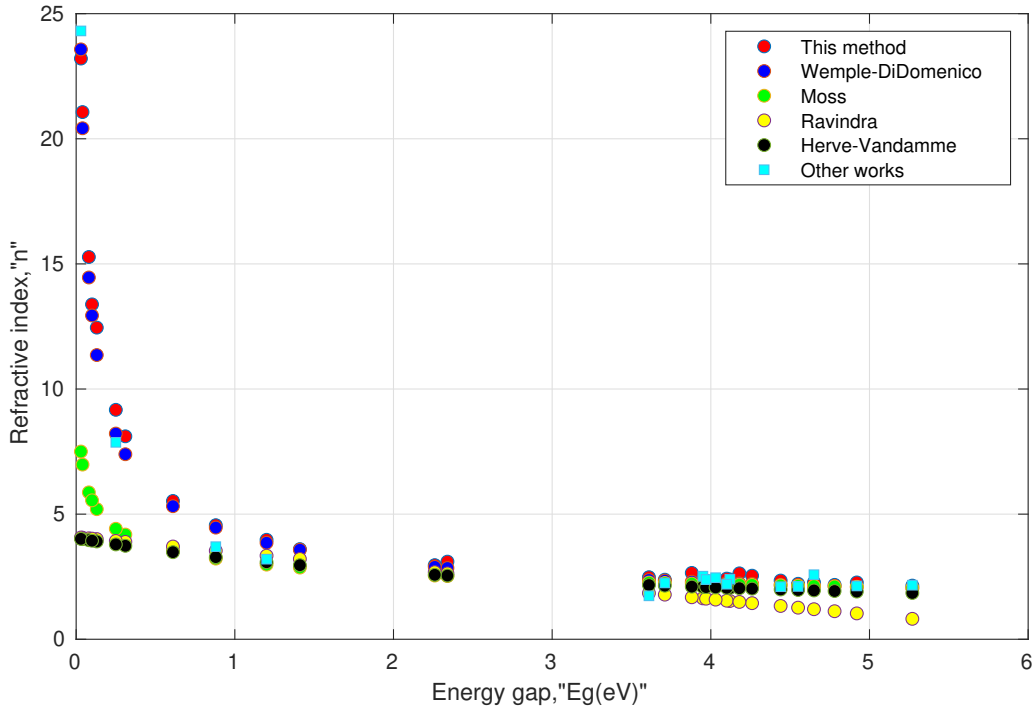

Figure 3.2 Simulated behavior of various models for oxide perovskites, shown in Table 3.2.

Table 3.1 Comparison of Refractive Indices Computed by Various Models with Literature Values, AAE, Absolute Accuracy Error

Perovskite ABX_3	**Energy Gap** $'E_g(eV)'$	**Refractive Index** $'n'$	**This Method** (Eqs. (3.13a),(3.13b))	**AAE**	**Wemple-DiDomenico Relation** (Eqs. (3.12a),(3.12b))	**AAE**	**Moss Relation** (Eq. (3.1)	**AAE**	**Ravindra Relation** (Eq. (3.4))	**AAE**	**Herve-Vandamme Relation** (Eq. (3.5))	**AAE**
$SrTiO_3$	4.1 [114]	2.388(632.8 nm) [114]	2.32	0.07	2.25	0.14	2.20	0.19	1.54	0.85	2.06	0.33
$SrSnO_3$	3.93 [115]	≈2.4 [116]	2.40	0.00	2.29	0.11	2.22	0.18	1.65	0.75	2.09	0.31
$KMgF_3$	10.2 [117]	1.404 (632.8 nm) [114]	1.44	0.04	1.35	0.05	1.75	0.35	*N.V.*	*N.D.*	1.41	0.01
$CaTiO_3$	3.5 [118]	≈ 2.46 [119]	2.46	0.00	2.40	0.06	2.28	0.18	1.91	0.55	2.19	0.27
$PbTiO_3$	3.4 [120]	2.52 [121]	2.53	0.01	2.43	0.09	2.30	0.22	1.98	0.54	2.22	0.3
$CsPbF_3$	3.8 [122]	2.134 (5.7eV) [122]	2.17	0.04	1.79	0.34	2.24	0.11	1.73	0.40	2.12	0.01
$CsPbI_3$	1.67 [123]	2.46 (435nm) [123]	2.46	0.00	2.45	0.01	2.75	0.29	3.05	0.59	2.83	0.37
$KTaO_3$	4.35 [124]	2.2(632.8 nm) [114]	2.36	0.16	2.19	0.01	2.16	0.04	1.39	0.81	2.02	0.18
$CsPbBr_3$	2.3 [125]	≈2.3 (580nm) [126]	2.25	0.05	2.15	0.15	2.54	0.24	2.66	0.36	2.59	0.29
$CsPbCl_3$	3.0 [125]	≈1.91 [127]	2.09	0.18	1.94	0.03	2.37	0.46	2.22	0.31	2.35	0.44
$LiTaO_3$	4.7 [128]	≈2.183 (632.8nm) [114]	2.28	0.10	2.13	0.05	2.12	0.06	1.17	1.01	1.94	0.24
$BaZrO_3$	5.30 [129]	2.13 [130]	2.20	0.07	2.03	0.10	2.06	0.07	0.80	1.33	1.85	0.28
$SrZrO_3$	6.15 [129]	2.16 [15]	2.02	0.14	1.92	0.24	1.98	0.18	0.27	1.89	1.73	0.43
$CaZrO_3$	6.40 [129]	2.1 [131]	1.96	0.14	1.90	0.20	1.96	0.14	0.12	1.98	1.70	0.4
$KCaF_3$	10.86 [132]	1.388(583.9nm) [102]	1.46	0.07	1.33	0.06	1.72	0.33	*N.V.*	*N.D.*	1.38	0.01
$LiBaF_3$	9.8 [117]	1.544(632.8 nm) [114]	1.45	0.09	1.36	0.18	1.76	0.22	*N.V.*	*N.D.*	1.43	0.11
$KZnF_3$	7.237 [133]	1.53(583.9nm) [102]	1.59	0.06	1.47	0.06	1.90	0.37	*N.V.*	*N.D.*	1.62	0.09
$RbCaF_3$	10.9 [134]	1.46 [135]	1.47	0.01	1.33	0.13	1.72	0.26	*N.V.*	*N.D.*	1.38	0.08
$CsCaCl_3$	6.89 [136]	1.58,1.603(583.9nm) [102, 136]	1.54	0.04, 0.06	1.49	0.09, 0.11	1.93	0.35, 0.33	*N.V.*	*N.D.*	1.65	0.07, 0.05
N.V. represents a negative value		*MAE*		0.07		0.11		0.23		0.87		0.21
N.D. represents not defined												

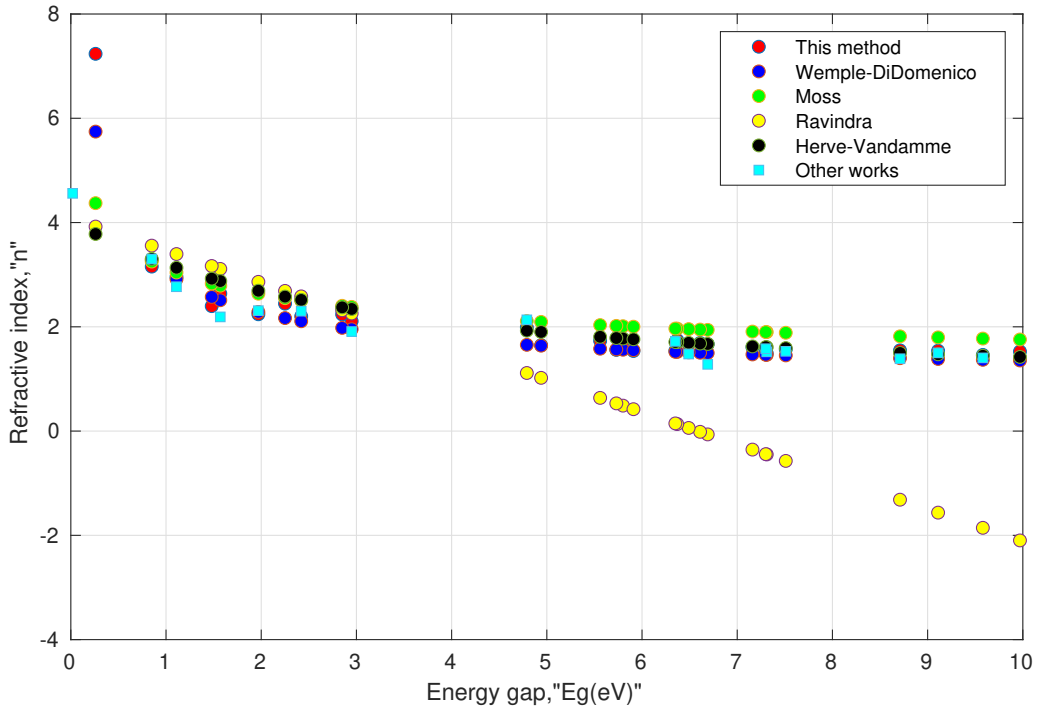

Figure 3.3 Simulated behavior of various models for halide perovskites, shown in Table 3.3.

This could be attributed to the non-parallelism in the trajectories of valence and conduction bands along the symmetry directions in perovskites [137–139]. Overall, the tabulated values indicated that Equations (3.13a) and (3.13b) were consistent enough for oxide perovskites and halide perovskites.

So far, we have seen that the proposed model not only predicts the refractive index of the perovskites with sufficient accuracy, but also shows a consistent behavioral pattern with some of the well-established models. However, it may not be appropriate to claim that the new formula is superior to these established models. First of all, the Wemple–DiDomenico model, Moss model, Ravindra model, and Herve–Vandamme model can be applied to all kinds of materials. However, the behavior of these models depends on various factors such as the types of bonds, the energy gaps, the nature of the materials such as unary, binary, or ternary, etc. Secondly, all these models take a single argument, i.e., the smallest direct energy gap to compute the corresponding static refractive index. However, the proposed new formula could be applicable only to perovskites, and it takes two arguments: one is a

Table 3.2 Energy Gap of Various Oxide Perovskites with Their Corresponding Refractive Indices Computed from Various Models

Oxide perovskite ABO3	**Energy gap (HSE)** $'E_g(eV)'$ [112]	$\frac{(\frac{r_A}{r_X}+\frac{r_B}{r_X})}{2}$ **[140]**	**This method** (Eq. (3.13a))	**Wemple–DiDomenico Relation** (Eq. (3.12a))	**Moss Relation** (Eq. (3.1))	**Ravindra Relation** (Eq. (3.4))	**Herve–Vandamme Relation** (Eq. (3.5))	**Other works**
$PbTiO_3$	3.95	0.78	2.38	2.28	2.21	1.64	2.09	$\approx$ 2.52 [121]
$BaNbO_3$	0.31	0.85	8.11	7.39	4.18	3.89	3.73	–
$BaTiO_3$	4.12	0.82	2.39	2.24	2.19	1.53	2.05	$\approx$ 2.4 [141]
$KTaO_3$	4.1	0.84	2.42	2.25	2.19	1.54	2.06	$\approx 2.2(632.8nm)$ [114]
$NaNbO_3$	4.55	0.75	2.22	2.16	2.14	1.26	1.97	$\approx$ 2.11 [142]
$SrFeO_3$	1.2	0.75	3.97	3.86	2.98	3.34	3.08	$\approx$ 3.2 [143]
$SrVO_3$	0.04	0.75	21.07	20.42	6.98	4.06	4.00	–
$KTcO_3$	0.13	0.85	12.45	11.36	5.20	4.00	3.91	–
$TlIO_3$	4.26	0.98	2.54	2.21	2.17	1.44	2.02	–
$CsIO_3$	4.18	1.05	2.63	2.23	2.18	1.49	2.04	–
$CaFeO_3$	1.41	0.71	3.60	3.58	2.87	3.21	2.96	–
$BaZrO_3$	4.92	0.86	2.27	2.09	2.09	1.03	1.90	$\approx$ 2.13 [130]
$BaSnO_3$	2.34	0.85	3.10	2.85	2.52	2.63	2.54	–
$KNbO_3$	4.44	0.84	2.35	2.18	2.15	1.33	1.99	$\approx$ 2.1 [141]
$SrTiO_3$	3.97	0.76	2.35	2.28	2.21	1.62	2.08	$\approx 2.388(632.8nm)$ [114]
$RbIO_3$	3.88	0.99	2.65	2.30	2.22	1.68	2.10	–
$BaBiO_3$	0.25	0.88	9.17	8.22	4.42	3.93	3.79	7.87^* [144]
$SrNbO_3$	0.08	0.79	15.28	14.46	5.87	4.03	3.96	–
$SrCrO_3$	0.61	0.76	5.53	5.32	3.53	3.71	3.48	–
$PbZrO_3$	4.65	0.82	2.27	2.14	2.13	1.20	1.95	$\approx$ 2.58 [145]
$NaTaO_3$	4.78	0.75	2.17	2.12	2.11	1.12	1.93	–
$LaNiO_3$	0.03	0.68	23.21	23.57	7.50	4.07	4.01	24.31^{**} [146]
$AgTaO_3$	3.61	0.79	2.48	2.37	2.26	1.85	2.17	$\approx$ 1.736 [147]
$SrZrO_3$	5.27	0.80	2.14	2.04	2.06	0.82	1.85	$\approx$ 2.16 [15]
$LaCrO_3$	3.71	0.73	2.38	2.34	2.25	1.78	2.14	$\approx$ 2.25 [148]

Table 3.2 Energy Gap of Various Oxide Perovskites with Their Corresponding Refractive Indices Computed from Various Models

Oxide perovskite ABO3	**Energy gap (HSE)** $'E_g(eV)'$ [112]	$\frac{(\frac{r_A}{r_X}+\frac{r_B}{r_X})}{2}$ **[140]**	**This method** (Eq. (3.13a))	**Wemple–DiDomenico Relation** (Eq. (3.12a))	**Moss Relation** (Eq. (3.1))	**Ravindra Relation** (Eq. (3.4))	**Herve–Vandamme Relation** (Eq. (3.5))	**Other works**
$LaMnO_3$	2.26	0.74	2.96	2.89	2.55	2.68	2.58	–
$CaTiO_3$	4.03	0.74	2.32	2.26	2.20	1.59	2.07	≈ 2.46 [119]
$LaTiO_3$	0.1	0.75	13.38	12.94	5.55	4.02	3.94	–
$SrCoO_3$	0.88	0.74	4.56	4.46	3.22	3.54	3.28	≈ 3.7 [143]

$*$ Estimate based on reflectivity of 0.6 at 0 K; ** estimate based on reflectivity of 0.85 at 0 K.

Table 3.3 Energy Gap of Various Halide Perovskites with Their Corresponding Refractive Indices Computed from Various Models

Halide Perovskite ABX3	**Energy Gap (HSE)** $'E_g(eV)'$ [112]	$\frac{(\frac{r_A}{r_X}+\frac{r_B}{r_X})}{2}$ **[140]**	**This method** (Eqs. (3.13b))	**Wemple–DiDomenico Relation** (Eqs. (3.12b))	**Moss Relation** (Eq. (3.1))	**Ravindra Relation** (Eq. (3.4))	**Herve–Vandamme Relation** (Eq. (3.5))	**Other works**
$TlZnF_3$	5.8	0.95	1.71	1.56	2.01	0.49	1.78	–
$CsSnCl_3$	1.57	0.79	2.64	2.51	2.79	3.11	2.88	≈ 2.19 [149]
$CsGeI_3$	1.48	0.59	2.40	2.57	2.83	3.17	2.92	–
$KMgF_3$	9.58	0.92	1.46	1.37	1.77	*N.V.*	1.44	$\approx 1.404(632.8nm)$ [114]
$KCdF_3$	6.69	1.01	1.67	1.50	1.94	*N.V.*	1.67	≈ 1.28 [136]
$RbZnF_3$	7.16	0.96	1.61	1.47	1.91	*N.V.*	1.62	–
$RbCaF_3$	9.11	1.06	1.54	1.38	1.80	*N.V.*	1.47	≈ 1.5 [150]
$RbCdF_3$	6.61	1.04	1.69	1.50	1.95	*N.V.*	1.68	–
$RbCaCl_3$	7.31	0.76	1.49	1.46	1.90	*N.V.*	1.61	≈ 1.52 [150]
$RbMnF_3$	6.49	0.99	1.68	1.51	1.96	0.06	1.69	≈ 1.478 [102]
$CsNaF_3$	0.26	1.13	7.24	5.74	4.37	3.92	3.78	4.56* [15, 112]
$TlCdBr_3$	5.91	0.68	1.54	1.55	2.00	0.42	1.76	–
$RbNiF_3$	5.56	0.94	1.73	1.58	2.03	0.64	1.81	–
$CsCaF_3$	9.97	1.12	1.53	1.35	1.76	*N.V.*	1.42	–
$CsPbF_3$	4.79	1.19	1.99	1.65	2.11	1.11	1.93	$\approx 2.134(5.7eV)$ [122]
$CsSnBr_3$	1.11	0.72	2.96	2.91	3.04	3.39	3.13	≈ 2.769 [149]
$CsCdF_3$	6.37	1.10	1.74	1.52	1.96	0.13	1.70	–
$KZnF_3$	7.51	0.93	1.57	1.45	1.88	*N.V.*	1.59	$\approx 1.53(583.9nm)$ [102]
$CsCaCl_3$	7.3	0.80	1.52	1.46	1.90	*N.V.*	1.61	$\approx 1.58, 1.603(583.9nm)$ [102, 136]
$CsGeBr_3$	1.97	0.67	2.24	2.28	2.63	2.86	2.69	≈ 2.31 [151]
$CsPbBr_3$	2.42	0.79	2.20	2.11	2.50	2.58	2.52	$\approx 2.3(580nm)$ [126]
$CsCaBr_3$	6.35	0.74	1.54	1.52	1.97	0.15	1.71	≈ 1.72 [15]
$CsPbCl_3$	2.95	0.86	2.11	1.95	2.38	2.25	2.34	≈ 1.91 [127]
$CsSnI_3$	0.85	0.64	3.15	3.28	3.25	3.56	3.30	≈ 3.3 [149]
$KCaF_3$	8.71	1.03	1.55	1.40	1.82	*N.V.*	1.50	$\approx 1.388(583.9nm)$ [102]

Table 3.3 Energy Gap of Various Halide Perovskites with Their Corresponding Refractive Indices Computed from Various Models

Halide Perovskite ABX3	**Energy Gap (HSE)** $'E_g(eV)'$ [112]	$\frac{(\frac{r_A}{r_X}+\frac{r_B}{r_X})}{2}$ **[140]**	**This method** (Eqs. (3.13b))	**Wemple–DiDomenico Relation** (Eqs. (3.12b))	**Moss Relation** (Eq. (3.1))	**Ravindra Relation** (Eq. (3.4))	**Herve–Vandamme Relation** (Eq. (3.5))	**Other works**
$KMnCl_3$	5.73	0.69	1.56	1.56	2.02	0.53	1.78	–
$TlFeF_3$	2.85	0.96	2.24	1.98	2.40	2.32	2.37	–
$LiSnCl_3$	4.94	0.72	1.65	1.64	2.09	1.02	1.90	–
$TlCuF_3$	2.25	0.95	2.44	2.17	2.55	2.69	2.58	–

N.V. represents a negative value; * orthorhombic lattice, $E_g = 0.019$ eV.

structural parameter, quantified as the cation-anion ratio, and the other is the energy gap. Generally, perovskites are sensitive to an external stimulus, and therefore, the question of the stability of this structure is very crucial as many electro-optical properties depend on the evolution of the lattice. Therefore, one cannot solely depend on Wemple–DiDomenico model, Moss model, Ravindra model, and Herve–Vandamme model for perovskites as these models isolate structural reformation.

3.5 Conclusions

In summary, this study presented a new model to correlate the refractive index with the energy gap in perovskites. This model was tested on various oxide perovskites and halide perovskites, and the results obtained were in accord with some established models, as well as the literature values. All these models facilitated the calculation of the static refractive index based on the transition of valence electrons to the conduction band after absorbing the threshold photon energy, and henceforth, all these were discrete models. The efficacy of the proposed model was that it represented the correct picture of optical and electronic properties depending on the structural evolvement in perovskites. It took account of both structural distortion and the covalent nature of the B-X bond that were responsible for the fluctuations of the optoelectronic properties. Moreover, it is a well-established fact that the optoelectronic properties are susceptible to the structural reorganization in perovskites. Therefore, the more precise the measurement of the cation/anion ratio, the more accurate will be the correlation predicted by this model.

CHAPTER 4

DENSITY FUNCTIONAL STUDY OF ZIRCONATE PEROVSKITES

Zirconate perovskites are known for their ionic conductivity. First principles study are performed to analyze the structural, elastic, electronic and optical properties of zirconate perovskites. The effects of alkaline earth metal cation substitution on their overall properties are further investigated. The calculations are performed using the projector augmented wave (PAW) within GGA-PBE and HSE06 formalism. The obtained results not only predict the properties in accord with the experimental ones, but also compare the efficacy of these two functionals. These results are published in the Journal of Physics Communications and can be found at "https://iopscience.iop.org/article/10.1088/2399-6528/abe9fd/pdf".

4.1 Introduction

Perovskite materials exhibit numerous functionalities such as piezoelectric, ferroelectric, ferromagnetic and pyroelectric. They are utilized in photovoltaic cells, LEDs, superconductivity, colossal magneto-resistance and topological insulators [49–52, 152]. Generally, oxide perovskites display good dielectric properties, halide perovskites are good photonic materials and chalcogenide perovskites exhibit applications in energy harvesting, solid-state lighting and sensing [53, 54, 153]. In recent decades, there has been keen interest in zirconate perovskites as these materials are known for good proton conductivity and thus have potential uses for fuel cells or hydrogen sensors [154, 155]. Moreover, due to their high thermal stability, zirconate perovskites are often regarded as potential candidates for thermal barrier coating materials [156].

Significant experimental work has been done to study different types of zirconate perovskites, establishing that injecting small dopant into these materials can result in ionic conduction behaviour [157,158]. From a theoretical perspective, commonly first-principles

based DFT calculations, the study of zirconate perovskites has been implemented from the beginning of the twenty-first century. In 2005, Terki et al [156] have studied the structural, elastic and electronic properties of $BaZrO_3$ and $SrZrO_3$ using Perdew-Burke-Ernzerhof (PBE) functional [41, 159]. Likewise, Hou (2008) [160] and Stoch et al (2011) [161] have investigated cubic and orthorhombic phases of $CaZrO_3$, using PBE functional. Similarly, Shawahni et al (2018) [162] have studied $SrRhO_3$ and $SrZrO_3$ compounds, using PBE functional. Furthermore, one can notice from the literature that there are numerous DFT based studies performed on different zirconate perovskites. Using PBE functional for investigation, especially of optoelectronic properties, is always dubious as this functional underestimates the band gap by more than 40% [163, 164]. This is because standard functionals such as PBE have intrinsic self-interaction errors which treat electrons to be more itinerant. Therefore, it is often not suitable to use PBE functional for localized systems such as defects, d and f block elements. To overcome such shortcomings, usually Heyd-Scuseria-Ernzerhof hybrid functional (HSE) [165] approach is incorporated with standard calculations. The HSE functional rectifies the self-interaction error to some extent by mixing some portion of Hartree-Fock (HF) exact exchange with the exchange part of PBE. DFT calculations using HSE can thus give more reliable results other than standard functionals [166], though, the choice of functionals along with the accuracy of calculations depend on both atomistic systems and the availability of computing resources. HSE functional is an improvement over another hybrid functional PBE0 [167, 168]. Due to problematic convergence of long-range mix of HF exact exchange in PBE0, HSE utilizes the screening parameter that allows the short-range mix between non-local HF exchange with local PBE exchange. Here, we have used standard HSE functional, called HSE06, which incorporates 25% Hartree-Fock (HF) exact exchange α, screening parameter w of 0.21 $\AA^{-1}$ and 100% correlation energy from PBE [169]. The magnitude of the screening parameter is crucial in predicting the accurate electronic structure of a material. It should be noted that HSE06 functional converges to PBE0 and PBE whenever $\omega \to 0$ and $\omega \to \infty$

respectively. Besides these functionals, we have also tested another functional PBEsol, which is quite popular for structure prediction [170, 171].

The principal aim of this study is to perform a comprehensive study of the cubic phase of $AZrO_3$ ($A = Ca, Sr, Ba$). Their structural, elastic, electronic and optical properties are predicted not only by using PBE functional but also with HSE06 functional. Throughout this chapter, it is believed that one can easily trace the computational difference between these two functionals. Further, the effect of variation of cation A on the overall properties of these materials can also be examined. To the best of our knowledge, the simultaneous investigation of calcium zirconate, strontium zirconate and barium zirconate perovskites using both PBE and HSE06 functionals is the first of its kind in the literature.

4.2 Computational Details

The investigation of structural, elastic, electronic and optical properties of alkaline-earth metal zirconate perovskites was executed through Density Functional Theory (DFT) as implemented in the Vienna Ab initio Simulation Package (VASP) [29, 30]. The projector augmented wave (PAW) [172, 173] method considers the valence states $3s^2 3p^6 4s^2$ for Ca, $4s^2 4p^6 5s^2$ for Sr, $5s^2 5p^6 6s^2$ for Ba, $4s^2 4p^6 4d^2 5s^2$ for Zr and $2s^2 2p^4$ for O while the remaining core states are considered to be frozen with the ion's environment. The cut-off energy for plane-wave basis sets was set at 520 eV (1.3 times the maximum cut-off energy) and the k-points grid for Brillouin-zone integration was set as $24 \times 24 \times 24$ for all PBE calculations and $4 \times 4 \times 4$ for HSE06 calculations. Only exception was made for the calculations of the dielectric functions where the k-points grid was set as $12 \times 12 \times 12$. The criteria for the convergence tolerance of self-consistent calculations was set as 10^{-6} eV for total energy and 0.015 eV/Å for force.

4.3 Results and Discussion

4.3.1 Structural Properties

The cubic structure of alkali-earth metal zirconate perovskite $AZrO_3$ (A=Ca, Sr and Ba) with space group $Pm3m$ is shown in Figure 4.1.

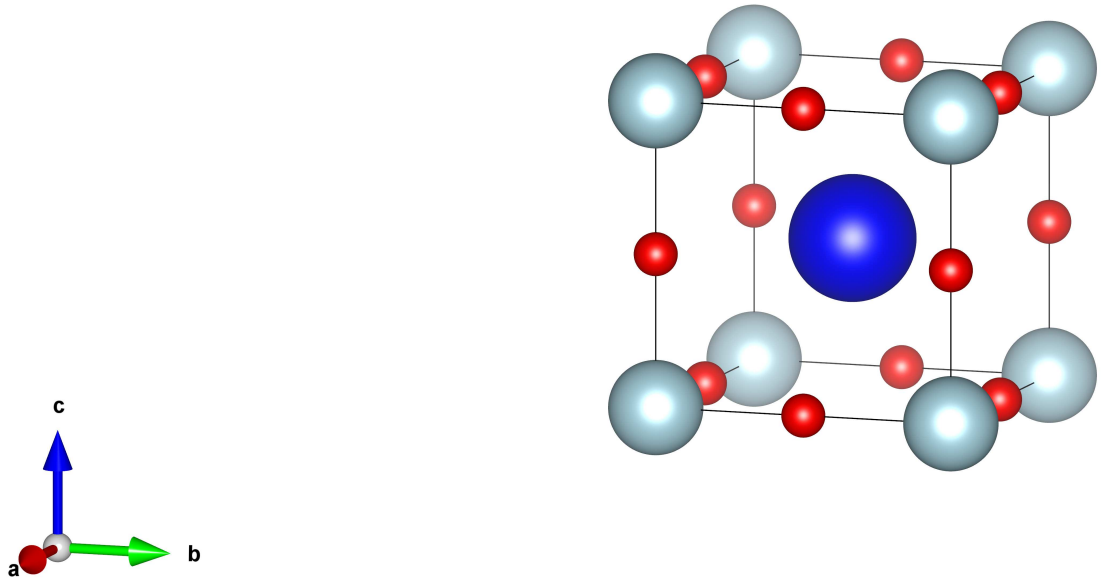

Figure 4.1 The cubic unit cell of $AZrO_3$, where A, Zr and O atoms are shown by blue, cyan and red colors, respectively.

The initial structures of $AZrO_3$ are taken from the materials project databases [15]. The geometrical positions of the elements in the primitive unit cell are: A (1/2,1/2,1/2), Zr (0,0,0) and O (0,1/2,0), (0,0,1/2), (1/2,0,0). The obtained lattice constants and bond lengths computed using PBE and HSE06, along with their respective available literature values are shown in Table 4.1. Both of these functionals overestimate the lattice constant. Lattice constants are also calculated using functionals PBEsol and PBE0. It can be seen that the PBEsol greatly reduces the overestimation of PBE, and can be used as an alternative to computationally expensive hybrid functionals. Moreover, the structure predicted by hybrid functional PBE0 indicates that the lattice parameters are insensitive to the screening factor. In the case of $CaZrO_3$ and $SrZrO_3$, there is a significant difference in computed values

Table 4.1 Calculated Values of Lattice Constant (a_0) and Bond Length (d) along with Their Experimental Values

	a_0(Å)					
Materials	*PBE*	*PBEsol*	*PBE*0	*HSE*06	*Literature*	d(Å) *PBE*;*HSE*06
$CaZrO_3$	4.14	4.10	4.10	4.10	4.02 [174]	$d_{Ca-O} = 2.93; 2.90$ $d_{Zr-O} = 2.07; 2.05$
$SrZrO_3$	4.17	4.13	4.14	4.14	4.10 [175]	$d_{Sr-O} = 2.95; 2.93$ $d_{Zr-O} = 2.09; 2.07$
$BaZrO_3$	4.24	4.19	4.20	4.20	4.19 [176]	$d_{Ba-O} = 3.00; 2.97$ $d_{Zr-O} = 2.12; 2.10$

with their respective available literature values. This may be due to the fact that these zirconate perovskites do not crystallize in cubic phase but rather in orthorhombic phase below room temperature [177]. Further, the larger size of cation A would have higher lattice constant as there is no effect of charge in the structure due to the same number of valence electrons. Since the DFT simulation is a zero temperature calculation, the cubic structural phase of $AZrO_3$ may not be dynamically stable at 0 K. This can be seen from the phonon dispersion curves and density of states curves, as shown in Figure 4.2 and Figure 4.3 respectively. These phonon spectra are calculated from PHONOPY [178], under harmonic approximation, by considering non-analytical term correction. The phonon calculations are done in a 2x2x2 super-cell, with a sampling mesh of 30x30x30. In the case of PBE functional, density functional perturbation method (DFPT) [179] is implemented whereas for HSE06 functional, finite displacement method (FDM) [180] is used for phonon calculations. It is ensured that the computed dynamical force constant matrix is symmetric. The presence of soft modes and negative (imaginary) frequency at the M and R points at the Brillouin zone in $CaZrO_3$ and $SrZrO_3$ indicates that the cubic structure is not their ground state structures. One can easily notice that the stability increases as the size of cation A increases. More accurately, the orthorhombic form transitions to cubic phase as the cation

size A increases. Only $BaZrO_3$ shows the stable cubic structure at 0 K. Furthermore, it has been experimentally known that there is no phase transition in $BaZrO_3$ between 4 and 1200 K, indicating high stable cubic structure [181]. The negligible forbidden gap between acoustic and optical phonons illustrates that they are good for thermal barrier coating materials.

4.3.2 Elastic Properties

The elastic properties of a crystal can be determined by computing its stiffness tensor $[C_{ij}]$, which is actually the response of a material to external stress. The stiffness matrices $[C_{ij}]_s$ of calcium zirconate, strontium zirconate and barium zirconate perovskites, calculated using PBE and HSE06 functionals are shown below,

(a) $CaZrO_3$

$$\left[C_{ij}\right]_{PBE} = \begin{pmatrix} 326.901 & 71.570 & 71.570 & 0 & 0 & 0 \\ 71.570 & 326.901 & 71.570 & 0 & 0 & 0 \\ 71.570 & 71.570 & 326.901 & 0 & 0 & 0 \\ 0 & 0 & 0 & 63.301 & 0 & 0 \\ 0 & 0 & 0 & 0 & 63.301 & 0 \\ 0 & 0 & 0 & 0 & 0 & 63.301 \end{pmatrix}; \left[C_{ij}\right]_{HSE06} = \begin{pmatrix} 359.921 & 76.418 & 76.418 & 0 & 0 & 0 \\ 76.418 & 359.921 & 76.418 & 0 & 0 & 0 \\ 76.418 & 76.418 & 359.921 & 0 & 0 & 0 \\ 0 & 0 & 0 & 72.559 & 0 & 0 \\ 0 & 0 & 0 & 0 & 72.559 & 0 \\ 0 & 0 & 0 & 0 & 0 & 72.559 \end{pmatrix}$$

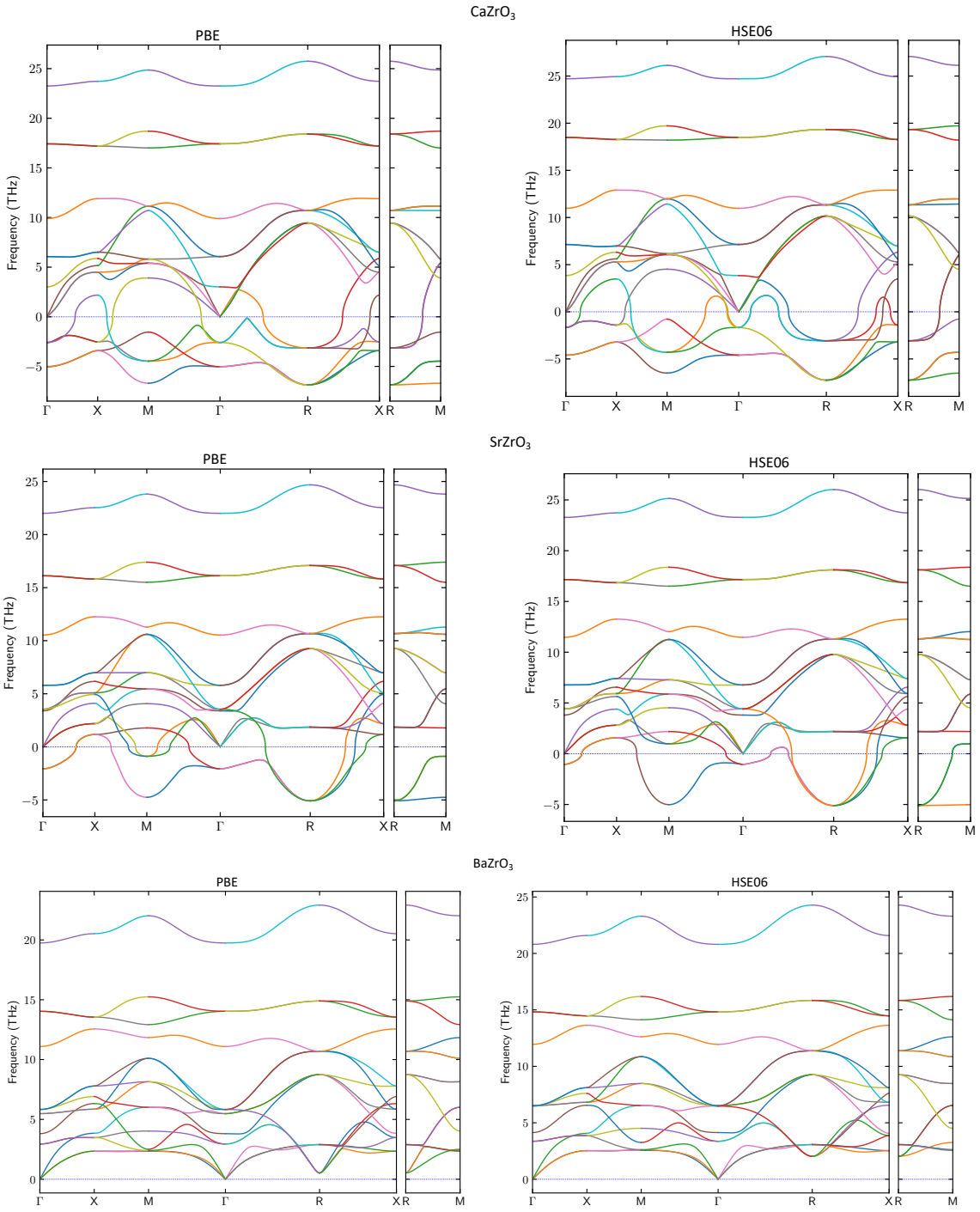

Figure 4.2 Calculated phonon band structure of calcium zirconate, strontium zirconate and barium zirconate perovskites, computed using both PBE and HSE06 functionals.

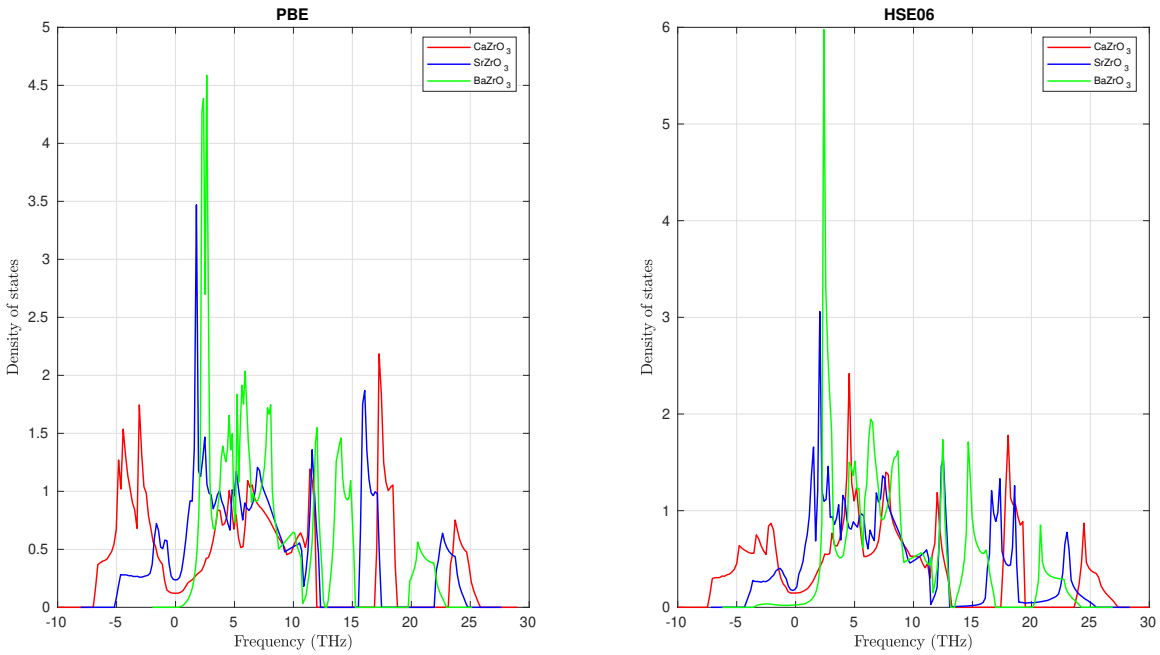

Figure 4.3 Calculated phonon density of states of calcium zirconate, strontium zirconate and barium zirconate perovskites, computed using both PBE and HSE06 functionals.

(b) $SrZrO_3$

$$\left[C_{ij}\right]_{PBE} = \begin{pmatrix} 314.074 & 73.665 & 73.665 & 0 & 0 & 0 \\ 73.665 & 314.074 & 73.665 & 0 & 0 & 0 \\ 73.665 & 73.665 & 314.074 & 0 & 0 & 0 \\ 0 & 0 & 0 & 74.027 & 0 & 0 \\ 0 & 0 & 0 & 0 & 74.027 & 0 \\ 0 & 0 & 0 & 0 & 0 & 74.027 \end{pmatrix}; \left[C_{ij}\right]_{HSE06} = \begin{pmatrix} 347.714 & 81.260 & 81.260 & 0 & 0 & 0 \\ 81.260 & 347.714 & 81.260 & 0 & 0 & 0 \\ 81.260 & 81.260 & 347.714 & 0 & 0 & 0 \\ 0 & 0 & 0 & 83.017 & 0 & 0 \\ 0 & 0 & 0 & 0 & 83.017 & 0 \\ 0 & 0 & 0 & 0 & 0 & 83.017 \end{pmatrix}$$

(c) $BaZrO_3$

$$\left[C_{ij}\right]_{PBE} = \begin{pmatrix} 290.827 & 79.417 & 79.417 & 0 & 0 & 0 \\ 79.417 & 290.827 & 79.417 & 0 & 0 & 0 \\ 79.417 & 79.417 & 290.827 & 0 & 0 & 0 \\ 0 & 0 & 0 & 85.255 & 0 & 0 \\ 0 & 0 & 0 & 0 & 85.255 & 0 \\ 0 & 0 & 0 & 0 & 0 & 85.255 \end{pmatrix}; \left[C_{ij}\right]_{HSE06} = \begin{pmatrix} 322.908 & 86.971 & 86.971 & 0 & 0 & 0 \\ 86.971 & 322.908 & 86.971 & 0 & 0 & 0 \\ 86.971 & 86.971 & 322.908 & 0 & 0 & 0 \\ 0 & 0 & 0 & 96.363 & 0 & 0 \\ 0 & 0 & 0 & 0 & 96.363 & 0 \\ 0 & 0 & 0 & 0 & 0 & 96.363 \end{pmatrix}$$

The inclusion of HF exchange causes an increment in the values of the elements in stiffness tensor. One can notice from the stiffness matrices that, in a cubic system, normal stress only produces normal strain and shear stress only produces shear strain. In contrast with the diagonal elements of the fourth quadrant, the diagonal elements of the first quadrant decrease and off-diagonal elements increase in the order of cation size A, as observed in these zirconate perovskites. This observation implies that the shear modulus/bulk modulus increases/decreases whenever the cation size increases. Using the Voigt-Reuss-Hill (VRH) [182, 183] averaging scheme, the shear modulus G and the bulk modulus B are related to $[C_{ij}]$ as [184],

$$\begin{aligned} G_v &= \frac{C_{11} - C_{12} + 3C_{44}}{5} \\ G_R &= \frac{5C_{44}(C_{11} - C_{12})}{4C_{44} + 3(C_{11} - C_{12})} \\ G &= \frac{1}{2}(G_v + G_R) \end{aligned} \tag{4.1}$$

$$\begin{aligned} B_v = B_R &= \frac{C_{11} + 2C_{12}}{3} \\ B &= \frac{1}{2}(B_v + B_R) \end{aligned} \tag{4.2}$$

We have also calculated Zener anisotropy factor A, Young's modulus E, Poisson's ratio v, Cauchy pressure C, Vickers hardness H_v and Debye temperature Θ_D according to the relations [185–188],

$$A = \frac{2C_{44}}{(C_{11} - C_{12})} \tag{4.3}$$

$$E = \frac{9BG}{3B + G} \tag{4.4}$$

$$v = \frac{3B - 2G}{2(3B + G)} \tag{4.5}$$

$$C = C_{12} - C_{44} \tag{4.6}$$

$$H_v = 2(\frac{G^3}{B^2})^{0.585} - 3 \tag{4.7}$$

$$\Theta_D = \frac{h}{k}(\frac{3nN_A\rho}{4\pi M})^{(1/3)} v_m \tag{4.8}$$

where h, k, N_A and ρ are Planck constant, Boltzmann constant, Avogadro number and density respectively; n and M are number of atoms and molecular mass per formula unit respectively; v_m is the average wave velocity calculated from G and B. They are shown in Table 4.2. The mechanical stability of these zirconate perovskites can be known from the Born's stability criteria [189], i.e., $C_{11} > 0$, $C_{44} > 0$, $C_{11} > |C_{12}|$ and $(C_{11} + 2C_{12}) > 0$. Based on these criteria, the materials under study are mechanically stable. Similarly, the anisotropic factor A being less than unity for all zirconate perovskites conveys that the materials exhibit elastic anisotropy. The brittle/ductile nature of the material can be known from the Pugh criterion B/G and the Poisson's ratio [190]. If B/G exceeds the critical value of 1.75, the material shows ductile nature; otherwise it is brittle. Likewise, the Poisson's ratio v greater than 0.33 indicates the ductile nature of the material; otherwise, it is brittle. Moreover, according to Pettifor criterion [191], the materials develop covalent character and possess brittle nature for negative Cauchy pressure; otherwise, they exhibit metallic character with ductile nature. All these criteria points that strontium zirconate and barium zirconate show brittle nature. Except the Poisson's ratio criterion, the Pugh criterion and the Pettifor criterion indicate that calcium zirconate shows ductile character. The hardness

test is important as it describes the material's ability to resist deformation. The computed Vickers hardness qualitatively conveys that the more brittleness the material, the more is its hardness. The Debye temperature correlates the highest normal mode of vibration. It can be seen from Table 4.2 that the Debye temperature decreases as one goes down the group of alkali-earth metal. This is because the density of an atom increases down the group which in turn decreases the velocity of sound.

4.3.3 Electronic Properties

The electronic band structures for calcium zirconate, strontium zirconate and barium zirconate perovskites, along with their density of states (DOS), are shown in Figures 4.4 and 4.5. It can be seen that HSE06 functional predicts the band gap with better accuracy than PBE functional. The spin-orbit coupling (SOC) shows trivial influence on these band structures. The band gaps due to HSE06 are also calculated using the PBE- generated structures (PBE-g). The severe underestimation of band gap by PBE and PBEsol indicates that these functionals suffer intrinsic self-interaction errors tremendously. On the other hand, the hybrid functional PBE0 tends to overestimate the band gap. Though PBE0 and HSE06 utilize the same portion of the mixing parameter, it shows that the screening factor is responsible for affecting the band gap. One can easily notice that the band gap bears an inverse relation with the screening parameter. Furthermore, these zirconate perovskites contain 4d electrons and besides global exchange correction, the correlation effect does influence the determination of band gap. The correction of correlation errors along with the pre-knowledge of the amount of HF exchange and the screening parameter is therefore crucial for predicting the more accurate electronic structure of zirconate perovskites. All these zirconate perovskites show topological resemblance and possess indirect band gap with transition occurring at $R-\Gamma$ symmetric points. However, the energy eigen values of the valence band are close to each other at M and R symmetric points. The computed band gaps along with their experimental values are shown in Table 4.4. From the analysis of

Table 4.2 Calculated Values of Elastic Constants, Anisotropy Factor, Cauchy Pressure, Vicker's Hardness and Debye Temperature, using Functionals PBE and HSE06, along with Their Available Experimental and Theoretical Values

Materials	*Methods*	G (GPa)	B (GPa)	A	E (GPa)	v	C (GPa)	H_v (GPa)	Θ_D (K)
$CaZrO_3$	*PBE*	84.169	156.681	0.495	214.159	0.272	8.27	9.927	612.964
	*HSE*06	95.200	170.919	0.512	240.878	0.265	3.86	11.493	648.714
	Expt.	-	-	-	-	-	-	-	-
	Theory [160]	87.9	154.8	0.495	221.8	0.261	8.2	11.148	-
$SrZrO_3$	*PBE*	89.983	153.802	0.615	225.894	0.255	−0.362	11.853	564.808
	*HSE*06	100.427	170.078	0.623	251.733	0.253	−1.76	13.011	594.051
	Expt. [192]	-	150	-	-	-	-	-	-
	Theory [156, 162, 193]	102.2, 118.8, 74.84	154.90, 160, 124.76	0.71, 0.58, 0.64	248.62, 247.64, 241.34	0.23, 0.20, 0.25	−15.51, −6, −0.01	15.418, 20.094, 10.519	-
$BaZrO_3$	*PBE*	92.920	149.887	0.806	231.022	0.243	−5.838	13.196	522.858
	*HSE*06	104.493	165.617	0.816	259.007	0.239	−9.392	14.708	551.897
	Expt. [194]	103	127	-	243	0.18	-	4.95	544
	Theory [195]	93	153	0.8	260	0.247	-	12.835	-

orbital contributions to DOS, it has been found that the valence band maxima (VBM) is dominated by O-2p states and the conduction band maxima (CBM) is dominated by Zr-4d states. These states also satisfy the selection rule for transition, that the change in angular momentum is unity, i.e., $\Delta l = \pm 1$. One can notice that the band gap is independent

Table 4.3 The Magnitude of BECs of Calcium Zirconate, Strontium Zirconate and Barium Zirconate Perovskites, Calculated using PBE and HSE06 Functionals

Materials	PBE	HSE06
$CaZrO_3$		
Ca	2.62	2.56
Zr	5.92	5.73
O	$-1.83, -4.89$	$-1.79, -4.69$
$SrZrO_3$		
Sr	2.57	2.54
Zr	6.01	5.78
O	$-1.85, -4.88$	$-1.83, -4.66$
$BaZrO_3$		
Ba	2.72	2.68
Zr	6.12	5.88
O	$-1.99, -4.86$	$-1.96, -4.64$

Table 4.4 Calculated Values of Band Gap (E_g) along with Their Experimental Values and Flow of Charge in Ions, Computed using Functionals PBE and HSE06

	$E_g(eV)$								
Materials	*PBE*	*PBE* (*SOC*)	*PBEsol*	*PBE*0	*HSE*06	*HSE*06 (*PBE*-g)	*Experimental*	*Flow* (*PBE*)	*Flow* (*HSE*06)
$CaZrO_3$	3.30	3.27	3.48	6.67	5.01	4.98	≈ 5.7 [196]	Ca-31.28% O-8.60%; O-144.75% Zr-48.13%	Ca-28.25% O-10.01%; O-134.90% Zr-43.23%
$SrZrO_3$	3.33	3.28	3.56	6.82	4.92	4.90	≈ 5.6 [197]	Sr-28.70% O-7.35%; O-144.10% Zr-50.37%	Sr-27.30% O-2.67%; O-133.12% Zr-44.56%
$BaZrO_3$	3.12	3.08	3.37	6.64	4.69	4.65	5.33 [198]	Ba-36.23% O-0.27%; O-143.16% Zr-53.19%	Ba-34.10% O-1.965%; O-132.30% Zr-47.13%

≈ room-temperature structure

of the order of cation size A. Similarly, in order to know the nature and strength of bonds in these structures, the Born effective charges (BECs) [179, 199] have been calculated and shown in Table 4.3. It is plausible to do so as studies have shown that ionicity defined by charge transfer can be described by the square root of Phillips ionicity [200]. Furthermore,

there are many empirical relationships between effective charge and ionicity [201]. The flow of a charge in an ion with respect to its static charge (SC) arises from the coupling between lattice displacement and electrostatic field and can be quantified as,

$$flow = \frac{|BEC - SC|}{SC} \times 100\% \tag{4.9}$$

They are shown in Table 4.4. The significantly higher flow indicates the covalent character of the bond. One can notice that the oxygen ion has both low and high flow, at directions perpendicular and parallel to the $[Ba{-}O]$ bond respectively, indicating that the low flow makes the ionic bond with the cation A and the high flow makes covalent bond with the cation Zr. The ionic strength in $[Ba{-}O]$ bond is the strongest as the flow of charge in oxygen is lowest among all, indicating that the O atom is the farthest from the Ba atom. This seems convincing from the notion of Fajan's rule [202] that the cation which is nearer to the anion can polarize it maximum, yielding higher degree of covalency. Therefore, the strength of ionic bond follows the order $[Ba-O] > [Sr-O] > [Ca-O]$ and the covalent bond strength as $[Zr-O]_{Ca} > [Zr-O]_{Sr} > [Zr-O]_{Ba}$.

4.3.4 Optical Properties

The electronic response of a material towards an incident photon can be described from its complex dielectric function $\varepsilon(\omega) = \varepsilon_1(\omega) + i\varepsilon_2(\omega)$. Generally, the real part $\varepsilon_1(\omega)$ represents the phase lag between the incident field and induced field due to polarization and the imaginary part $\varepsilon_2(\omega)$ represents the measure of energy loss. The imaginary part $\varepsilon_2(\omega)$ can be evaluated from the momentum matrix elements between

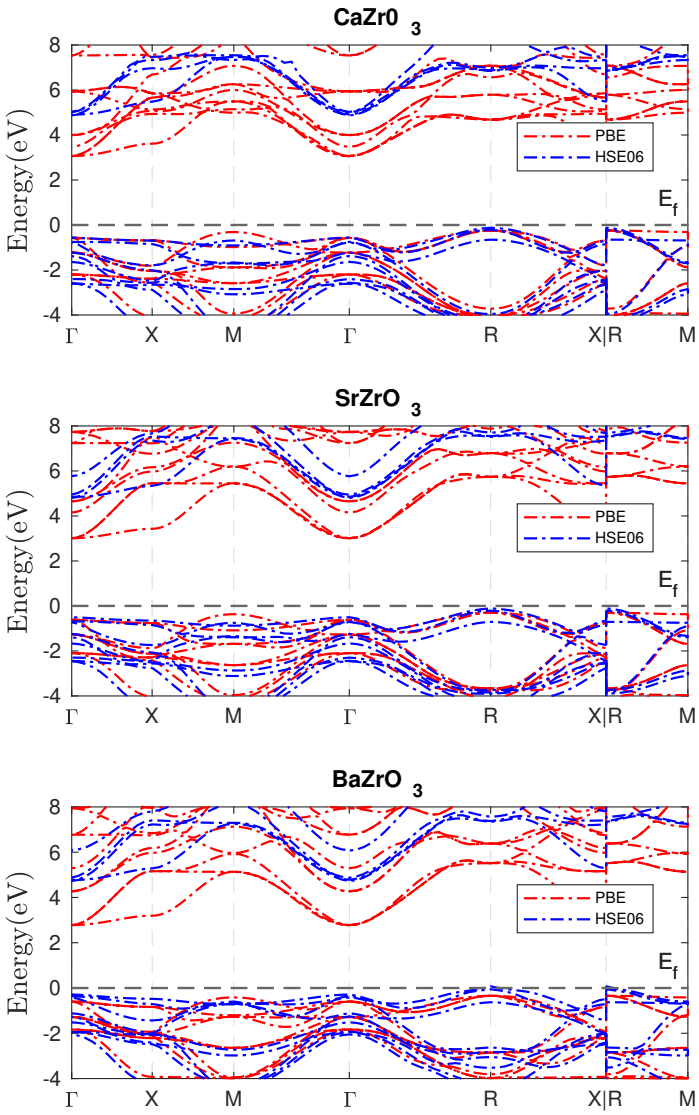

Figure 4.4 The electronic band structures of calcium zirconate, strontium zirconate and barium zirconate perovskites.

the unoccupied and occupied electronic states as [203],

$$\varepsilon_2(\omega) = \frac{Ve^2}{2\pi\hbar m^2\omega^2}\int d^3k \sum_{nn'} |<\overrightarrow{k}\,n|\overrightarrow{p}|\overrightarrow{k}\,n'>|^2 f(\overrightarrow{k}\,n)$$

$$[1-f(\overrightarrow{k}\,n')]\delta[E_{\overrightarrow{k}\,n} - E_{\overrightarrow{k}\,n'} - \hbar\omega]$$

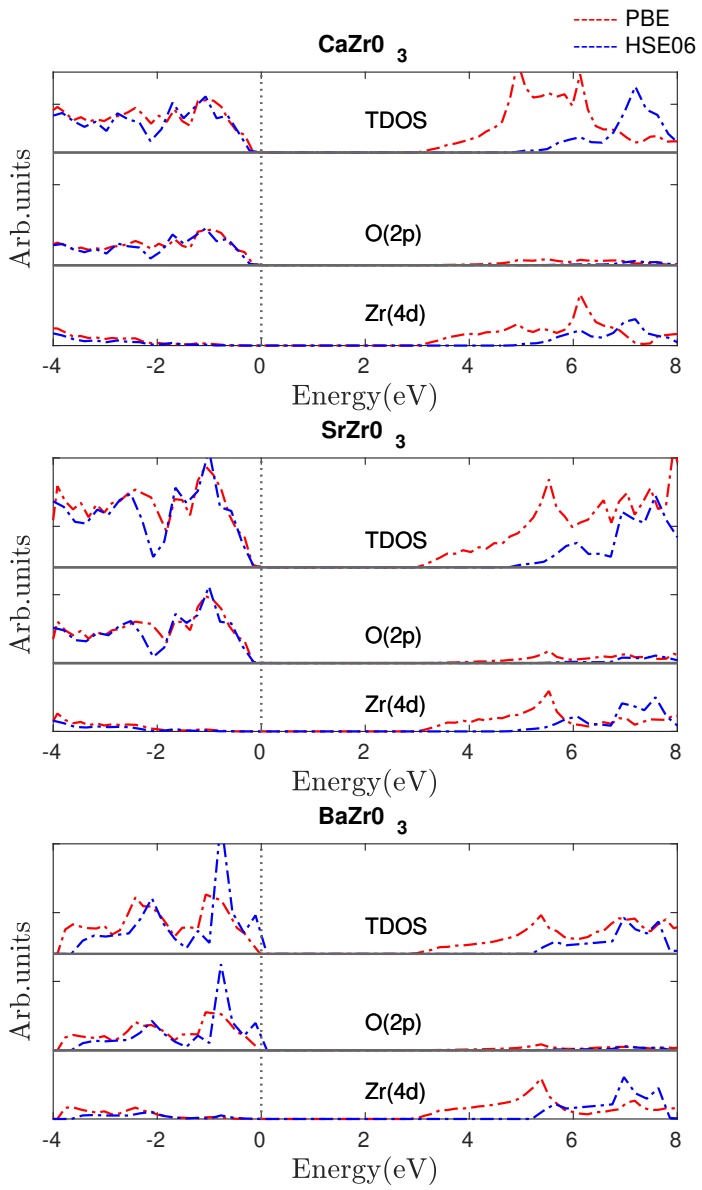

Figure 4.5 The total density of states (TDOS) of calcium zirconate, strontium zirconate and barium zirconate perovskites, along with orbitals contribution of their respective elements.

where, $\overrightarrow{p}$, $f(\overrightarrow{k}n)$, $E_{\overrightarrow{k}n}$ are the momentum operator, Fermi distribution function and eigenvalue of state $\overrightarrow{k}n$ respectively. The real part $\varepsilon_1(\omega)$ can then be evaluated from the imaginary part $\varepsilon_2(\omega)$ using the Kramers-Kronig relation as [204],

$$\varepsilon_1(\omega) = 1 + \frac{2}{\pi}\int_0^{\infty} \frac{\omega'\varepsilon_2(\omega')}{\omega'^2 - \omega^2} d\omega' \tag{4.10}$$

The calculated $\varepsilon_1(\omega)$ and $\varepsilon_2(\omega)$ for calcium, strontium and barium zirconate perovskites using both PBE and HSE06 functionals are shown in Figure 4.6. Both PBE and

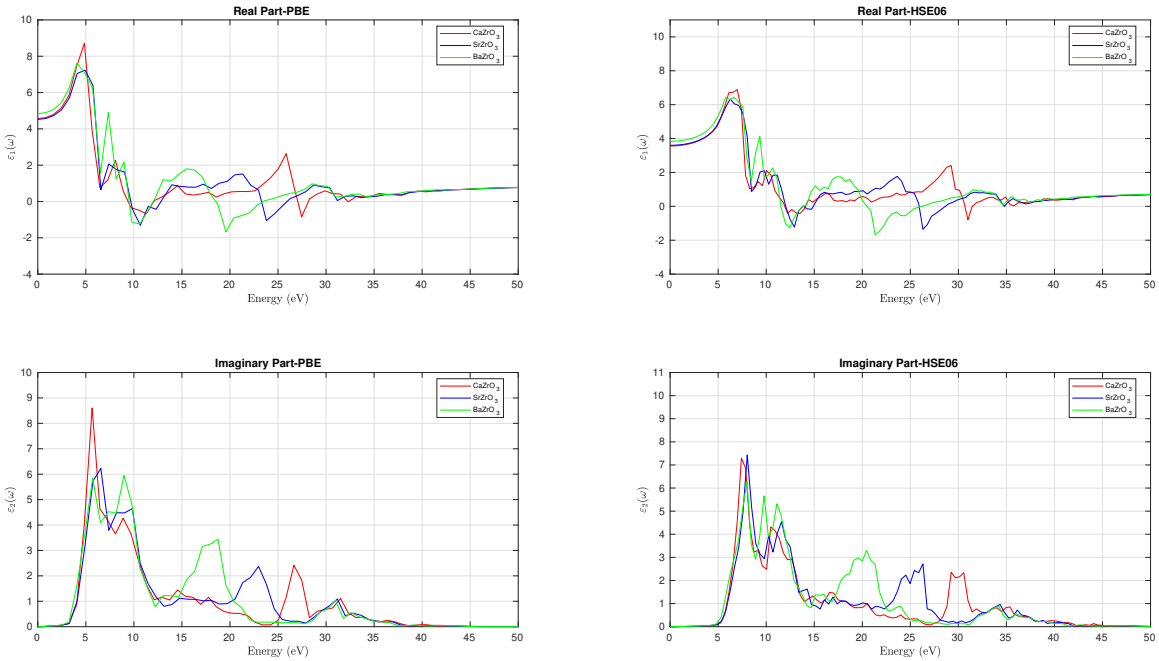

Figure 4.6 Real and imaginary parts of dielectric function of calcium zirconate, strontium zirconate and barium zirconate perovskites, computed using functionals PBE and HSE06.

HSE06 computations show similar dielectric spectra and any variation can be attributed to the effect of short range electron-electron interaction. For the time dependent field, $\varepsilon_1(0)$ is the static dielectric constant. It is noteworthy that the variation of static dielectric constant is independent of the size of ion A and shows inverse relation to band gap as suggested by Penn model [90] as,

$$\varepsilon_1(0) \approx 1 + [\frac{\hbar\omega_p}{E_g}]^2 S_0 \tag{4.11}$$

where, S_0 is a dimensionless constant, ω_p is a screened plasma frequency and E_g is a Penn gap. Usually, the Penn gap is larger than a band gap, and refers to energy corresponding to the first reflectivity peak. The value of S_0, as suggested by Penn himself, is 1 and the more accurate value, especially for homopolar semiconductors, is taken as 0.62 [91].

Recent study by Diego Julio Cirilo-Lombardo [205] has suggested the value to be $2/3$. Our work on zirconate perovskites suggest the value to be 0.86. Table 4.5 shows the values of $\varepsilon_1(0)$, plasmon energy $\hbar\omega_p$, Penn gap E_g and reflectivity peak E_R. On the other hand, $\varepsilon_2(\omega)$ is seldom negative and starts from zero and shows variation after the incident photon energy exceeds the threshold band width. The peaks of $\varepsilon_2(\omega)$ are related to the interband transitions. From the knowledge of $\varepsilon_1(\omega)$ and $\varepsilon_2(\omega)$, the other optical properties

Table 4.5 Calculated Values of $\varepsilon_1(0)$, $\hbar\omega_p$, E_g(Penn) and E_R

Materials	*Methods*	$\varepsilon_1(0)$	$\hbar\omega_p$ (eV)	$E_g(Penn)$ (eV) $S_0 = 2/3, 1$	E_R (eV)
$CaZrO_3$	*PBE*	4.56	11.88	5.14, 6.29	5.65
$CaZrO_3$	*HSE*06	3.56	14.22	7.34, 8.88	8.02
$SrZrO_3$	*PBE*	4.52	12.76	5.55, 6.80	6.50
$SrZrO_3$	*HSE*06	3.59	13.85	7.02, 8.60	8.01
$BaZrO_3$	*PBE*	4.83	12.10	5.04, 6.18	5.70
$BaZrO_3$	*HSE*06	3.84	13.91	6.74, 8.25	7.89

such as reflectivity R, refractive index n, extinction coefficient k, energy loss spectra L and absorption coefficient α are calculated as [206–208],

$$R(\omega) = \frac{(n-1)^2 + (\frac{\alpha c}{2\omega})^2}{(n+1)^2 + (\frac{\alpha c}{2\omega})^2} \tag{4.12}$$

where c is the speed of light.

$$n(\omega) = [\frac{\{\varepsilon_1^2(\omega) + \varepsilon_2^2(\omega)\}^{1/2} + \varepsilon_1(\omega)}{2}]^{1/2} \tag{4.13}$$

$$k(\omega) = [\frac{\{\varepsilon_1^2(\omega) + \varepsilon_2^2(\omega)\}^{1/2} - \varepsilon_1(\omega)}{2}]^{1/2} \tag{4.14}$$

$$L(\omega) = \frac{\varepsilon_2(\omega)}{[\varepsilon_1^2(\omega) + \varepsilon_2^2(\omega)]} \tag{4.15}$$

$$\alpha(\omega) = \frac{2\omega}{c}\left[\frac{\{\varepsilon_1^2(\omega) + \varepsilon_2^2(\omega)\}^{1/2} - \varepsilon_1(\omega)}{2}\right]^{1/2} \tag{4.16}$$

They are shown in Figure 4.7. One can notice that not only $\varepsilon_1(0)$ but also $R(0)$ and $n(0)$

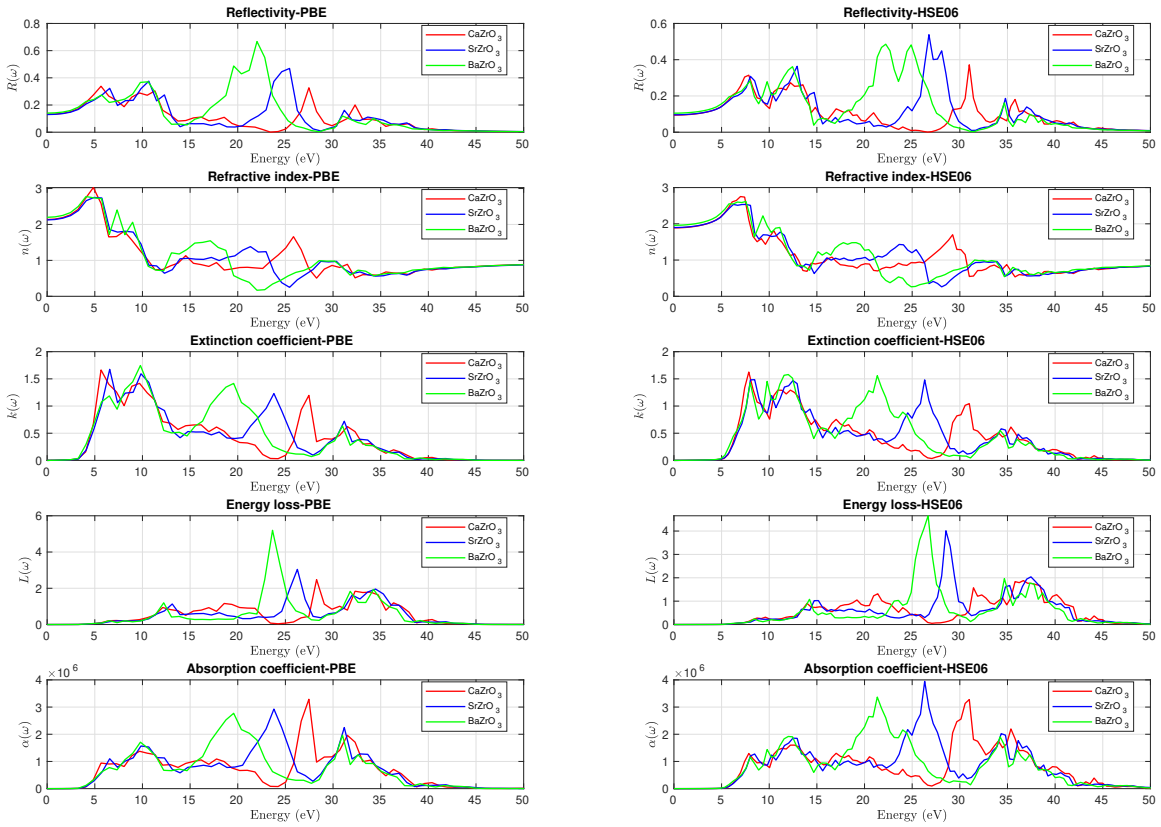

Figure 4.7 Reflectivity, refractive index, extinction coefficient, energy loss and absorption coefficient spectra.

are independent of the size of cation A. The values of $R(0)$ and $n(0)$ indicate that $BaZrO_3$ shows higher metallic character for the time-independent field. The reflectivity spectra $R(\omega)$ of all zirconate perovskites show minima at energies corresponding to the plasma edge. This decrease in reflectivity may be due to plasmonic excitation. Furthermore, our calculated static refractive index satisfies the relation $n(0) = (\varepsilon(0))^{1/2}$ and its inverse

Table 4.6 Calculated Values of Static Reflectivity and Refractive Index

Materials	*Methods*	$R(0)$	$n(0)$	$n(H-V)$
$CaZrO_3$	*PBE*	0.13	2.14	≈ 1.80
$CaZrO_3$	*HSE*06	0.09	1.88	
$SrZrO_3$	*PBE*	0.13	2.13	≈ 1.78
$SrZrO_3$	*HSE*06	0.09	1.89	
$BaZrO_3$	*PBE*	0.14	2.20	1.84
$BaZrO_3$	*HSE*06	0.11	1.95	

dependence with band gap can be verified from Harve-Vandamme $(H-V)$ relation [96],

$$n(H-V) = \sqrt{1+(\frac{A}{E_g+B})^2} \tag{4.17}$$

where A=13.6 eV and B=3.4 eV are the constants. Utilizing $H-V$ relation, the refractive indices are calculated with the aid of their experimental band gaps and then compared with the simulated values. They are shown in Table 4.6. The peak of energy loss spectra $L(\omega)$ characterizes the plasma resonance. The absorption coefficient α is almost zero when the photon energy is below band gap, which is trivial for single particle model. At energy higher than plasmon energy, the absorption coefficient decreases to zero and refractive index approaches one, indicating the transparency of the material. All these materials show high absorption in the UV region.

4.4 Conclusions

In summary, a comprehensive study of the cubic phase of $CaZrO_3$, $SrZrO_3$ and $BaZrO_3$ was performed using both PBE and HSE06 functionals. It was found that the lattice constants of these zirconate perovskites are dependent on the size of their respective alkaline-earth metal cations. Moreover, except $BaZrO_3$, the cubic phases of $CaZrO_3$ and $SrZrO_3$ are high temperature structures. The study of mechanical properties reveals that

$SrZrO_3$ and $BaZrO_3$ show brittle nature whereas $CaZrO_3$ shows some ductile character. All these materials show high indirect band gap with $A-X$ dominated by ionic bond and $B-X$ by covalent bond. The optical absorption of these zirconate perovskites are higher in the UV regions. Finally, it is anticipated that this study will be helpful to tune the properties of these materials by altering the cation A.

CHAPTER 5

DENSITY FUNCTIONAL STUDY OF Cs-Pb-Br VARIANTS

This chapter is based on the study of Cs-Pb-Br variants. The variants include $CsPbBr_3$, $CsPb_2Br_5$ and Cs_2PbBr_4. The results of this study are presented in TMS conference 2021.

5.1 Introduction

Perovskite solar cells have gained notoriety in the last few years as their light-harvesting capacity has been augmented from 3.8% in 2009 to over 24.2% in 2019 [209]. Despite the demonstration of increasing efficiency of perovskite solar cells in a short time, there are several issues such as fabrication processes, stability, degradation, predictability in behavior, durability, toxicity etc., that has hindered their use in the commercial realm [210–212]. Methylammonium lead halide has been extensively studied from the very beginning due to its potential as a perovskite solar cell material [26, 213]. However, this material deteriorates rapidly when exposed to light, heat, air or moisture [214, 215]. As an alternative to methylammonium lead halide, it has been found that lead-based and tin-based inorganic halide perovskites show better stability under external conditions and qualify as suitable materials for solar cells and other optoelectronic devices [216–219]. From the environmental perspective, tin-based perovskites are considered as a better choice than lead-based perovskites [220]. Nevertheless, the efficiency and stability of tin-based perovskites is inferior. Furthermore, it has been found that lead-based perovskite solar cells pose a minor environmental hazard [221–224]. Among several inorganic halide perovskites, cesium lead bromide $CsPbBr_3$ shows promise as a candidate for the fabrication of solar cells and optoelectronic devices due to its stability, inherent direct band gap, broad absorption spectrum and good transport properties [225–227]. In recent years, it has been found that lowering the dimensionality of halide perovskites leads to enhanced photoluminescence and stability than their three-dimensional counterparts [228–231].

Further, the change in the dimensionality of an inorganic halide perovskite can evoke surprising ramifications to its intrinsic behavior. The dimensionality in perovskites are governed by their octahedral cages. In zero-dimensional perovskites, the octahedral cages are discrete whereas they are connected with one another forming a layer in two-dimensional perovskites. Likewise, in three-dimensional perovskites, the octahedral cages share the corner atoms with each other. Generally, 2D perovskites are synthesized by inserting some suitable chemical that sits in the intercalated region and acts as a spacer between the layered structure. This technique is profound in 2D organic-inorganic hybrid perovskites. Moreover, the variation of such a spacer not only produces the desired stability to the structure but also yields different functionalities of significant interest to the required 2D system. This is illustrated in Figure 1.2.

This study describes the two-dimensional (2D) counterpart of $CsPbBr_3$. One plausible model for 2D-$CsPbBr_3$ would be Ruddlesden-Popper (RP) phase [232]- Cs_2PbBr_4. Unfortunately, the RP phase is not so frequent in halide perovskites in contrast to oxide perovskites [233]. Nevertheless, it is of interest to proceed with the theoretical study of RP phase of $CsPbBr_3$. On the other hand, the most likely second model for 2D counterpart of $CsPbBr_3$ would be ternary halogen-plumbate $CsPb_2Br_5$. In contrast to Cs_2PbBr_4, $CsPb_2Br_5$ can be synthesized at room temperature, different from $CsPbBr_3$ which requires a higher temperature. The first report on the synthesis of $CsPb_2Br_5$ was probably mentioned by Yu et al. [234] stating its efficient photoluminescence in the visible region (512 nm) with a quantum yield of 87%. In the paper of Sun et al. [235], they have reported that $CsPb_2Br_5$ results as a by-product during the synthesis of $CsPbBr_3$, yielding higher photoluminescence by transitioning to $CsPb_2Br_5$. However, the work of Jiang et al. [236] has some contradiction by reporting $CsPb_2Br_5$ as an indirect band gap material with inactive photoluminescence. Further, Zhang et al. [237], in their paper, have clarified from the luminescence mechanism that $CsPb_2Br_5$ exhibits a band-edge emission

in the ultraviolet region and photoluminscence is associated with $CsPbBr_3$ by-product in $CsPb_2Br_5$.

The need for a theoretical study of Cs-Pb-Br variants is significant due to the complexity in the synthesis and characterization of these materials. The aim of this paper is to study the structural, electronic and optical properties of 3D-$CsPbBr_3$ in conjunction with its 2D counterparts- both RP phase Cs_2PbBr_4 and $CsPb_2Br_5$; utilizing the framework of density functional theory (DFT). The emergence of new physical phenomena with respect to the decreasing dimensionality of $CsPbBr_3$ are analyzed. It is anticipated that this work will be beneficial in the design and fabrication of solar cells and other potential optoelectronic devices.

5.2 Computational Details

This work utilizes first-principles calculations based on DFT in which projector augmented wave (PAW) method was implemented using the Vienna Ab initio Simulation Package (VASP) [29, 30]. All the calculations were performed within the Generalized Gradient Approximation (GGA) using Perdew, Burke and Ernzerhof (PBE) as exchange-correlation functional [159, 238]. The plane wave basis functions with large cut off energy- 400 eV (greater than 1.3 times the maximum cut off energy) were used in all the three variants of *Cs-Pb-Br* along with a sufficiently large Monkhorst K-mesh for Brillouin Zone integration. The lattice optimizations were performed with total energy convergence criteria of 10^{-6} eV and final force acting on each atom smaller than 0.02 eV/$\mathring{A}$. The resultant optimized structures, along with the lattice parameters, are summarized in Table 1. For post processing, simulation tools such as Vesta [239], Vaspkit [240], Phonopy [178] and Sumo [241] are used in this study.

Table 5.1 Calculated Structure of Unit Cell Geometry with Lattice Parameters (a, b, c) along with Their Corresponding Literature Values in Angstrom

Material	Crystal system	Space group	Unit cell dimensions	Others work Experimental (Theoretical)
$CsPbBr_3$	Orthorhombic	Pnma (62)	$a = 8.34$, $b = 8.40$ $c = 11.97$	$a = 8.21$,$b = 8.25$ $c = 11.76$ [242]
Cs_2PbBr_4	Tetragonal	I4/mmm (139)	$a = b = 5.97$ $c = 18.33$	$(a = b = 5.95$ $c = 18.19)$ [243]
$CsPb_2Br_5$	Tetragonal	I4/mcm (140)	$a = b = 8.61$ $c = 15.47$	$a = b = 8.49$ $c = 15.19$ [244]

5.3 Results and Discussion

5.3.1 Structure and Stability

The computed structure of $CsPbBr_3$ crystallizes in the orthogonal space group of Pnma (62) and its 2D counterpart Cs_2PbBr_4 and $CsPb_2Br_5$ in the tetragonal space group of I4/mmm (139) and I4/mcm (140) respectively. Their structures are shown in Figure 5.1. $CsPbBr_3$ has interconnected or corner-sharing octahedron cage $[BX_6]^{-1}$ and Cs^+ reside at the centre formed by eight such octahedral cages whereas they are disjoint in Cs_2PbBr_4. Similarly, the structure of $CsPb_2Br_5$ reveals that Cs^+ reside in the intercalated region of $[Pb_2Br_5]^-$ layers.

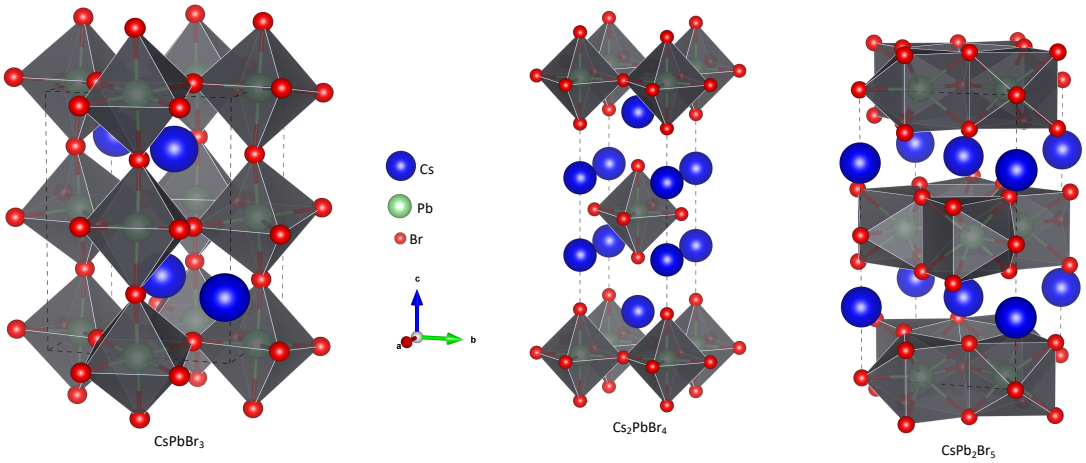

Figure 5.1 Structure of 3*D* and 2*D* variants of Cs-Pb-Br.

Further, the stability of these molecules can be verified by calculating their cohesive energy. The cohesive energy per atom (ΔE_c) for any molecule, say $A_aB_bX_x$, is quantified through the relation,

$$\Delta E_c(A_aB_bX_x) = \frac{aE(A)+bE(B)+xE(X)-E(A_aB_bX_x)}{a+b+x} \tag{5.1}$$

where, $E(i)$, $i = A,B,X$ is the energy of an isolated atom i and $E(A_aB_bX_x)$ represents the total energy of $A_aB_bX_x$. The calculated values of cohesive energy per atom in eV for $CsPbBr_3$, Cs_2PbBr_4 and $CsPb_2Br_5$ are 2.89, 2.87 and 2.88 respectively. Therefore, it appears easy to dissociate Cs_2PbBr_4 among the three compounds of *Cs-Pb-Br*. Moreover, the orthorhombic phase is possibly the ground-state structure of $CsPbBr_3$ and tetragonal phases of their 2D counterparts are unstable at 0 K temperature. This can be seen by the presence of soft modes in their phonon dispersion diagram, as illustrated in Figure 5.2. It has been reported that the stability can be affected by temperature as well as with the number of layers, in the case of 2D [245,246]. Henceforth, one has enough room to suspect that these tetragonal structures might be stable at room temperature or higher, unless they have low phase transition temperature.

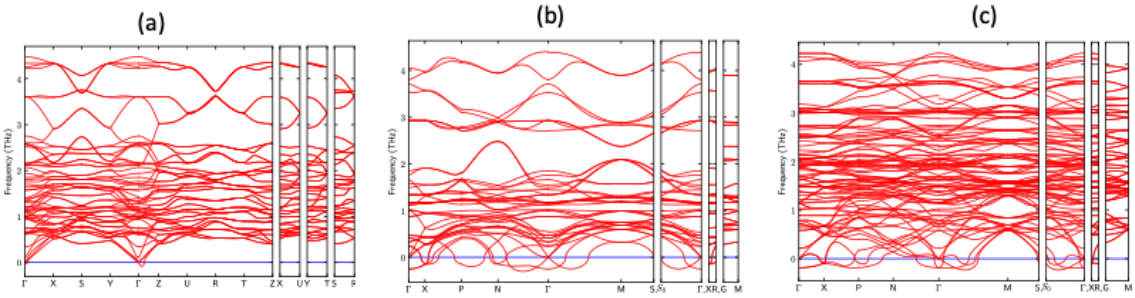

Figure 5.2 Phonon dispersion diagram-(a) $CsPbBr_3$, (b) Cs_2PbBr_4 and (c) $CsPb_2Br_5$ under harmonic approximation.

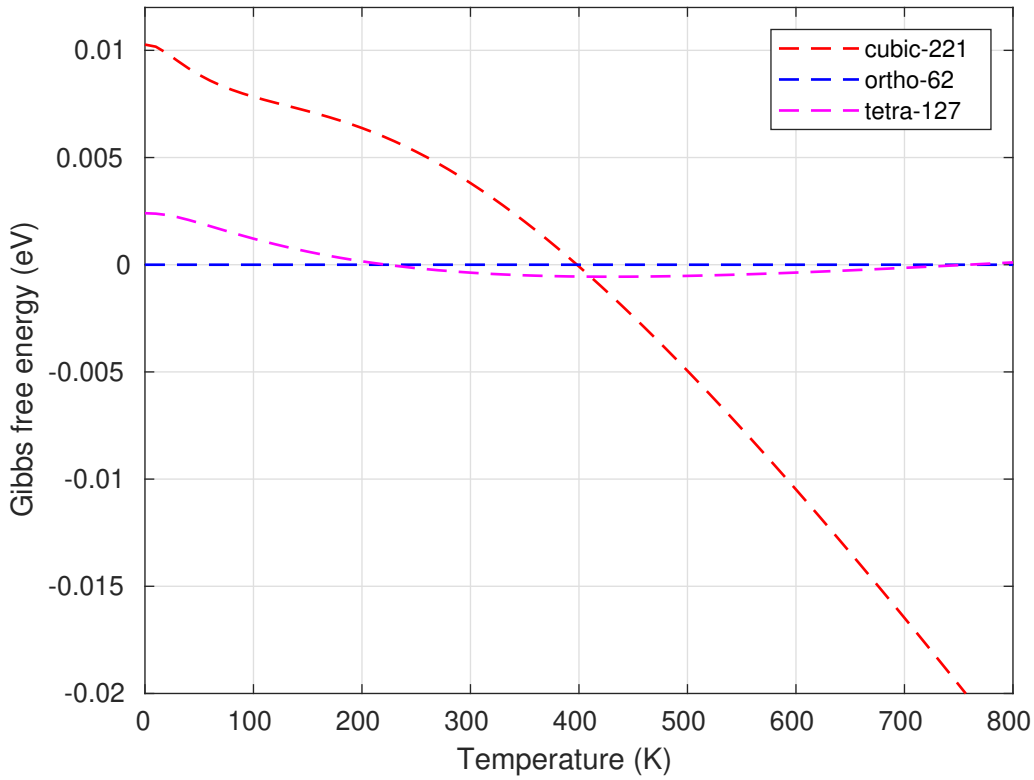

Figure 5.3 The variation of Gibbs free energy of $CsPbBr_3$ phases with temperature, compared with respect to its orthorhombic phase.

It can be seen that *Cs* cation in $APbBr_3$ does not form a modular structure. Its phase evolution with respect to temperature shows that $CsPbBr_3$ has an orthorhombic (space group 62) structure till 200 K and morphs to tetragonal (space group 127) between 200-400 K and cubic (space group 221) above 400 K. This has been predicted by studying the variation of Gibbs free energy using the QHA model, as shown in Figure 5.3. Further, it illustrates that the transition from orthorhombic to tetragonal is second order and from tetragonal to cubic, it is first order. The results agree with experiment [247] which states that the first order and the second order transition occurs at 130 ° *C* and 88 °*C*, respectively.

5.3.2 Electronic Properties

For simulating their electronic properties, we have computed the band structures, the total density of states (DOS) and partial density of states (PDOS); these are shown in Figure 5.4.

One can notice that except $CsPb_2Br_5$, the other variants show direct band gap. Due to heavy atom Pb, the spin-orbit coupling (SOC) is included in all our calculations. In all three variants of *Cs-Pb-Br*, there is no significant change in the topography of the valence band with the inclusion of SOC. However, to demonstrate the conduction band degeneracy

Table 5.2 Calculated Values of Band Gap (E_g) with SOC and WSOC along with Their Corresponding Literature Values in Electron Volt

Material	E_g $SOC;WSOC$	Experimental;Theoretical
$CsPbBr_3$	0.95;2.0	2.25 [248];2.16 [249]
Cs_2PbBr_4	0.98;2.26	−;2.29 [250]
$CsPb_2Br_5$	2.55;3.04	3.87 [251];3.08 [249]

or split due to SOC, an illustration has been shown for $CsPb_2Br_5$. The calculated values of the band gap with SOC and without SOC, along with their literature values, are shown in Table 5.2. It is well known that DFT calculations, using standard functional, severely underestimate the band gap and due to the intrinsic error cancellation between SOC and neglect of quasi-particle corrections, the band gap computed without SOC has higher proximity to the correct value. Further, the orbital contribution of the valence band maximum (VBM) and the conduction band minimum (CBM) can be analyzed from their DOS and PDOS. In all three variants, the VBM is dominated by Br p state and the CBM mainly constitute Pb p state. It is interesting to note that Cs has no direct contribution to the band edge state.

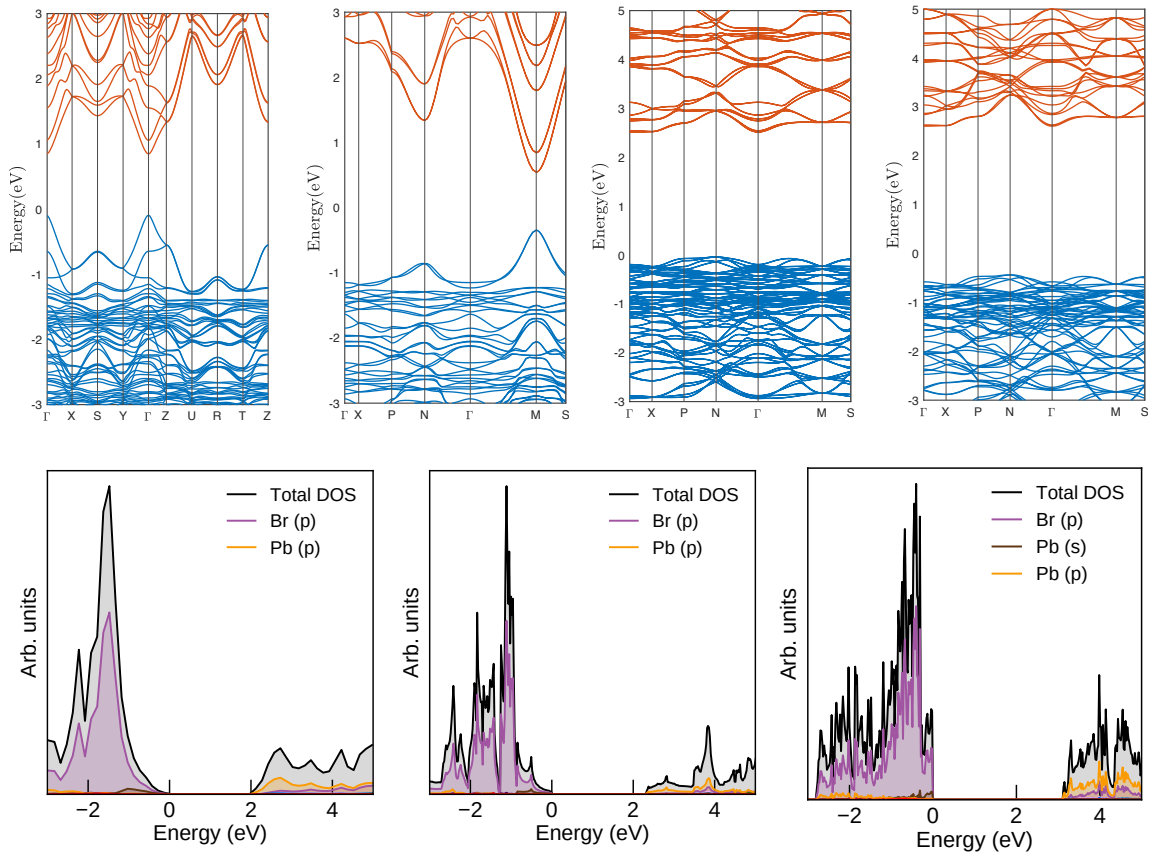

Figure 5.4 Calculated band structure diagrams with SOC, from left to right- $CsPbBr_3$, Cs_2PbBr_4, $CsPb_2Br_5$ with SOC and WSOC (Without SOC) respectively. Their corresponding DOS and PDOS are shown at bottom.

The absorption of photons in halide pervoskite solar cells leads to the generation of electrons and holes. These charge carriers are coupled with each other via Coulomb interaction to form quasiparticles in the form of excitons. The effective mass (m^*) is estimated by the parabolic fitting of energy (E) with momentum (k),

$$m^* = \hbar^2 [\frac{\partial^2 E}{\partial k^2}]^{-1} \tag{5.2}$$

and the exciton binding energy (E_b) is calculated by utilizing the Wannier exciton model [252],

$$E_b = \frac{2\mu e^4}{(\hbar 8\pi\varepsilon(\infty))^2} \tag{5.3}$$

where, μ and $\hbar$ are the reduced effective mass and Planck constant respectively, e is the electronic charge and $\varepsilon(\infty)$ is the permittivity at high wavelength limit. In the case of $CsPbBr_3$, the computed values of m_e^* and m_h^*, under the effect of SOC, are 0.157 m_e and 0.124 m_e respectively and E_b is 51.72 meV. The literature values of m_e^*/m_h^* are slightly greater/less than 0.2 m_e, indicating $m_h^* < m_e^*$ [253]. The calculated values of exciton binding energy for $CsPbBr_3$ are in the range of 27-63 meV [254]. Likewise, the values of m_e^*, m_h^* and E_b for Cs_2PbBr_4 are 0.17 m_e, 0.19 m_e and 102.5 meV respectively. The values of m_e and m_h for Cs_2PbBr_4 are 0.194 m_e and 0.316 m_e respectively [250]. Similarly, for $CsPb_2Br_5$, the values of m_e^*, m_h^* and E_b are 0.52 m_e, 2.41 m_e and 292.30 meV respectively. The large exciton binding energy in 2D counterparts of $CsPbBr_3$ can be attributed to weak screening of Coulomb interaction. It should be noted that the high value of m_h^* can be justified by the flat valence band, as shown in Figures 5.4(c) and 5.4(d). The relative permittivity values, used in the calculations for $CsPbBr_3$, Cs_2PbBr_4 and $CsPb_2Br_5$, are 4.29, 3.45 and 4.47 respectively. These values are the geometric mean of their respective anisotropic values.

5.3.3 Optical Properties

For investigating the optical properties, the absorption coefficient spectra have been studied for all the three variants of *Cs-Pb-Br*. The absorption spectra of materials are of paramount significance as the first and foremost criterion for solar cells should exhibit very high values of the absorption coefficient in the visible range of the solar spectra. Secondly, they play a major role in determining the thickness of cells and therefore in influencing the aspects of cell design. For instance, materials having a higher absorption coefficient are not only suitable for solar cells but also comparatively thin cells can be designed. The absorption coefficient of materials depend on the incident frequency of light and the required variation in materials $CsPbBr_3$, Cs_2PbBr_4 and $CsPb_2Br_5$ are shown in Figure 5.5.

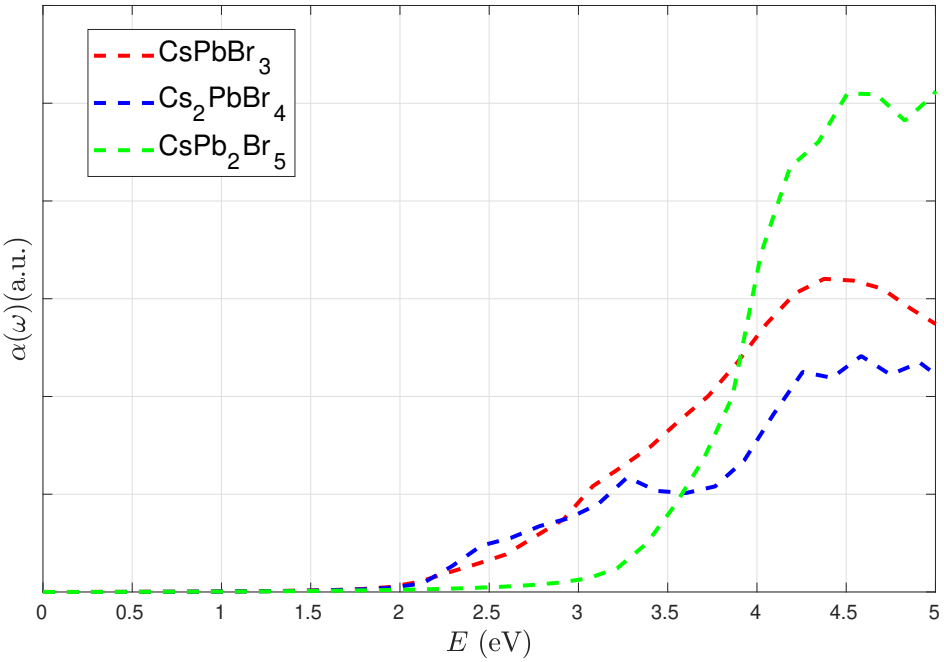

Figure 5.5 Calculated absorption coefficients of Cs-Pb-Br variants in 100 direction. $CsPbBr_3$ is anisotropic in all direction whereas its 2D counterparts- Cs_2PbBr_4 and $CsPb_2Br_5$ is isotropic in 100 and 010 direction.

The absorption coefficients were calculated from frequency (ω) dependent dielectric functions, $\varepsilon(\omega) = \varepsilon 1(\omega) + i\varepsilon 2(\omega)$ according to the relation [206],

$$\alpha(\omega) = \frac{2\omega}{c}\left[\frac{(\varepsilon_1^2(\omega) + \varepsilon_2^2(\omega))^{\frac{1}{2}} - \varepsilon_1(\omega)}{2}\right]^{\frac{1}{2}}, \tag{5.4}$$

The absorption edge values found in the literature for $CsPbBr_3$ and $CsPb_2Br_5$ were 2.4 eV [254] and 3.26 eV [255] respectively, which indeed agree well with our computed values. It can be seen that there is no absorption below the band edge of these materials. $CsPbBr_3$ and Cs_2PbBr_4 show broad absorption ranging from visible to UV region whereas $CsPb_2Br_5$ shows absorption prominent in the UV region. Therefore, $CsPbBr_3$ and Cs_2PbBr_4 materials are more suitable for photovoltaic applications.

5.3.4 Conclusions

In summary, we have studied the structural, electronic and optical properties of $CsPbBr_3$ along with its 2D variants-Cs_2PbBr_4, $CsPb_2Br_5$. There is no significant difference in the cohesive energy of these compounds. All of them show anisotropy and their band structures show noticeable variation in the conduction band region, due to spin-orbit coupling. Except $CsPb_2Br_5$, the other two variants possess intrinsic direct band gap. The optical properties reveal that $CsPbBr_3$ and Cs_2PbBr_4 have absorption edge in the wavelength range of visible to low UV, while $CsPb_2Br_5$ shows dominant absorption in the UV region. The calculations show that the excitons are loosely bound in $CsPbBr_3$ than its 2D counterparts.

CHAPTER 6

ISOSYMMETRIC STRESS ON CUBIC HALIDE PEROVSKITES

This chapter discusses the isosymmetric stress and its application to some cubic halide perovskites. All the calculations are performed with generalized gradient approximation schemes. The study has been published in SN Applied Sciences and can be found at "https://link.springer.com/article/10.1007/s42452-020-04059-1".

6.1 Introduction

Halide perovskites, ABX_3 (A is a monovalent cation, B is a bivalent cation and X is a halogen are found to be important ternary materials for potential use in optoelectronic and photovoltaic applications due to their efficient light-harvesting capabilities [256–259]. Their inherent direct band gap, which resemble the solar spectrum qualify them as excellent solar cell materials [59, 60]. Recent studies of halide perovskites have reported the power conversion efficiency above 25% for perovskite-based solar cells [60].

Despite the tunable band gap, large absorption coefficient in the visible spectrum with long charge carrier diffusion length, small exciton binding energy, defect resistance enabling non-radiative recombination and low-cost fabrication process for perovskite solar cells than conventional cells, they show instability with even minor external conditions and thereby degrade swiftly, decreasing the power conversion efficiency [27, 59, 260–266]. A number of measures have been taken by various researchers not only to make them stable but also tune the band gap at the same time [267–269]. Among several measures, the application of pressure is considered to be one of the clean and green ways to nullify such problems. Furthermore, the investigation of the influence of the reorganization on the lattice structure and its implications on the electronic structure of perovskites can be understood by applying pressure at different scales.

The application of pressure on perovskites can cause several effects such as dilation

of the lattice [270], displacement of cation and anion [271, 272], rotation of octahedral cages [273], phase transitions [274, 275] etc. Generally, more than one effect can occur in perovskites at a time, leading to the dependence of the electronic structure calculations on a number of factors. It is, therefore, critical to study the effect of each factor individually by isolating other effects. Such a study will be beneficial in identifying one-to-one understanding of the dynamics of electronic structure configuration and the properties that are associated with it.

A number of papers on perovskites in the literature discuss the effects of lattice dilation and octahedral rotations [276–278]. The significance of the present study is that it focuses only on the lattice dilation, keeping octahedral rotations unchanged, in the aftermath of the hydrostatic pressure. For this purpose, we have chosen to study the influence of hydrostatic pressure on halide perovskites to investigate how the lattice dilation would affect the electronic structure and the associated properties without any rotation of the polyhedra or phase transitions. Such an application of pressure here on is called isosymmetric compression and the choice of materials that are used to study the isosymmetric lattice contraction are cubic (space group Pm3m) ABX_3 where $A = K, Rb, Cs$; $B = Ge, Sn, Pb$ and $X = Cl, Br, I$. The chosen halide perovskites are taken in such a way that their respective cation and anion belong to the same group (A=alkali metal, B=crystallogen and C=halogen). This way of selecting the perovskites is advantageous as it not only facilitates the study of size effect but also hinders the charge effect as one moves down the periodic table.

The stability and degree of distortion in perovskites are usually quantified by the Goldschmidt tolerance factor (t) [17],

$$t = \frac{R_A + R_X}{\sqrt{2}(R_B + R_X)} \tag{6.1}$$

where, R_A, R_B and R_X are the radii of A, B and X respectively and the measured octahedral tilt angle. In the case of isosymmetric compression, it is easy to note that the tolerance factor for all cubic distorted structure, under compression, should be constant close to unity and exhibits no octahedral tilt or $a^0a^0a^0$ in terms of Glazer notation [22].

In this paper, the various aspects of isosymmetric effects have been discussed. We have investigated the structural, mechanical and electro-optical properties of halide perovskites under isosymmetric lattice contraction. Further, the size effects due to cation and anion substitution have been explored in detail. It is anticipated that the results of this study will be beneficial to design future materials.

6.2 Computational Methods

The first principles calculations based on Density Functional Theory (DFT) have been implemented using the Vienna Ab initio Simulation Package (VASP) [29, 30]. The calculations were performed within the Generalized Gradient Approximation (GGA) using Perdew, Burke and Ernzerhof (PBE) [159, 238, 279] as exchange-correlation functional. This approach considers the valence states $3s^23p^64s^1$ for K, $4s^24p^65s^1$ for Rb, $5s^25p^66s^1$ for Cs, $3d^{10}4s^14p^2$ for Ge, $5s^25p^2$ for Sn, $5d^{10}6s^26p^2$ for Pb, $3s^23p^5$ for Cl, $4s^24p^5$ for Br and $5s^25p^5$ for I. All the lattice optimization for cubic structures were performed with a convergence criterion that the final force acting on each atom should not exceed 0.015 $eV/\AA$. A large Monkhorst K-mesh with spacing of 0.06 $\AA^{-1}$ and the plane-wave basis functions with cut off energy of 410 eV were considered. The Gaussian smearing of width 0.05 eV was carried out for Brillouin zone integration except for density of states calculations where tetrahedron method with Blöchl corrections were used. The electronic band structures were calculated by considering both spin-orbit coupling (SOC) and without spin-orbit coupling (WSOC). The hydrostatic pressure was applied from 1 GPa to 10 GPa and optimization of the pressure induced structures were implemented with total energy convergence tolerance of 1.5×10^{-9} eV and force convergence tolerance of 0.0154 $eV/\AA$.

All the simulations were performed by imposing the symmetry preserved constraint, as this study is focused on isosymmetric lattice contraction. For the simulations of the mechanical properties, the elastic stiffness constants, matrices $[C_{ij}]$, were computed using the stress-strain relationships for all the pressure induced optimized structures [280]. The bulk modulus B and the shear modulus G were calculated from the matrix $[C_{ij}]$ using the Voigt-Reuss-Hill (VRH) averaging scheme [185, 281],

$$\begin{aligned} B_v = B_R &= \frac{C_{11}+2C_{12}}{3} \\ B &= \frac{1}{2}(B_v + B_R) \end{aligned} \tag{6.2}$$

$$\begin{aligned} G_v &= \frac{C_{11}-C_{12}+3C_{44}}{5} \\ G_R &= \frac{5C_{44}(C_{11}-C_{12})}{4C_{44}+3(C_{11}-C_{12})} \\ G &= \frac{1}{2}(G_v + G_R) \end{aligned} \tag{6.3}$$

The bulk modulus was also calculated by fitting the pressure-volume (P-V) data points using the Birch-Murnaghan 3^{rd} order equation of state [282],

$$P(V) = \frac{3B}{2}[(\frac{V_0}{V})^{7/3} - (\frac{V_0}{V})^{5/3}][1 + \frac{3}{4}(B^{'} - 4)((\frac{V_0}{V})^{2/3} - 1)] \tag{6.4}$$

where, V_0 is the equilibrium volume and $B^{'} = \frac{dB}{dP}$. The mechanical nature of all these structures were quantified by measuring Pugh ratio (B/G) and normalized Cauchy pressure ($\frac{C_{12}-C_{44}}{E}$), where E is the Young's modulus calculated as in [283],

$$E = \frac{9BG}{3B+G} \tag{6.5}$$

The optical properties were analyzed for all the pressure induced structures by calculating the frequency (ω) dependent dielectric functions, $\varepsilon(\omega) = \varepsilon_1(\omega) + i\varepsilon_2(\omega)$, where imaginary part is calculated as,

$$\varepsilon_2(\omega) = \frac{e^2 h}{\pi m^2 \omega^2} \sum_{v,c} \int_{BZ}^{\infty} |M_{cv}(k)|^2 \delta[\omega_{cv}(k) - \omega] d^3k \tag{6.6}$$

where, M_{cv} is the momentum matrix for a vertical transition from a filled initial state to an empty final state. The corresponding real part is calculated from the imaginary part using Kramers-Kronig transformation. Likewise, the estimation of the optical parameters such as the absorption coefficient (α), reflectivity (R) and refractive index (n) were performed according to the relations [206, 207, 284],

$$\alpha(\omega) = \frac{2\omega}{c} [\frac{\{\varepsilon_1^2(\omega) + \varepsilon_2^2(\omega)\}^{1/2} - \varepsilon_1(\omega)}{2}]^{1/2} \tag{6.7}$$

$$n(\omega) = [\frac{\{\varepsilon_1^2(\omega) + \varepsilon_2^2(\omega)\}^{1/2} + \varepsilon_1(\omega)}{2}]^{1/2} \tag{6.8}$$

$$R(\omega) = \frac{(n-1)^2 + (\frac{\alpha c}{2\omega})^2}{(n+1)^2 + (\frac{\alpha c}{2\omega})^2} \tag{6.9}$$

where c is the speed of light.

6.3 Results and Discussion

We have selected cubic halide perovskites ABX_3 ($A = K, Rb, Cs$; $B = Ge, Sn, Pb$ and $X = Cl, Br, I$) and studied how their structures and electro-optical properties vary due to the exchange of cation and anion in their respective group of the periodic table, under

the influence of isosymmetric compression. The lattice parameter (a_0), band gap (E_g) and bulk modulus (B) of various optimized structures along with their corresponding available experimental and theoretical values are shown in Table 6.1. Our calculated lattice parameters overestimate experiment by 2%, as expected given that they were calculated using the PBE. Likewise, the band gap severely underestimates experiment under WSOC by 9%-49% and the underestimation is even worse due to SOC. The reason for the closer proximity of WSOC may be due to a fortuitous error cancellation between the neglect of quasi-particle correction and spin-orbit coupling. However, since we are only interested in trends, this underestimation is not problematic. Further, the bulk modulus values obtained by fitting the third-order Birch-Murnaghan equation 6.4 match well with those calculated from elastic tensor matrices. The bond length variations of $A-X$ and $B-X$ along with their compressibilities were calculated to quantify whether the simulations yield optimized isosymmetric structures for all cubic compressed structures. The variations in bond lengths with pressure are shown in Figure 6.1, which satisfy the condition $< A-X >= \sqrt{2} < B-X >$. Similarly, from the compressibility point of view, it is hitherto understandable that the compressibility of polyhedron AX_{12} should match with the polyhedron BX_6 under isosymmetric compression. Their variations are also shown in Figure 6.2, which implicitly yields the condition for isosymmetric cubic structure contraction as $V_{A-X} = 3.24 \times V_{B-X}$, where V_{A-X} and V_{B-X} are the volumes of polyhedra AX_{12} and BX_6 respectively. The structural variations of lattice parameters of these perovskites, under hydrostatic pressure, are highlighted in Figure 6.3. The lattice parameter varies inversely with compression and it can be seen that a quadratic model of the form $a(P) = a_0 + c_1P + c_2P^2$ can be used to describe the variation, where a_0 is the equilibrium lattice parameter, c_1 and c_2 are negative and positive coefficients respectively. One can further notice that the size of the atomic radius contributes significantly to the variation of the lattice parameters.

Table 6.1 Calculated Values of Lattice Parameters (a_0), Energy Gap (E_g) and Bulk Modulus (B)

Materials	a_0(Å)		E_g (eV)			B(GPa)	
	this work	literature	this work WSOC	this work SOC	literature	this work	literature
$CsPbCl_3$	5.714	5.605[a] [285]	2.27	1.10	3.0[a] [286]	23.690[c],23.464[d]	21.54[b],22.59[b],31[b],25.8[b] [287]
$CsPbBr_3$	5.989	5.87[a] [285]	1.87	0.69	2.25[a]-2.30[a] [248, 286]	18.845[c],18.956[d]	18.45[b],27[b],23.5[b] [287]
$CsPbI_3$	6.384	6.289[a] [285]	1.59	0.35	1.73[a] [288]	14.904[c],14.998[d]	14.38[b],14.4[b],19.8[b],23[b] [287]
$CsGeI_3$	5.991	5.98[a]-6.05[a] [258, 285]	0.83	0.4	1.63[a] [289]	17.824[c],18.265[d]	18.89[b] [287]
$CsSnI_3$	6.273	6.219[a] [285]	0.68	0.08	1.31[a] [290]	15.22[c],15.754[d]	15.10[b],17.59[b],6.30[b] [291]
$KPbI_3$	6.337	6.352[b] [292]	1.54	0.28	1.36[b] [292]	15.261[c],15.939[d]	-
$RbPbI_3$	6.359	6.366[b] [292]	1.57	0.31	1.37[b] [292]	15.536[c],15.284[d]	-

a experimental value of room-temperature phase, *b* theoretical value of cubic phase; obtained using -*c* third-order Birch-Murnaghan EOS, *d* elastic tensor matrix

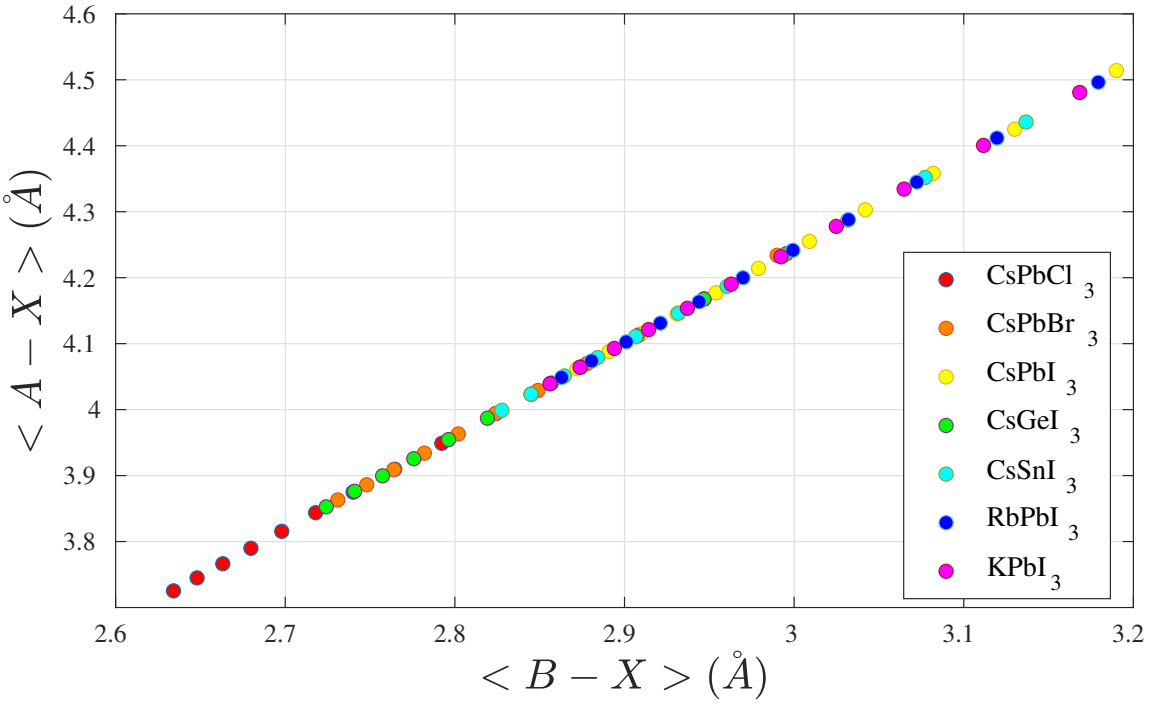

Figure 6.1 The bond length variation under isosymmetric lattice contraction.

For the size of atomic radius $K < Rb < Cs$, $Ge < Sn < Pb$ and $Cl < Br < I$, the order of variations in lattice parameters are $KPbI_3 < RbPbI_3 < CsPbI_3$, $CsGeI_3 < CsSnI_3 < CsPbI_3$ and $CsPbCl_3 < CsPbBr_3 < CsPbI_3$ respectively. This is due to the fact that there is no contribution of bonding to lattice variation in these structures as these alkali metals, crystallogens and halogens have the same number of valence electrons down their respective groups of the periodic table. The size of cation and anion is also associated with the compressibility. The smaller the size, the smaller the bond lengths $< A - X >$ and $< B - X >$, which in turn results in smaller compressibility. The compressibility in perovskites is usually dominated by the bond length $< A - X >$ due to the larger volume of the polyhedron $[A - X]_{12}$. However, for isosymmetric contraction, both $< A - X >$ and $< B - X >$ play equal role as shown earlier in Figure 6.2. Thus, it can be said that $CsPbCl_3$ shows more resistance to deformation than $CsPbBr_3$ and $CsPbI_3$ because of its smaller size anion and the order follows in accordance with the size of their respective anions ($Cl < Br < I$). Likewise, similar comparison can be drawn for the remaining perovskites based

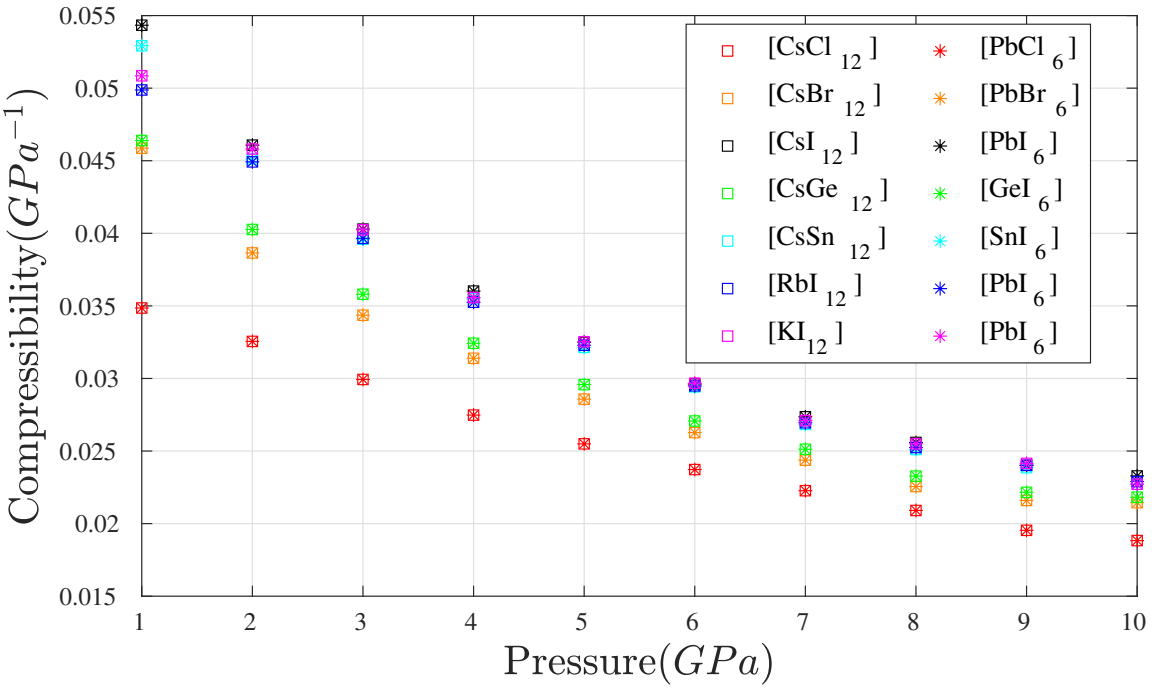

Figure 6.2 The variation of compressibility of the polyhedra in isosymmetric compression.

on the size of their respective cations. The effect of size can also be seen in the mechanical behavior of these materials. For instance, due to the higher compressibility, $CsPbI_3$ is softer and more ductile than $CsPbBr_3$ and $CsPbCl_3$. In other words, $CsPbI_3$ can withstand fracture longer than $CsPbBr_3$ and $CsPbCl_3$ under compression. Their deformation behavior can also be quantified by measuring Pugh ratio and normalized Cauchy pressure [293]. The Pugh ratio criterion [190] suggests that the materials show ductile nature when B/G ratio is greater than 1.75; otherwise, they exhibit brittle nature. Likewise, the Pettifor criterion [191] suggests that the materials develop covalent character when the Cauchy pressure is negative and hence possess brittle nature and vice-versa. The result is shown in Figure 6.4. According to Pugh ratio and Cauchy pressure criteria, except $CsGeI_3$, all of them show ductile character and ductility increases under isosymmetric compression. Therefore, the transition of materials from brittle character to ductile character might be achieved by the application of compression. According to the Pettifor criterion, $CsGeI_3$ shows greater tendency for directional bonding and therefore makes this material brittle.

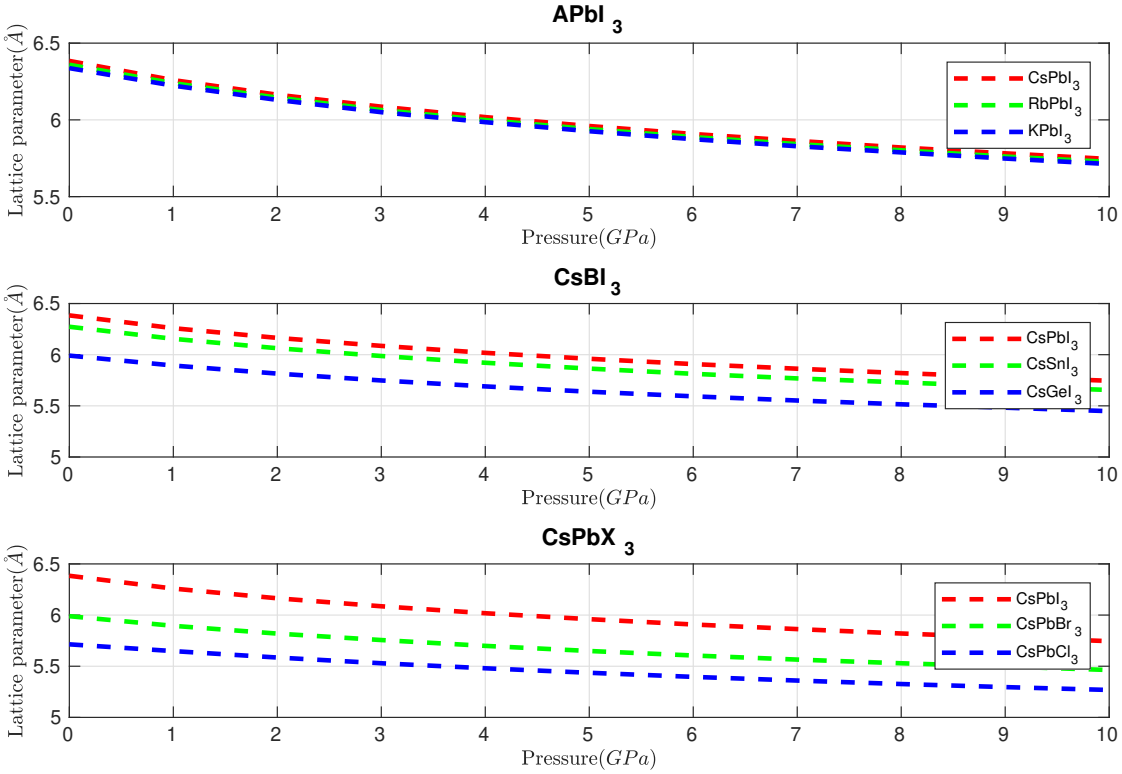

Figure 6.3 The lattice parameter variation as a function of the isosymmetric compression.

Moreover, one can notice that the red line is the longest among other ductile materials indicating that the associated material can rupture quicker during compression and the presence of discontinuity in the lines can be interpreted as the change in the nature of the bonding.

It has been observed that the alteration of cation and anion size contributes significantly to the macroscopic elastic properties. The very next implication would be the change in the electro-optical behaviors resulting from this alteration. The electronic behaviour can be studied by performing the band structure computations along the high symmetric path. As an example, due to the smaller size of the *Cl* atom, the lattice volume of $CsPbCl_3$ is the smallest among $CsPbBr_3$ and $CsPbI_3$. As a result, the volume of reciprocal space or the Brillouin zone (BZ) follows the order $CsPbCl_3 > CsPbBr_3 > CsPbI_3$. This effect has been shown by the dashed lines in the plots of Figure (6.5). The dashed lines indicate that the resulting position of high symmetric K-points of $CsPbI_3$ is mapped in the band

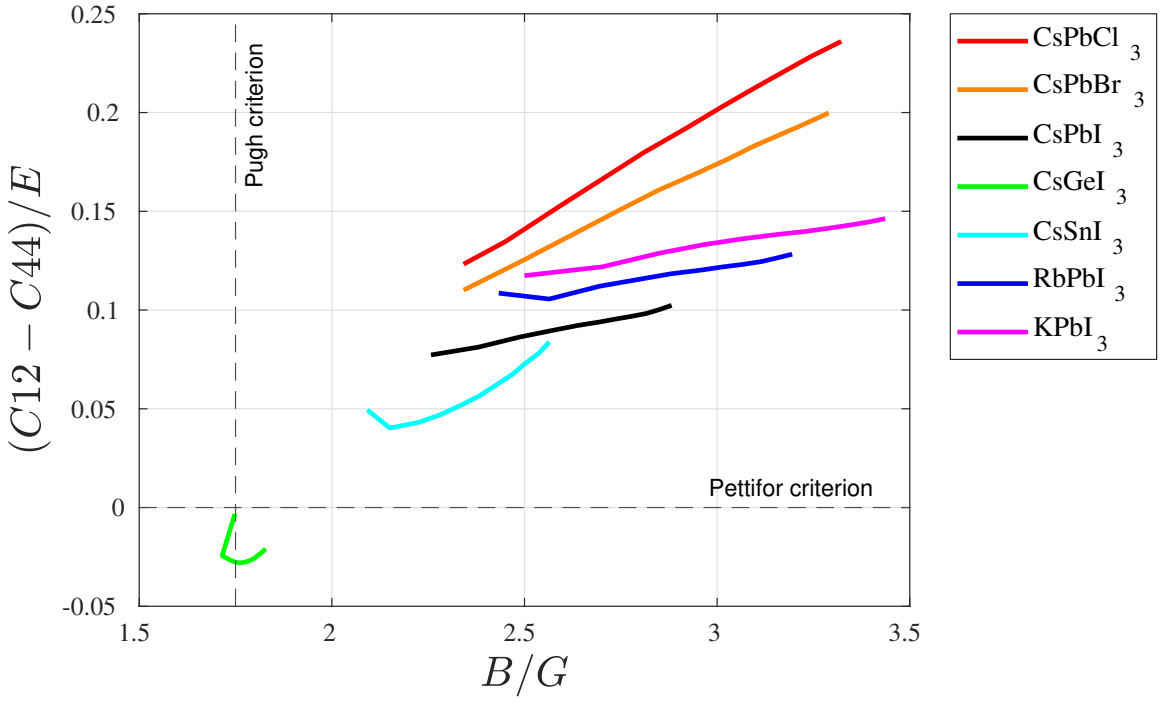

Figure 6.4 The brittle/ductile nature interpreted in terms of Pugh ratio and normalized Cauchy pressure.

structures of the remaining perovskites. Furthermore, due to compression, there is an increment in the Brillouin zone which can be seen from the position of dashed curves (in red and cyan color) in the band structures. One can notice that, all these perovskites are direct band gap materials with transition occurring at *R*-*R* symmetric points. Under isosymmetric compression of these structures, the band gap remains direct but reduces, thereby altering the semiconductor behavior towards metallic nature. It should be noted that the computed band structures in Figure 6.5, do not consider SOC. This is because the simulated band gap is worsened more by considering SOC than WSOC and, under isosymmetric compression, there is a probability of reducing the band gap to negative values. The density of states (DOS) and the individual contribution of each element or partial density of states (PDOS), in Figure 6.6, shows clearly that the hybridization of *s* orbital of *B* and *p* orbitals of *X* contribute to the valence band maxima (VBM) whereas the conduction band minima (CBM) is dominated by *p* orbitals of *B*. Further, the antibonding of *B*-*s* and *X*-*p* at VBM is significant resulting in covalent nature of the overlap. Unlike in

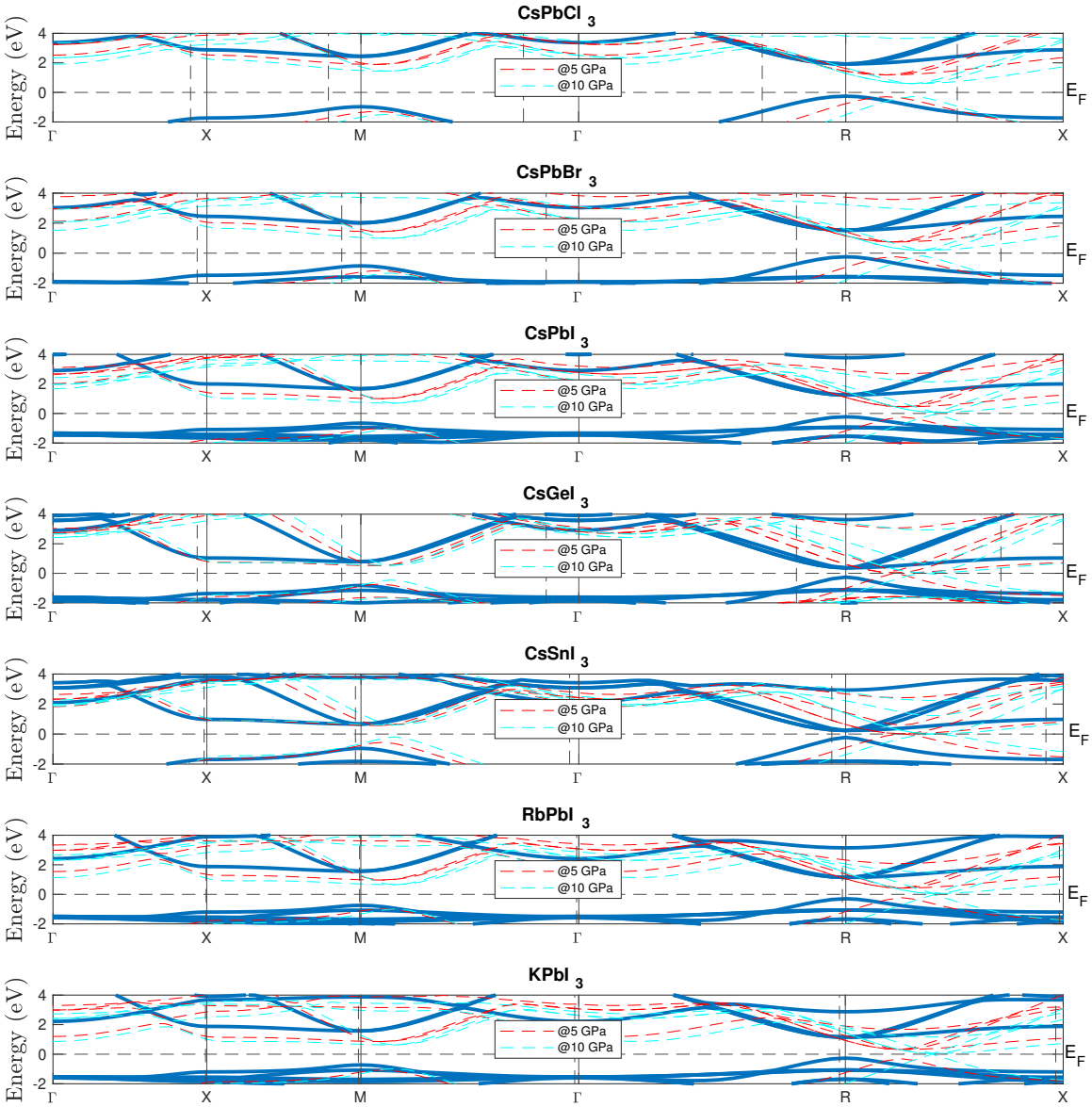

Figure 6.5 Electronic band structure of cubic halide perovskites in the high symmetric path under different pressure. The vertical dashed lines, except $CsPbI_3$, are used to denote high symmetric K-points of $CsPbI_3$ mapped into BZ of other perovskites.

VBM, the overlap in CBM has ionic nature as the band is singly dominated by p orbitals of B. Therefore, based on the analysis of DOS, the size of anion can influence the tuning of band gap in these halide perovskites in a definite order. For instance, the band gap varies in the order of $CsPbCl_3 > CsPbBr_3 > CsPbI_3$ indicating that the larger size of anion results

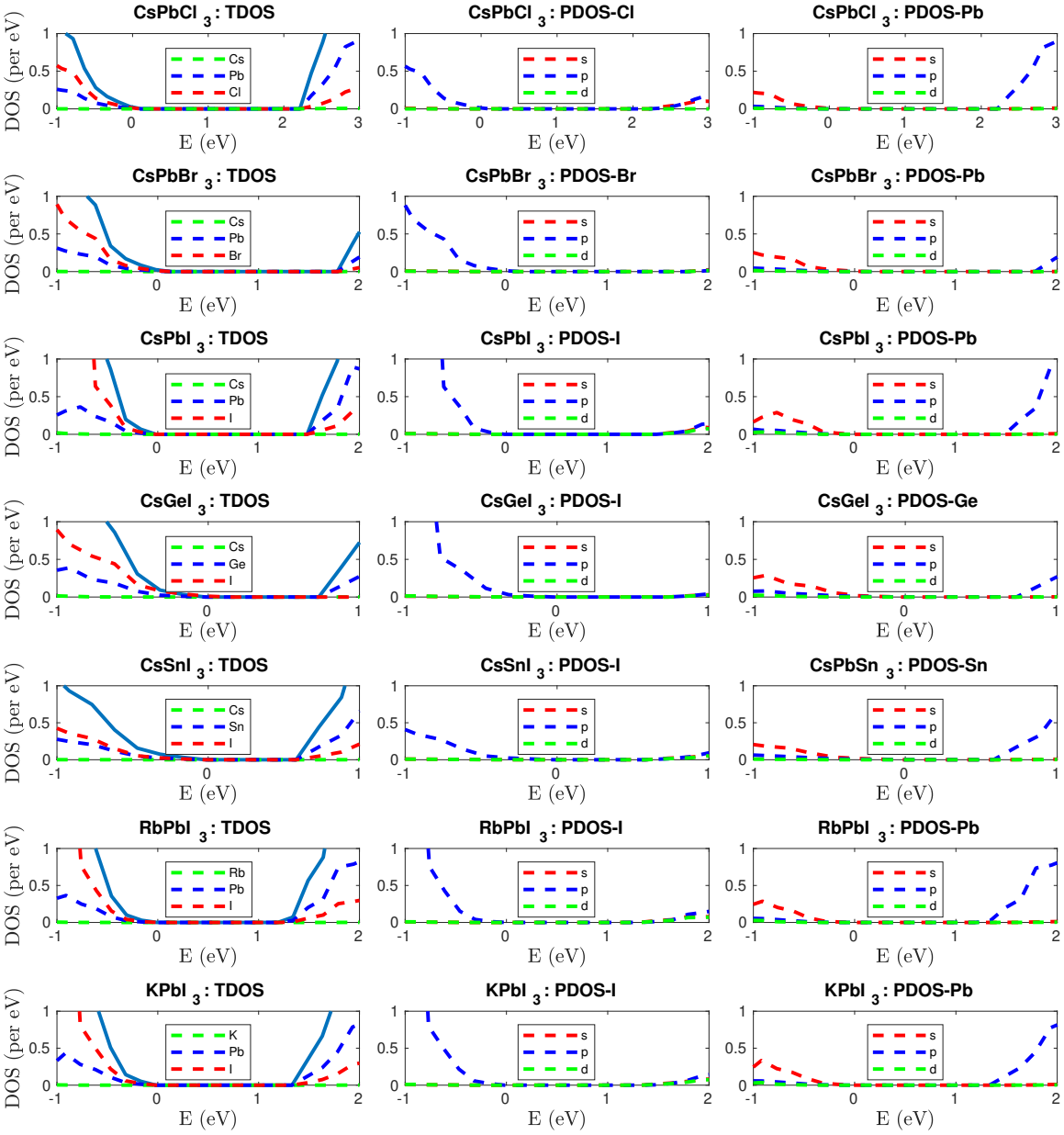

Figure 6.6 The density of states showing TDOS and PDOS of X and B with their orbitals contributions.

in red-shift of the band gap. However, the effect of cation size of alkali elements in the

PbI framework shows increase in the band gap ($KPbI_3 < RbPbI_3 < CsPbI_3$) with respect to size. Similarly, it is interesting to note that there is no definite size effect due to crystallogen cations in the band gap- as the band gap varies in the order of $CsSnI_3 < CsGeI_3 < CsPbI_3$ whereas size varies in the order of $Ge < Sn < Pb$. These trends of band gap variation, with respect to the order of the size of A cation and X anion, are the same with or without SOC. However, they are different for B cation. The variation of band gap under SOC follows the order $CsSnI_3 < CsPbI_3 < CsGeI_3$. This may be due to higher SOC corrections ($\Delta E_g^{SOC} = E_g^{SOC} - E_g^{WSOC}$) in $CsPbI_3$, which is 81% greater than $CsGeI_3$, as shown in Figure 6.7. The other possibility can be the choice of exchange-correlation functional or method implemented, which results in different magnitudes of quasi-particle corrections in these systems. In the work of Huang and Lambrecht [285], they have shown that the band gap follows the order $CsSnI_3 < CsGeI_3 < CsPbI_3$, under both SOC and WSOC, using quasi-particle self-consistent GW method. However, these conformities are violated, when anion I is replaced by anion Cl; plus all their results (trends of variation) agree with our under WSOC formalism. As the cubic phases of these perovskites are unstable at room temperature, it is very difficult to reckon the correct trend experimentally. Nevertheless, we have compared with their room-temperature phases and found that the trends in all the cation and anion variations do satisfy with the trends calculated under WSOC. All these variations can be explained based on the degree of overlap between B-s and X-p orbitals. For instance, one can notice from Figure 6.6 that the overlap in Sn-perovskite is more than that of Ge-perovskite and Pb-perovskite, suggesting that the band gap follows the order of $CsSnI_3 < CsGeI_3 < CsPbI_3$. Based on this observation, it can be said that the greater ionic nature of hybridization between B-s and X-p orbitals results in blue-shift of the band gap in halide perovskites. Further, the influence of compression on the lattice has been observed by the red-shift of DOS with increasing pressure.

For the optical properties, we have chosen independent particle approximation (IPA) to study optical parameters such as absorption coefficient (α), reflectivity (R) and refractive

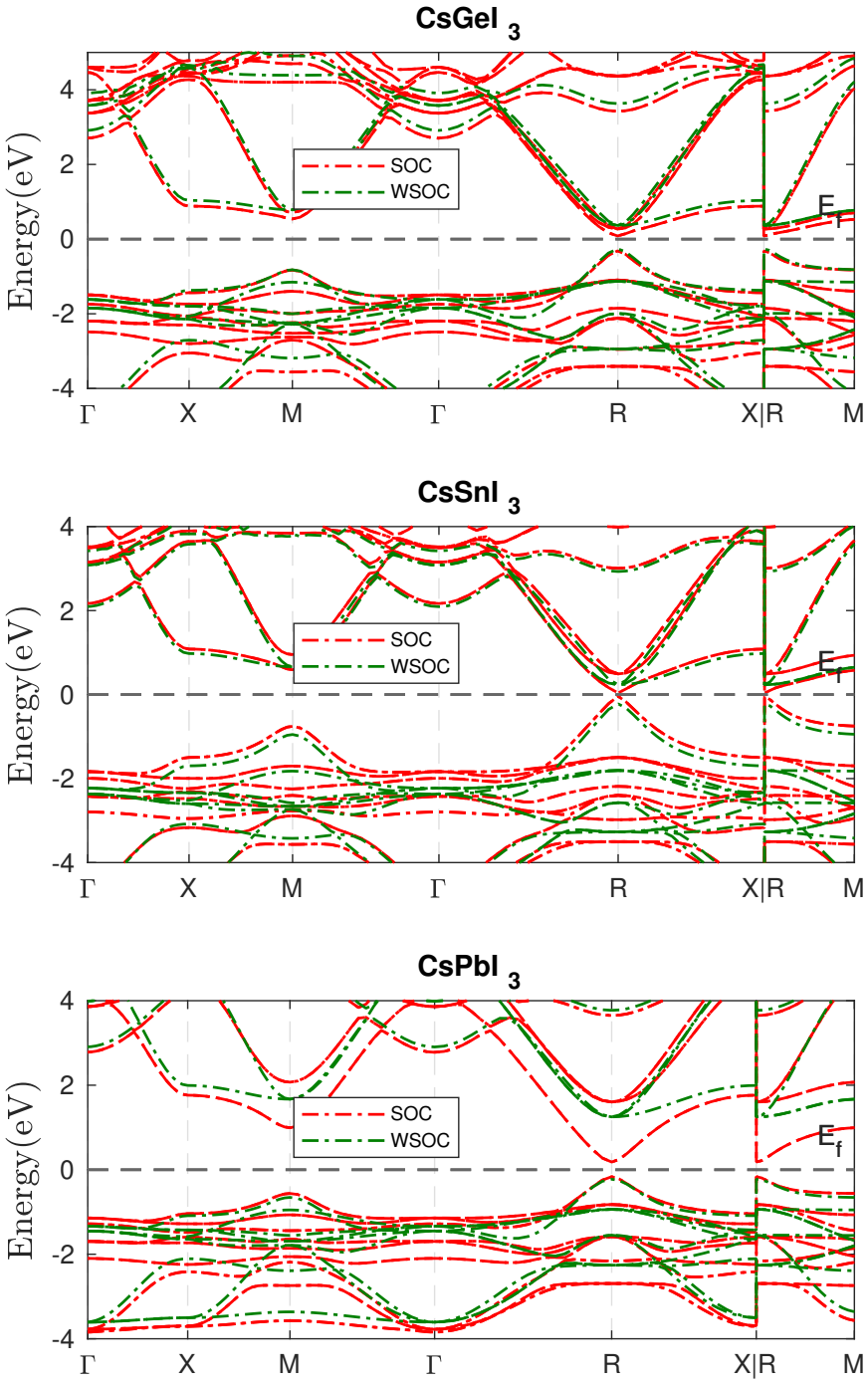

Figure 6.7 Doubly degenerate conduction bands due to SOC. The magnitudes of spin-orbit splitting increases from *Ge* to *Pb*.

index (n), under isosymmetric compression. One can notice from Figure 6.8 that all these materials show good absorption in the visible spectrum. The application of pressure increases the absorption coefficient towards low band gap. In contrast, reflectivity and refractive index are high at the beginning indicating opacity for time independent field. Likewise, the variation of refractive index can be interpreted based on the band gap. The computed static refractive index implies qualitatively that it varies inversely with the band gap and the order of refractive index $ABI_3 > ABBr_3 > ABCl_3$ can be explained as the larger size of anion I has comparatively more loose electrons resulting in higher degree of polarizability. As the accuracy of DFT calculations rely on the choice of exchange-correlation potential, the underestimation of band gap can also be thought as the overestimation of refractive index. For instance, our computed static refractive index for $CsPbBr_3$ and $CsPbI_3$ overestimate their experimental counterparts roughly by 8% and 14% respectively [123, 126]. Similarly, the effect of compression on these optical parameters can also be explained based on the shrinkage of the band gap. It can be seen that, under isosymmetric compression, materials with less band gap have higher optical parameters till the visible region and the pattern becomes opposite towards the ultra-violet region. On the other hand, one can qualitatively imply that the larger band gap materials show less optical response, even during compression.

6.4 Conclusions

To the best of our knowledge, this study has explored the idea of isosymmetric lattice compression for the first time in perovskites. We have studied the aftermath of the isosymmetric lattice compression in seven halide perovskites and some of the key findings are as follows: (a) the Goldschmidt tolerance factor remains unchanged, (b) the degree of compressibility of polyhedra AX_{12} matches well with their corresponding polyhedra BX_6, (c) the volume of these polyhedra satisfies the relation, $V_{A-X} = 3.24 \times V_{B-X}$, and (d) band gap decreases but the compression preserves the band gap nature. Since the changes in

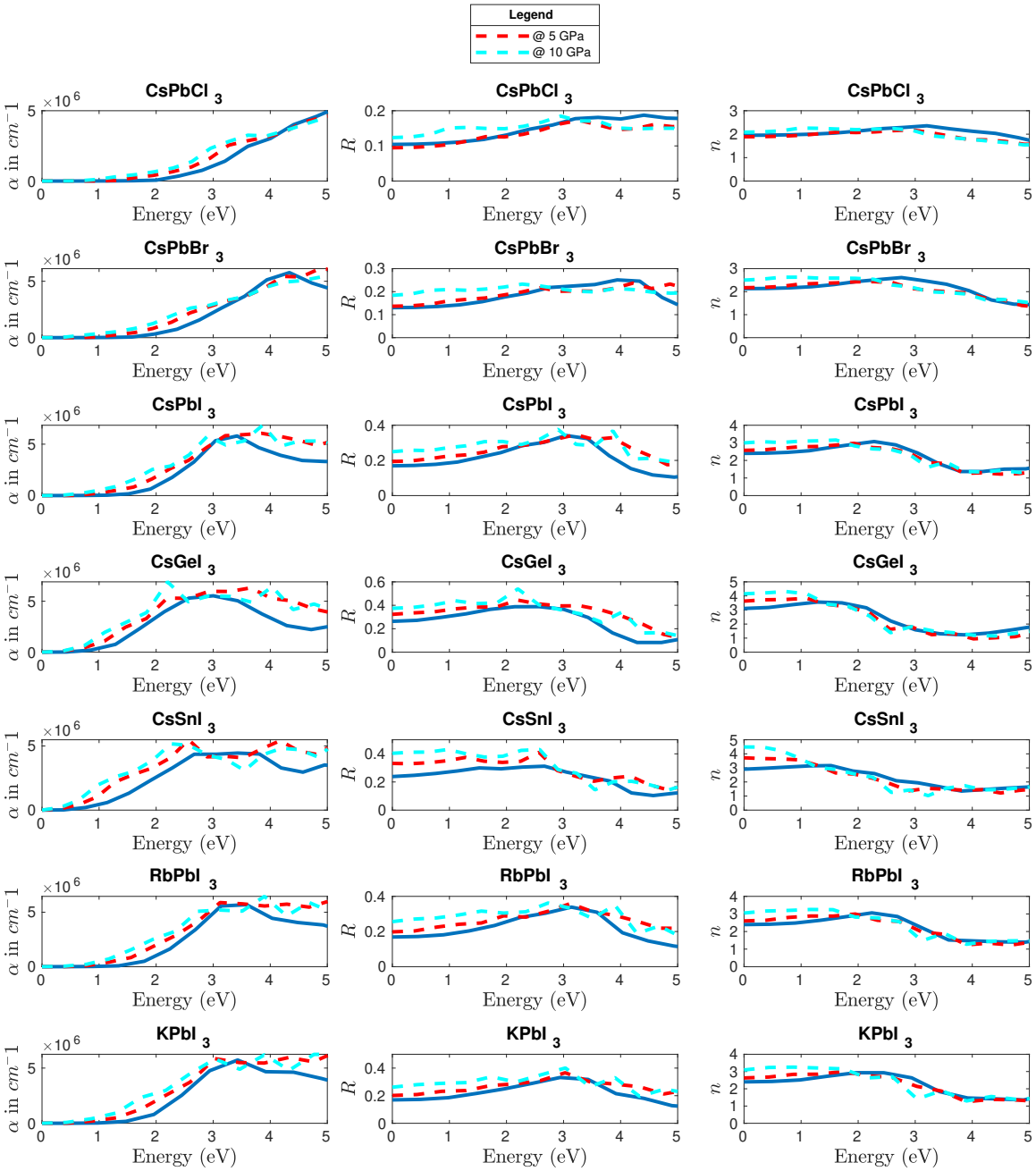

Figure 6.8 Optical spectra- absorption coefficient (α), reflectivity (R) and refractive index (n) as a function of pressure. Solid line represents normal conditions.

properties of perovskites emerge from the competition between octahedral tilt and lattice contraction, the study of isosymmetric lattice compression is significant as it isolates octahedral tilt. Further, the size reduction due to A cation and X anion is accompanied by the widening of band gap, and there is no definite pattern in the band gap variation due to B cation. It is observed that band gap widening is caused by a decrease in overlap between B-s and X-p and vice-versa. From this study, one can remark that the overlap between B-s and X-p increases with isosymmetric lattice contraction, implying that such changes may have been anomalous if the octahedral tilting is taken into account. Moreover, the study has qualitatively shown the inverse relation between band gap and refractive index with the larger band gap materials showing less optical response. All the studied materials have intrinsic direct band gap matching the solar spectrum and show good absorption for the visible spectrum. These photonic qualities can be further enhanced with isosymmetric strains. The application of isosymmetric stress resists the external conditions and therefore allows these potent solar materials to behave predictably. Such information may be useful to design optoelectronic devices such as LEDs, solar cells etc.

CHAPTER 7

CONCLUSIONS

Density functional theory is the state-of-the-art technique for investigating the electronic structure of materials. Perovskites are multi-functional materials with properties ranging from dielectric, pyroelectric, piezoelectric, ferroelectric and ferromagnetic, therefore, making them suitable for various optoelectronic devices. In this dissertation, we have studied various oxides and halide perovskites, using density functional theory.

In Chapter 1, we started by surveying the evolution of computational materials science. Its present status is prominent among various other disciplines of sciences, in not only predicting the properties of the given material but also discovering new materials based on given properties. A brief introduction to the perovskites is presented describing structural properties along with deformation and other modular forms.

In Chapter 2, the theoretical foundation of density functional theory is presented, beginning with the limitations of applying Schrödinger equation in the multi-body system. Then an elementary theoretical description of different properties of materials, viz., structural, elastic, electronic, and optical is discussed.

In Chapter 3, we have presented a model which relates the energy gap with the refractive index. This model has been tested among different perovskites, yielding accuracy on par with the other well-established models.

In Chapter 4, a detailed study of the structural, elastic, electronic, and optical properties of some alkaline earth metal zirconate perovskites is performed, using both standard and hybrid functionals. The effect of the size of *A* cation on the overall properties can be analyzed. It is found that increasing the size of *A* cation leads to higher stability. The phonon dispersion indicates that these zirconate perovskites are suitable for thermal coating materials and the electronic dispersion designates them as insulators. The internal bond

strength is studied by quantifying charge flow due to coupling between lattice displacement and electrostatic field. Further, the dimensionless constant in the Penn model was predicted to be 0.86. Besides parsing the properties, Chapter 4 implicitly describes the efficacy between standard and hybrid functionals.

Chapter 5 describes *Cs-Pb-Br* variants such as $CsPbBr_3$ and its 2D counterparts Cs_2PbBr_4 and $CSPb_2Br_5$. The structural phase transition from tetragonal to orthorhombic crystal system is predicted below 200 K and from tetragonal to cubic above 400 K. It is found that the former transition is second order and the latter is the first order. $CsPbBr_3$ and Cs_2PbBr_5 have a direct band gap and the absorption of photons is higher in the visible region, whereas $CsPb_2Br_5$ has indirect band gap and absorption is higher at the UV region. Likewise, the exciton binding energy of 2D counterparts is higher due to the lesser screening effect.

Chapter 6 presents the notion of isosymmetric stress and its effect on several cubic halide perovskites ABX_3 ($A = K, Rb, Cs$; $B = Ge, Sn, Pb$ and $X = Cl, Br, I$). The exchange of cations A, B, and anion X on the overall properties are analyzed. The non-trivial effects in band structure due to spin-orbit coupling are studied.

APPENDIX

INTRODUCTION TO VASP

A brief description of VASP, as mentioned in chapter 1, is described in this section.

VASP (Vienna Ab Initio Simulation Package) is one of the important packages for performing ab-initio quantum mechanical calculations, using pseudo-potentials and a plane wave basis set. It can easily operate and handle an atomistic system containing 100-200 atoms. The bulk system can be modeled better than the isolated system or molecule as the code utilizes periodic boundary conditions. VASP requires at least four input files. They are as follows:

i) INCAR is a central file, containing the setting tags of the parameters, as per the need of the calculations.

ii) POSCAR contains information about the geometry of the system.

iii) POTCAR contains information about the potentials, exchange-correlation functional, valence and core electrons, etc.

iv) KPOINTS contains the set of k-points for sampling the first Brillouin zone.

Except for the POTCAR file, the input files need to be prepared based on the atomistic system and level of convergence. The POTCAR file can be found on the database and the pseudopotentials in it must follow the same sequence as the POSCAR file. After successful convergence of any calculations, the VASP generates its output in two formats. The first one is the text format and the output is written in the files CONTCAR, EIGENVAL, OUTCAR, OSZICAR, DOSCAR, etc. The next output format is the xml format and the name of the file is vasprun.xml. These output files can be parsed and made compatible with various post-processing tools such as Vesta, Matlab, or Python scripts, etc. The detailed tutorial about atomic-scale materials modeling using VASP can be found at "https://www.vasp.at".

As an illustration to describe some of the important setting tags needed to prepare INCAR file for high throughput results for structural optimization are shown below,

PREC= Accurate
ADDGRID=.TRUE.
EDIFF=$1e^{-8}$
EDIFFG=$-5e^{-4}$
ISIF=3
IBRION=2
NSW=200
NELMIN=5

PREC tag is used to control the precision of the calculations. The tag ADDGRID= .TRUE. is used to add an additional grid for charge augmentation. EDIFF=$1e^{-8}$ implies that the electronic relaxation terminates when the total energy change becomes less than $1e^{-8}$ eV. Similarly, the EDIFFG tag is used for ionic relaxation. In this case, the ionic relaxation will stop, when the forces acting on the ions are smaller than $5e^{-4}$. ISIF determines the degree of freedom to be updated during the relaxation of the structure. ISIF=3 is good for bulk structure relaxation which allows ionic positions, cell shape, and

volume to change during optimization. For 2D structures, ISIF=2 or 3 are more preferable. IBRION tag controls the movement of ions. For structural optimization, IBRION=2 is frequently used. Likewise, IBRION= 0 describes molecular dynamics, IBRION=6 is used to calculate Hessian and Stiffness matrices, and IBRION=8 for phonon calculations using density functional perturbation method. NSW and NELMIN describe the number of ionic and electronic steps, respectively.

Besides these tags, there are other useful tags such as ISYM, ENCUT, LREAL, ISMEAR etc., which are used to increase convergence and accuracy of the calculations. ISYM tag tells VASP whether to consider symmetry or not. If the symmetry of the final structure is known pre-hand then the use of this tag increases the convergence. The symmetry should be off for any symmetry-breaking calculations such as spin-orbit coupling. ENCUT is another important tag that determines the cutoff energy for the plane-wave basis set. Generally, ENCUT and KPOINTS should be determined by setting convergence tests. Otherwise, ENCUT with 30% greater than ENMAX is roughly considered suitable. LREAL tag determines the evaluation of projection operator to be done in real space or reciprocal space. For a small system, the projection should be done at reciprocal space, which yields higher accuracy. ISMEAR tag provides a smearing method for the Brillouin zone sampling. Smearing is useful to avoid numerical problems, during finite sampling of the Brillouin zone. Gaussian smearing is used for structural optimization and tetrahedron smearing for accurate energy calculations. For comparison purposes, calculations need to be done with the same setup of PREC, ENCUT, LREAL, EDIFF, EDIFFG, and ISMEAR.

Among several output files of VASP, the chief files are CONTCAR, OSZICAR, OUTCAR, and DOSCAR. CONTCAR contains the geometry of the structure, which can later be named POSCAR for the continual of the job. OSZICAR contains information about total energy, energy change, convergence parameters, iteration, number of electronic and ionic steps, etc. OUTCAR is the central output file and contains all the information of the simulation. DOSCAR contains information about the density of states (DOS) and integrated DOS.

REFERENCES

[1] R. F. Mould. The Early History of X-ray Diagnosis with Emphasis on the Contributions of Physics 1895-1915. *Physics in Medicine and Biology*, 40(11):1741–1787, November 1995.

[2] M. Manutchehr-Danai, editor. *Laue Method*, pages 516–516. Springer Berlin Heidelberg, Berlin, Heidelberg, 2009.

[3] P. P. Ewald. Max von Laue, 1879-1960. *Biographical Memoirs of Fellows of the Royal Society*, 6:134–156, 1960.

[4] H. A. Hauptman. History of X-ray Crystallography. *Chemometrics and Intelligent Laboratory Systems*, 10(1):13–18, 1991. Proceedings of the Mathematics in Chemistry Conference.

[5] J. C. H. Spence. Lawrence Bragg, Microdiffraction and X-ray Lasers. *Acta Crystallographica Section A*, 69(1):25–33, January 2013.

[6] W. H. Bragg. The Reflection of X-rays by Crystals. *Nature*, 91(2280):477–477, June 1913.

[7] S. Mande. Early Developments in Crystallography. *Resonance*, 19(12):1077–1086, December 2014.

[8] T. Mulvey. Origins and Historical Development of the Electron Microscope. *British Journal of Applied Physics*, 13(5):197–207, May 1962.

[9] G. Braun, D. Tierney, and H. Schmitzer. How Rosalind Franklin Discovered the Helical Structure of DNA: Experiments in Diffraction. *The Physics Teacher*, 49(3):140–143, 2011.

[10] G. N. Lewis. The Specific Heat of Solids at Constant Volume, and the Law of Dulong and Petit. *Journal of the American Chemical Society*, 29(8):1165–1168, August 1907.

[11] U. Piespergen. Chapter 3 Heat Capacity and Debye Temperatures. In R.K. Willardson and A. C. Beer, editors, *Physics of III-V Compounds*, volume 2 of *Semiconductors and Semimetals*, pages 49–60. Elsevier, 1966.

[12] R. E. Peierls. Recollections of Early Solid State Physics. *Proceedings of the Royal Society of London. Series A, Mathematical and Physical Sciences*, 371(1744):28–38, 1980.

[13] J. D. Martin. What's in a Name Change? *Physics in Perspective*, 17(1):3–32, March 2015.

[14] N. Argaman and G. Makov. Density Functional Theory: An Introduction. *American Journal of Physics*, 68(1):69–79, January 2000.

[15] A. Jain, S. P. Ong, G. Hautier, W. Chen, W. D. Richards, S. Dacek, S. Cholia, D. Gunter, D. Skinner, G. Ceder, and K. Persson. The Materials Project: A Materials Genome Approach to Accelerating Materials Innovation. *APL Materials*, 1(1):011002, 2013. http://link.aip.org/link/AMPADS/v1/i1/p011002/s1&Agg=doi.

[16] E. A. Katz. Perovskite: Name Puzzle and German-Russian Odyssey of Discovery. *Helvetica Chimica Acta*, 103(6):e2000061, 2020.

[17] V. M. Goldschmidt. Die Gesetze der Krystallochemie. *Naturwissenschaften*, 14(21):477–485, May 1926.

[18] M. Johnsson and P. Lemmens. Crystallography and Chemistry of Perovskites. In *Handbook of Magnetism and Advanced Magnetic Materials*. American Cancer Society, 2007. https://onlinelibrary.wiley.com/doi/abs/10.1002/9780470022184.hmm411.

[19] C. Li, X. Lu, W. Ding, L. Feng, Y. Gao, and Z. Guo. Formability of ABX3 (X = F, Cl, Br, I) Halide Perovskites. *Acta Crystallographica. Section B, Structural science*, 64 Pt 6:702–7, 2008.

[20] H. A. Jahn and W. H. Bragg. Stability of Polyatomic Molecules in Degenerate Electronic States II-Spin Degeneracy. *Proceedings of the Royal Society of London. Series A - Mathematical and Physical Sciences*, 164(916):117–131, 1938.

[21] J. Akhtar, M. Aamir, and M. Sher. Chapter 2 - Organometal Lead Halide Perovskite. In S. Thomas and A. Thankappan, editors, *Perovskite Photovoltaics*, pages 25–42. Academic Press, 2018.

[22] A. M. Glazer. The Classification of Tilted Octahedra in Perovskites. *Acta Crystallographica Section B*, 28(11):3384–3392, November 1972.

[23] C. J. Howard and H. T. Stokes. Group-Theoretical Analysis of Octahedral Tilting in Perovskites. *Acta Crystallographica Section B*, 54(6):782–789, December 1998.

[24] A. M. Glazer. Simple Ways of Determining Perovskite Structures. *Acta Crystallographica Section A*, 31(6):756–762, November 1975.

[25] M. M. Stylianakis. Optoelectronic Nanodevices. *Nanomaterials (Basel, Switzerland)*, 10(3):520, March 2020. nano10030520[PII].

[26] A. Kojima, K. Teshima, Y. Shirai, and T. Miyasaka. Organometal Halide Perovskites as Visible-Light Sensitizers for Photovoltaic Cells. *Journal of the American Chemical Society*, 131(17):6050–6051, May 2009.

[27] G. Schileo and G. Grancini. Halide Perovskites: Current Issues and New Strategies to Push Material and Device Stability. *Journal of Physics: Energy*, 2(2):021005, February 2020.

[28] S. K. Sahoo, B. Manoharan, and N. Sivakumar. Chapter 1 - Introduction: Why Perovskite and Perovskite Solar Cells? In Sabu Thomas and Aparna Thankappan, editors, *Perovskite Photovoltaics*, pages 1–24. Academic Press, 2018.

[29] G. Kresse and J. Furthmüller. Efficient Iterative Schemes for Ab Initio Total-Energy Calculations using A Plane-Wave Basis Set. *Phys. Rev. B*, 54:11169–11186, October 1996. https://link.aps.org/doi/10.1103/PhysRevB.54.11169.

[30] G. Kresse and J. Hafner. Ab Initio Molecular Dynamics for Liquid Metals. *Phys. Rev. B*, 47:558–561, January 1993. https://link.aps.org/doi/10.1103/PhysRevB.47.558.

[31] I. Falconer. J. J. Thomson and the Discovery of the Electron. *Physics Education*, 32(4):226–231, July 1997.

[32] H. P. gen. Schieck. Rutherford Scattering and the Atomic Nucleus. In *Key Nuclear Reaction Experiments*, 2053-2563, pages 2–1 to 2–9. IOP Publishing, 2015.

[33] M. A. B. Whitaker. The Bohr-Moseley Synthesis and A Simple Model for Atomic X-ray Energies. *European Journal of Physics*, 20(3):213–220, January 1999.

[34] J. Kohanoff. *Electronic Structure Calculations for Solids and Molecules: Theory and Computational Methods*. Cambridge University Press, 2006.

[35] P. Hohenberg and W. Kohn. Inhomogeneous Electron Gas. *Phys. Rev.*, 136:B864–B871, November 1964.

[36] E. H. Lieb and B. Simon. The Thomas-Fermi Theory of Atoms, Molecules and Solids. *Advances in Mathematics*, 23(1):22–116, 1977.

[37] J. Žofka. Application of the Hartree-Fock Method in Nuclear Theory. *Czechoslovak Journal of Physics B*, 20(8):926–938, August 1970.

[38] R. Latter. Atomic Energy Levels for the Thomas-Fermi and Thomas-Fermi-Dirac Potential. *Phys. Rev.*, 99:510–519, July 1955.

[39] R. M. Martin. *Electronic Structure: Basic Theory and Practical Methods*, chapter Density functional theory. Cambridge University Press, 2004.

[40] W. Kohn and L. J. Sham. Self-Consistent Equations Including Exchange and Correlation Effects. *Phys. Rev.*, 140:A1133–A1138, November 1965.

[41] J. P. Perdew, K. Burke, and M. Ernzerhof. Generalized Gradient Approximation Made Simple. *Phys. Rev. Lett.*, 77:3865–3868, October 1996.

[42] F. Bloch. Über die Quantenmechanik der Elektronen in Kristallgittern. *Zeitschrift für Physik*, 52(7):555–600, July 1929.

[43] M. Li, Y. Wang, A. Chen, A. Naidu, B. S. Napier, W. Li, C. L. Rodriguez, S. A. Crooker, and F. G. Omenetto. Flexible magnetic composites for light-controlled actuation and interfaces. *Proceedings of the National Academy of Sciences*, 115(32):8119–8124, 2018.

[44] P. C. Reshmi Varma. Chapter 7 - Low-Dimensional Perovskites. In S. Thomas and A. Thankappan, editors, *Perovskite Photovoltaics*, pages 197 – 229. Academic Press, 2018.

[45] I. Hussain, H. P. Tran, J. Jaksik, J. Moore, N. Islam, and M. J. Uddin. Functional Materials, Device Architecture, and Flexibility of Perovskite Solar Cell. *Emergent Materials*, 1(3):133–154, December 2018. https://doi.org/10.1007/s42247-018-0013-1.

[46] J. Young and J. M. Rondinelli. Octahedral Rotation Preferences in Perovskite Iodides and Bromides. *The Journal of Physical Chemistry Letters*, 7(5):918–922, 2016. https://doi.org/10.1021/acs.jpclett.6b00094.

[47] F. Dogan, H. Lin, M. Guilloux-Viry, and O. Peña. Focus on Properties and Applications of Perovskites. *Science and Technology of Advanced Materials*, 16(2):020301, April 2015. https://doi.org/10.1088%2F1468-6996%2F16%2F2%2F020301.

[48] X. Dai, K. Xu, and F. Wei. Recent Progress in Perovskite Solar Cells: The Perovskite Layer. *Beilstein Journal of Nanotechnology*, 11:51–60, 2020.

[49] Y. Mao, H. Zhou, and S. S. Wong. Synthesis, Properties, and Applications of Perovskite - Phase Metal Oxide Nanostructures. *Material Matters*, 2010.

[50] M. Petrović, V. Chellappan, and S. Ramakrishna. Perovskites: Solar Cells and Engineering Applications – Materials and Device Developments. *Solar Energy*, 122:678 – 699, 2015. http://www.sciencedirect.com/science/article/pii/S0038092X15005277.

[51] L. F. Schneemeyer, J. V. Waszczak, S. M. Zahorak, R. B. van Dover, and T. Siegrist. Superconductivity in Rare Earth Cuprate Perovskites. *Materials Research Bulletin*, 22(11):1467 – 1473, 1987.

[52] W. Li and L.-J. Ji. Perovskite Ferroelectrics Go Metal Free. *Science*, 361(6398):132–132, 2018. https://science.sciencemag.org/content/361/6398/132.

[53] E. A. R. Assirey. Perovskite Synthesis, Properties and Their Related Biochemical and Industrial Application. *Saudi Pharmaceutical Journal*, 27(6):817 – 829, 2019. http://www.sciencedirect.com/science/article/pii/S1319016419300726.

[54] H. Wei and J. Huang. Halide Lead Perovskites for Ionizing Radiation Detection. *Nature Communications*, 10:1066, 03 2019.

[55] X. Liu, W. Zhao, H. Cui, Y. Xie, Y. Wang, T. Xu, and F. Huang. Organic-Inorganic Halide Perovskite Based Solar Cells - Revolutionary Progress in Photovoltaics. *Inorg. Chem. Front.*, 2, 02 2015.

[56] A. Jayatissa and Z. Shi. Perovskites-Based Solar Cells: A Review of Recent Progress, Materials and Processing Methods. 05 2018.

[57] H. Wells. Über die Cäsium- und Kalium-Bleihalogenide. *Zeitschrift für anorganische Chemie*, 3:195 – 210, 11 2004.

[58] C. K. Møller. *The Structure of Caesium Plumbo Iodide $CsPbI_3$*. Matematisk-fysiske meddelelser ; 32,1, Munksgaard [in Komm.],København, 1959.

[59] C. Zhang, A. G. Manohari, C. Liu, J. Hu, Y. Yang, R.E.I. Schropp, and Y. Mai. Inorganic Halide Perovskite Materials and Solar Cells. *APL Materials*, 7:120702, 12 2019.

[60] H. P. Pasanen, P. Vivo, L. Canil, A. Abate, and N. Tkachenko. Refractive Index Change Dominates The Transient Absorption Response of Metal Halide Perovskite Thin Films in The Near Infrared. *Phys. Chem. Chem. Phys.*, 21:14663–14670, 2019. http://dx.doi.org/10.1039/C9CP02291K.

[61] W. Xiao, D. Tan, W. Zhou, J. Liu, and J. Xu. Cubic Perovskite Polymorph of Strontium Metasilicate at High Pressures. *American Mineralogist*, 98(11-12):2096–2104, 11 2013. https://doi.org/10.2138/am.2013.4470.

[62] X.-G. Zhao, G. M. Dalpian, Z. Wang, and A. Zunger. The Polymorphous Nature of Cubic Halide Perovskites. *Phys. Rev. B*, 101:155137, April 2020. https://link.aps.org/doi/10.1103/PhysRevB.101.155137.

[63] P. Wang, J. Guan, D.T.K Galeschuk, Y. Yao, C.F. He, S. Jiang, S. Zhang, Y. Liu, M. Jin, C. Jin, and Y. Song. Pressure-Induced Polymorphic, Optical, and Electronic Transitions of Formamidinium Lead Iodide Perovskite. *The Journal of Physical Chemistry Letters*, 8 10:2119–2125, 2017.

[64] Q. Ou, X. Bao, Y. Zhang, H. Shao, G. Xing, X. Li, L. Shao, and Q. Bao. Band Structure Engineering in Metal Halide Perovskite Nanostructures for Optoelectronic Applications. *Nano Materials Science Special Issue on Two-Dimensional Nanomaterials*, 1(4):268 – 287, 2019.

[65] H. Zhaosheng, Z. Lin, J. Su, J. Zhang, J. Chang, and Y. Hao. A Review on Energy Band-Gap Engineering for Perovskite Photovoltaics. *Solar RRL*, 09 2019.

[66] T. Geng, Z. Ma, Y. Chen, Y. Cao, P. Lv, N. Li, and G. Xiao. Bandgap Engineering in Two-Dimensional Halide Perovskite $Cs_3Sb_2I_9$ Nanocrystals Under Pressure. *Nanoscale*, 12:1425–1431, 2020. http://dx.doi.org/10.1039/C9NR09533K.

[67] M.-J. Wu, C.-C. Kuo, L.-S. Jhuang, P.-H. Chen, Y.-F. Lai, and F.-C. Chen. Bandgap Engineering Enhances The Performance of Mixed-Cation Perovskite Materials for Indoor Photovoltaic Applications. *Advanced Energy Materials*, 9(37):1901863. https://onlinelibrary.wiley.com/doi/abs/10.1002/aenm.201901863.

[68] N. M. Ravindra, P. Ganapathy, and J. Choi. Energy Gap–Refractive Index Relations in Semiconductors – An Overview. *Infrared Physics and Technology*, 50(1):21 – 29, 2007. http://www.sciencedirect.com/science/article/pii/S135044950600048X.

[69] S. K. Tripathy and A. Pattanaik. Optical and Electronic Properties of Some Semiconductors from Energy Gaps. *Optical Materials*, 53:123 – 133, 2016.

[70] V. Kumar and J. Singh. Model for Calculating The Refractive Index of Different Materials. *Indian Journal of Pure and Applied Physics*, 48, 08 2010.

[71] P. M. Celliers, M. Millot, S. Brygoo, R.S. McWilliams, Dayne E. Fratanduono, J. R. Rygg, Alexander F. Goncharov, P. Loubeyre, J. H. Eggert, J. L. Peterson, N. B. Meezan, S. Le Pape, G. W. Collins, R. Jeanloz, and R. J. Hemley. Insulator-Metal Transition in Dense Fluid Deuterium. *Science*, 361(6403):677–682, 2018. https://science.sciencemag.org/content/361/6403/677.full.pdf.

[72] O. S. Kushnir, P. A. Shchepanskyi, V. Yo. Stadnyk, and A. O. Fedorchuk. Relationships Among Optical and Structural Characteristics of $ABSO_4$ Crystals. *Optical Materials*, 95:109221, 2019.

[73] S. B. Aziz, A. Q. Hassan, S. J. Mohammed, W. O. Karim, M. F. Z. Kadir, H. A. Tajuddin, and N. N. M. Y. Chan. Structural and Optical Characteristics of PVA:C-Dot Composites: Tuning The Absorption of Ultra Violet (UV) Region. *Nanomaterials*, 9(2), 2019. https://www.mdpi.com/2079-4991/9/2/216.

[74] N. Drissi, N. Bouarissa, and F. Jomni. Optical Properties and Chemical Bonding of 3C-SiC under High-Pressure. *Optik*, 202:163613, 2020. http://www.sciencedirect.com/science/article/pii/S0030402619315116.

[75] D. Mrdjenovich, M. K. Horton, J. H. Montoya, C. M. Legaspi, S. Dwaraknath, V. Tshitoyan, A. Jain, and K. A. Persson. Propnet: A Knowledge Graph for Materials Science. *Matter*, 2(2):464 – 480, 2020.

[76] E. Sharma and P. Sharma. Applicability of Different Models of Energy Bandgap and Refractive Index for Chalcogenide Thin Films. *Materials Today: Proceedings*, 2020. http://www.sciencedirect.com/science/article/pii/S2214785320304417.

[77] D. M. Hoat, M. Naseri, R. Ponce-Pérez, J.F. Rivas-Silva, and G. H. Cocoletzi. First Principles Insight into The Structural, Electronic, Optical and Thermodynamic Properties of $CsPb_2br_5$ Compound. *Chemical Physics*, 533:110704, 2020. http://www.sciencedirect.com/science/article/pii/S0301010419313862.

[78] M. Isik, S. Delice, N. M. Gasanly, N. H. Darvishov, and V. E. Bagiev. Investigation of Optical Properties of $Bi_{12}GeO_{20}$ Sillenite Crystals by Spectroscopic Ellipsometry and Raman Spectroscopy. *Ceramics International*, 2020.

[79] K. Ueda, H. Yanagi, R. Noshiro, H. Hosono, and H. Kawazoe. Vacuum Ultraviolet Reflectance and Electron Energy Loss Spectra. *Journal of Physics: Condensed Matter*, 10(16):3669–3677, April 1998. https://doi.org/10.1088

[80] S. Manzoor, J. Häusele, K. A. Bush, A. F. Palmstrom, J. Carpenter, Z. J. Yu, S. F. Bent, M. D. Mcgehee, and Z. C. Holman. Optical Modeling of Wide-Bandgap Perovskite and Perovskite/Silicon Tandem Solar Cells Using Complex Refractive Indices for Arbitrary-Bandgap Perovskite Absorbers. *Opt. Express*, 26(21):27441–27460, October 2018. http://www.opticsexpress.org/abstract.cfm?URI=oe-26-21-27441.

[81] L. Phillips, A. Rashed, R. Treharne, J. Kay, P. Yates, I.Z. Mitrovic, A. Weerakkody, S. Hall, and K. Durose. Maximizing The Optical Performance of Planar $CH_3NH_3PbI_3$ Hybrid Perovskite Heterojunction Stacks. *Solar Energy Materials and Solar Cells*, 147:327–333, 12 2015.

[82] A. Nyayban, S. Panda, A. Chowdhury, and B. I. Sharma. First Principle Studies on The Optoelectronic Properties of Rubidium Lead Halides., year=2019, eprint=1909.11419, archiveprefix=arXiv, primaryclass=cond-mat.mtrl-sci.

[83] B. Ezealigo, A. Nwanya, S. Ezugwu, S. Offiah, D. Obi, R. Osuji, R. Bucher, M. Maaza, P. Ejikeme, and F. Ezema. Method to Control The Optical Properties: Band Gap Energy of Mixed Halide Organolead Perovskites. *Arabian Journal of Chemistry*, 13, 09 2017.

[84] M. Nenkov and T. Pencheva. Determination of Thin Film Refractive Index and Thickness by Means of Film Phase Thickness. *Open Physics*, 6:332–343, 06 2008.

[85] M. Ono, S. Aoyama, M. Fujinami, and S. Ito. Significant Suppression of Rayleigh Scattering Loss in Silica Glass Formed by The Compression of its Melted Phase. *Optics Express*, 26:7942, 04 2018.

[86] H. Ong, J. Dai, A. Li, G. Du, R. Chang, and S. Ho. Effect of A Microstructure on The Formation of Self-Assembled Laser Cavities in Polycrystalline ZnO. *Journal of Applied Physics*, 90:1663–1665, 08 2001.

[87] T. S. Moss. Photoconductivity in The Elements. *Proceedings of the Physical Society. Section A*, 64(6):590–591, June 1951.

[88] T. S. Moss. Relations Between The Refractive Index and Energy Gap of Semiconductors. *Physica Status Solidi (b)*, 131(2):415–427, 1985.

[89] R. R. Reddy and Y. N. Ahammed. A Study on The Moss Relation. *Infrared Physics and Technology*, 36(5):825 – 830, 1995.

[90] D. R. Penn. Wave-Number-Dependent Dielectric Function of Semiconductors. *Phys. Rev.*, 128:2093–2097, December 1962.

[91] N. Ravindra, S. Auluck, and V. Srivastava. On The Penn Gap in Semiconductors. *Physica Status Solidi (b)*, 93:K155 – K160, 06 1979.

[92] V. P. Gupta and N. M. Ravindra. Comments on The Moss Formula. *Physica Status Solidi (b)*, 100(2):715–719, 1980.

[93] N. M. Ravindra. Energy Gap-Refractive Index Relation — Some Observations. *Infrared Physics*, 21(5):283 – 285, 1981.

[94] S. K. Tripathy. Refractive Indices of Semiconductors from Energy Gaps. *Optical Materials*, 46:240–246, 2015.

[95] M. Anani, C. Mathieu, A. Hamza, S. Lebid, C. Zouaoui, and Y. Amar. Model for Calculating The Refractive Index of A III-V Semiconductor. *Computational Materials Science*, 41:570–575, 02 2008.

[96] P. Herve and L.K.J. Vandamme. General Relation Between Refractive Index and Energy Gap in Semiconductors. *Infrared Physics and Technology*, 35(4):609 – 615, 1994. http://www.sciencedirect.com/science/article/pii/1350449594900264.

[97] A. Bahadur and M. Mishra. Correlation Between Refractive Index and Electronegativity Difference for ANB8-N Type Binary Semiconductors. *Acta Physica Polonica A*, 123(4):737–740, 4 2013.

[98] S. H. Wemple and M. DiDomenico. Behavior of The Electronic Dielectric Constant in Covalent and Ionic Materials. *Phys. Rev. B*, 3:1338–1351, February 1971. https://link.aps.org/doi/10.1103/PhysRevB.3.1338.

[99] C. Cushman, N. Smith, M. Kaykhaii, N. Podraza, and M. Linford. An Introduction to Modeling in Spectroscopic Ellipsometry, Focusing on Models for Transparent Materials: The Cauchy and Sellmeier Models. *Vacuum Technology & Coating*, 07 2016.

[100] V. Brückner. To The Use of Sellmeier Formula. `https://www.researchgate.net/publication/262294649_To_the_use_of_Sellmeier_formula`, 05 2014.

[101] F. Wooten. *Optical Properties of Solids*. Academic Press, 1972.

[102] S. Batsanov, E. Ruchkin, and I. Poroshina. *Refractive Indices of Solids*. 01 2016.

[103] C. Koughia, S. Kasap, and P. Capper. *Springer Handbook of Electronic and Photonic Materials*. Springer-Verlag, Berlin, Heidelberg, 2007.

[104] A.M. Efimov. *Optical Constants of Inorganic Glasses*. Laser & Optical Science & Technology. Taylor & Francis, 1995.

[105] A. Walsh. Principles of Chemical Bonding and Band Gap Engineering in Hybrid Organic-Inorganic Halide Perovskites. *The Journal of Physical Chemistry C*, 119:57555760, 02 2015.

[106] J.-H. Lee, N. C. Bristowe, J. H. Lee, S.-H. Lee, P. D. Bristowe, A. K. Cheetham, and H. M. Jang. Resolving The Physical Origin of Octahedral Tilting in Halide Perovskites. *Chemistry of Materials*, 28(12):4259–4266, 2016.

[107] R. J. D. Tilley. Perovskites: Structure–Property Relationships : Wiley, 2016 400 pages, isbn 978-1-118-93566-8. *MRS Bulletin*, 42(4):325–325, 2017.

[108] J. George, D. Waroquiers, D. D. Stefano, G. Petretto, G.-M. Rignanese, and G. Hautier. The Limited Predictive Power of The Pauling Rules. 8 2019. https://chemrxiv.org/articles/The_Limited_Predictive_Power_of_the_Pauling_Rules/9255446.

[109] R.L. Moreira and A. Dias. Comment on "Prediction of Lattice Constant in Cubic Perovskites". *Journal of Physics and Chemistry of Solids*, 68(8):1617 – 1622, 2007. http://www.sciencedirect.com/science/article/pii/S0022369707001850.

[110] Pa. Granger, V.I. Parvulescu, S. Kaliaguine, and W. Prellier. *Perovskites and Related Mixed Oxides: Concepts and Applications*. 11 2015.

[111] A. Cammarata and J. M. Rondinelli. Covalent Dependence of Octahedral Rotations in Orthorhombic Perovskite Oxides. *The Journal of Chemical Physics*, 141(11):114704, 2014. https://doi.org/10.1063/1.4895967.

[112] S. Körbel, M. A. L. Marques, and S. Botti. Stability and Electronic Properties of New Inorganic Perovskites from High-Throughput Ab Initio Calculations. *J. Mater. Chem. C*, 4:3157–3167, 2016. http://dx.doi.org/10.1039/C5TC04172D.

[113] A. Garza and G. Scuseria. Predicting Band Gaps with Hybrid Density Functionals. *The Journal of Physical Chemistry Letters*, 7, 08 2016.

[114] M. J. Weber. *Handbook of Optical Materials, Boca Raton: CRC Press*. 2003.

[115] Y. Zhang, M. Sahoo, and J. Wang. Tuning The Band Gap and Polarization in $BaSnO_3/SrSnO_3$ Superlattices for Photovoltaic Applications. *Phys. Chem. Chem. Phys.*, 19, 02 2017.

[116] T. Schumann, S. Raghavan, K. Ahadi, H. Kim, and S. Stemmer. Structure and Optical Band Gaps of $(Ba,Sr)SnO_3$ Films Grown by Molecular Beam Epitaxy. *Journal of Vacuum Science & Technology A: Vacuum, Surfaces, and Films*, 34:050601, 09 2016.

[117] S. Ono, O. Riadh, A. Quema, H. Murakami, N. Sarukura, T. Nishimatsu, N. Terakubo, H. Mizuseki, Y. Kawazoe, A. Yoshikawa, and T. Fukuda. Band-Structure Design of Fluoride Complex Materials for Deep-Ultraviolet Light-Emitting Diodes. *Japanese Journal of Applied Physics*, 44:7285–7290, 10 2005.

[118] A. P. Sakhya, J. Maibam, S. Saha, S. Chanda, A. Dutta, B. I. Sharma, R. K. Thapa, and T. P. Sinha. Electronic Structure and Elastic Properties of $ATiO_3$ $(A = Ba,Sr,Ca)$ Perovskites: A First Principles Study. *IJPAP*, 53(2):102–109, February 2015. http://hdl.handle.net/123456789/30513.

[119] M. Rizwan, Z. Usman, M. Shakil, S. S. A. Gillani, S. Azeem, H. B. Jin, C. B. Cao, R. F. Mehmood, G. Nabi, and M. A. Asghar. Electronic and Optical Behaviour of Lanthanum Doped $CaTiO_3$ Perovskite. *Materials Research Express*, 7(1):015920, January 2020. https://doi.org/10.1088%2F2053-1591%2Fab6802.

[120] S. Piskunov, E. Heifets, R.I. Eglitis, and G. Borstel. Bulk Properties and Electronic Structure of $SrTiO_3$, $BaTiO_3$, $PbTiO_3$ Perovskites: An Ab Initio HF/DFT Study. *Computational Materials Science*, 29(2):165 – 178, 2004. http://www.sciencedirect.com/science/article/pii/S0927025603001812.

[121] M. Bass, Optical Society of America Staff, Optical Society of America, E.W. Van Stryland, W.L. Wolfe, and D.R. Williams. *Handbook of Optics: Devices, Measurements, and Properties*. Handbook of Optics. McGraw-Hill, 1995. https://books.google.com/books?id=owg6AQAAIAAJ.

[122] G. Murtaza, I. Ahmad, M. Maqbool, H. A. R. Aliabad, and A. Afaq. Structural and Optoelectronic Properties of Cubic $CsPbF_3$ for novel applications. *Chinese Physics Letters*, 28(11):117803, November 2011. https://doi.org/10.1088%2F0256-307x%2F28%2F11%2F117803.

[123] R. K. Singh, R. Kumar, N. Jain, S. R. Dash, J. Singh, and A. Srivastava. Investigation of Optical and Dielectric Properties of $CsPbI_3$ Inorganic Lead Iodide Perovskite Thin Film. *Journal of the Taiwan Institute of Chemical Engineers*, 96:538 – 542, 2019. http://www.sciencedirect.com/science/article/pii/S1876107018306059.

[124] G. E. Jellison, I. Paulauskas, L. A. Boatner, and D. J. Singh. Optical Functions of $KTaO_3$ as Determined by Spectroscopic Ellipsometry and Comparison with Band Structure Calculations. *Phys. Rev. B*, 74:155130, October 2006. https://link.aps.org/doi/10.1103/PhysRevB.74.155130.

[125] Y. Yuan, R. Xu, H.-T. Xu, F. Hong, F. Xu, and L. Wang. Nature of The Band Gap of Halide Perovskites ABX_3 ($A = CH_3NH_3, Cs$; $B = Sn, Pb$; $X = Cl, Br, I$): First-Principles Calculations. *Chinese Physics B*, 24:116302, 11 2015.

[126] D. Dirin, I. Cherniukh, S. Yakunin, Y. Shynkarenko, and M. Kovalenko. Solution-Grown $CsPbBr_3$ Perovskite Single Crystals for Photon Detection. *Chemistry of Materials*, 28, 11 2016.

[127] Mineralogy Database. http://webmineral.com/data/Perovskite.shtml.XraySG5NKjOR (Accessed on 2020-03-14).

[128] R. Estrada, N. Djohan, D. Pasole, M. Dahrul, A. Kurniawan, J. Iskandar, H. Hardhienata, and Irzaman. The Optical Band Gap of $LiTaO_3$ and Nb_2o_5-Doped $LiTaO_3$ thin films based on tauc plot method to be applied on satellite. *IOP Conference Series: Earth and Environmental Science*, 54:012092, January 2017. https://doi.org/10.1088%2F1755-1315%2F54%2F1%2F012092.

[129] G. Pilania, K. McClellan, C. Stanek, and B. Uberuaga. Physics-Informed Machine Learning for Inorganic Scintillator Discovery. *The Journal of Chemical Physics*, 148, 04 2018.

[130] L. S. Kouchaksaraie. Theoretical Calculation of Electrical and Optical Properties of $BaZrO_3$. *International Journal of Physical and Mathematical Sciences*, 5(11):1680 – 1683, 2011. https://publications.waset.org/vol/59.

[131] Mineralogy Database. http://www.webmineral.com/data/Lakargiite.shtm1#.XbRoEugzbIU (Accessed on 2020-03-14).

[132] K. E. Babu, N. Murali, K. Babu, B. Babu, and V. Veeraiah. Structural, Electronic and Elastic Properties of $KCaF_3$ and $RbCaF_3$ for Vacuum Ultraviolet- Transparent Lens Materials. volume 1661, 05 2015.

[133] S. Hiadsi, H. Bouafia, B. Sahli, B. Abidri, A. Bouaza, and A. Akriche. Structural, Mechanical, Electronic and Thermal Properties of $KZnF_3$ and $AgZnF_3$ Perovskites: FP-(L)APW+lo Calculations. *Solid State Sciences*, 58:1 – 13, 2016. http://www.sciencedirect.com/science/article/pii/S129325581630293X.

[134] S. Ehsan, A. Tröster, F. Tran, and P. Blaha. Dft Study of The Electronic Properties and The Cubic to Tetragonal Phase Transition in $RbCaF_3$. *Physical Review Materials*, 2, 09 2018.

[135] A. Mousa, J. Khalifeh, N. Mahmoud, and H. Juwhari. First Principles Study of Structural, Electronic and Optical Properties of The Fluoroperovskite $RbCaF_3$ Crystal. *American Journal of Condensed Matter Physics*, 3:151–162, 11 2013.

[136] M. Lal and S. Kapila. Structural, Electronic, Optical and Mechanical Properties of $CsCaCl_3$ and $KCdF_3$ Cubic Perovskites. *International Journal of Materials Science*, 12(1):137–147, 2017.

[137] K. Takegahara. Electronic Band Structures in Cubic Perovskite-Type Oxides: Bismuthates and Transition Metal Oxides. *Journal of Electron Spectroscopy and Related Phenomena*, 66(3):303 – 320, 1994.

[138] L. D. Whalley, J. M. Frost, Y.-K. Jung, and A. Walsh. Perspective: Theory and Simulation of Hybrid Halide Perovskites. *The Journal of Chemical Physics*, 146(22):220901, 2017. https://doi.org/10.1063/1.4984964.

[139] M. A. Green, Y. Jiang, A. M. Soufiani, and A. Ho-Baillie. Optical Properties of Photovoltaic Organic–Inorganic Lead Halide Perovskites. *The Journal of Physical Chemistry Letters*, 6(23):4774–4785, 2015.

[140] L. Q. Jiang, J. K. Guo, H. B. Liu, M. Zhu, X. Zhou, P. Wu, and C. H. Li. Prediction of Lattice Constant in Cubic Perovskites. *Journal of Physics and Chemistry of Solids*, 67(7):1531 – 1536, 2006.

[141] M. N. Polyanskiy. Refractive Index Database. `https://refractiveindex.info`. Accessed on 2020-03-13.

[142] V. Lingwal, A. S. Kandari, and N. S. Panwar. Optical Properties of Sodium Niobate Thin Films. *Nanosystems: Physics, Chemistry, Mathematics*, pages 583–591, 08 2016.

[143] T. Jia, Z. Zeng, H. Q. Lin, Y. Duan, and P. Ohodnicki. First-Principles Study on The Electronic, Optical and Thermodynamic Properties of ABO_3 (A = La, Sr, B = Fe, Co) *P*erovskites. *RSC Adv.*, 7:38798–38804, 2017.

[144] R. P. Lobo and F. Gervais. Bismuth Disproportionation in babio$_3$ Studied by Infrared and Visible Reflectance Spectra. *Phys. Rev. B*, 52:13294–13299, November 1995. https://link.aps.org/doi/10.1103/PhysRevB.52.13294.

[145] G. Nazir, S. Tariq, A. Afaq, Q. Mahmood, S. Saad, A. Mahmood, and S. Tariq. Under Pressure DFT Investigations on Optical and Electronic Properties of $PbZrO_3$. *Acta Physica Polonica A*, 133:105–113, 01 2018.

[146] L. Guan, B. Liu, L. Jin, J. Guo, Q. Zhao, Y. Wang, and G. Fu. Electronic Structure and Optical Properties of $LaNiO_3$: First Principles Calculations. *Solid State Communications - Solid State Commun*, 150:2011–2014, 11 2010.

[147] S. Çabuk and S. Simsek. First-Principles Studies of The Electronic Structure and Optical Properties of $AgBO_3(B = Nb, Ta)$ in The Paraelectric Phase. *Open Physics*, 6:730–736, 09 2008.

[148] N. Soltani, S. Hosseini, and A. Kompany. Nanoscale Ab-Initio Calculations of Optical and Electronic Properties of $LaCrO_3$ in Cubic and Rhombohedral Phases. *Physica B-condensed Matter - Physica B*, 404:4007–4014, 11 2009.

[149] Hayatullah, G. Murtaza, S. Muhammad, S. Naeem, M.N. Khalid, and M. Ali. Physical Properties of $CsSnM_3$ $(M = Cl, Br, I)$: A First Principle Study. *Acta Physica Polonica A*, 124:102–107, 07 2013.

[150] A. A. Mubarak. The Elastic, Electronic and Optical Properties of $RbCaX_3$ ($X = F, Cl$) Compounds. *International Journal of Modern Physics B*, 28:1450192, 11 2014.

[151] L.-C. Tang, J. Huang, C. Chang, M.-H. Lee, and L. Liu. New Infrared Nonlinear Optical Crystal $CsGeBr_3$: Synthesis, Structure and Powder Second-Harmonic Generation Properties. *J. Phys.: Condens. Matter J. Phys.: Condens. Matter*, 17:217–7275, 11 2005.

[152] B. Bouadjemi, S. Bentata, A. Abbad, W. Benstaali, and B. Bouhafs. Half-Metallic Ferromagnetism in $PrMnO_3$ Perovskite from First Principles Calculations. *Solid State Communications*, 168:6 – 10, 2013.

[153] M. Oumertem, D. Maouche, S. Berri, N. Bouarissa, D. P. Rai, R. Khenata, and M. Ibrir. Theoretical Investigation of the Structural, Electronic and Thermodynamic Properties of Cubic and Orthorhombic $XZrS_3$ $(X = Ba, Sr, Ca)$ compounds. *J. Comput. Electron.*, 18(2):415–427, June 2019. https://doi.org/10.1007/s10825-019-01317-3.

[154] H. Iwahara. Proton Conducting Ceramics and Their Applications. *Solid State Ionics*, 86-88:9 – 15, 1996. https://doi.org/10.1016/0167-2738(96)00087-2.

[155] T. Yajima, K. Koide, H. Takai, N. Fukatsu, and H. Iwahara. Application of Hydrogen Sensor using Proton Conductive Ceramics as a Solid Electrolyte to Aluminum Casting Industries. *Solid State Ionics*, 79:333 – 337, 1995. http://www.sciencedirect.com/science/article/pii/016727389500083I.

[156] R. Terki, H. I. Faraoun, G. Bertrand, and H. Aourag. Full Potential Calculation of Structural, Elastic and Electronic Properties of $BaZrO_3$ and $SrZrO_3$. *Physica Status Solidi (b)*, 242:1054 – 1062, 04 2005.

[157] S. M. Alay-e Abbas, S. Nazir, S. Cottenier, and A. Shaukat. Evaluation of Thermodynamics, Formation Energetics and Electronic Properties of Vacancy Defects in $CaZrO_3$. *Scientific Reports*, 7, 12 2017.

[158] S. S. Pandit, A. Weyl, and D. Janke. High-Temperature Ionic and Electronic Conduction in Zirconate and Hafnate Compounds. *Solid State Ionics*, 69(2):93 – 99, 1994.

[159] J. P. Perdew, K. Burke, and Y. Wang. Generalized Gradient Approximation for The Exchange-Correlation Hole of a Many-Electron System. *Phys. Rev. B*, 54:16533–16539, Dec 1996.

[160] Z. F. Hou. Ab Initio Calculations of Elastic Modulus and Electronic Structures of Cubic $CaZrO_3$. *Physica B: Condensed Matter*, 403(17):2624 – 2628, 2008. http://www.sciencedirect.com/science/article/pii/S0921452608000446.

[161] P. Stoch, J. Szczerba, J. Lis, D. Madej, and Z. Pedzich. Crystal Structure and Ab Initio Calculations of $CaZrO_3$. *Journal of the European Ceramic Society*, 32(3):665 – 670, 2012. http://www.sciencedirect.com/science/article/pii/S0955221911005073.

[162] A. M. Shawahni, M. S. Abu-Jafar, R. T. Jaradat, T. Ouahrani, R. Khenata, A. A. Mousa, and K. F. Ilaiwi. Structural, Elastic, Electronic and Optical Properties of $SrTMO_3(TM = Rh, Zr)$ Compounds: Insights from FP-LAPW Study. *Materials (Basel, Switzerland)*, 11(10):2057, Oct 2018. 30360385[pmid].

[163] F. Tran and P. Blaha. On The Importance of The Kinetic-Energy Density for Band Gap Calculations in Solids with Density Functional Theory. *The Journal of Physical Chemistry A*, 121, 04 2017.

[164] P. Borlido, T. Aull, A. W. Huran, F. Tran, M. A. L. Marques, and S. Botti. Large-Scale Benchmark of Exchange–Correlation Functionals for The Determination of Electronic Band Gaps of Solids. *Journal of Chemical Theory and Computation*, 15(9):5069–5079, 2019. https://doi.org/10.1021/acs.jctc.9b00322.

[165] J. Heyd, G. E. Scuseria, and M. Ernzerhof. Hybrid Functionals Based on A Screened Coulomb Potential. *The Journal of Chemical Physics*, 118(18):8207–8215, 2003. https://doi.org/10.1063/1.1564060.

[166] G.-X. Zhang, A. M. Reilly, A. Tkatchenko, and M. Scheffler. Performance of Various Density-Functional Approximations for Cohesive Properties of 64 Bulk Solids. *New Journal of Physics*, 20(6):063020, jun 2018.

[167] C. A. Guido, E. Brémond, C. Adamo, and P. Cortona. Communication: One Third: A New Recipe for The PBE0 Paradigm. *The Journal of Chemical Physics*, 138(2):021104, 2013. https://doi.org/10.1063/1.4775591.

[168] A. D. Becke. Density-Functional Thermochemistry. IV. A New Dynamical Correlation Functional and Implications for Exact-Exchange Mixing. *The Journal of Chemical Physics*, 104(3):1040–1046, 1996. https://doi.org/10.1063/1.470829.

[169] F. Viñes, O. Lamiel-García, K. Chul Ko, J. Yong Lee, and F. Illas. Systematic Study of The Effect of HSE Functional Internal Parameters on the Electronic Structure and Band Gap of A Representative Set of Metal Oxides. *Journal of Computational Chemistry*, 38(11):781–789, 2017. https://onlinelibrary.wiley.com/doi/abs/10.1002/jcc.24744.

[170] J. P. Perdew, A. Ruzsinszky, G. I. Csonka, O. A. Vydrov, G. E. Scuseria, L. A. Constantin, X. Zhou, and K. Burke. Restoring The Density-Gradient Expansion for Exchange in Solids and Surfaces. *Physical Review Letters*, 100(13), April 2008. http://dx.doi.org/10.1103/PhysRevLett.100.136406.

[171] H. Bouafia, S. Hiadsi, B. Abidri, A. Akriche, L. Ghalouci, and B. Sahli. Structural, Elastic, Electronic and Thermodynamic Properties of $KTaO_3$ and $NaTaO_3$: Ab Initio Investigations. *Computational Materials Science*, 75:1–8, 07 2013.

[172] P. E. Blöchl. Projector Augmented-Wave Method. *Phys. Rev. B*, 50:17953–17979, December 1994. https://link.aps.org/doi/10.1103/PhysRevB.50.17953.

[173] G. Kresse and D. Joubert. From Ultrasoft Pseudopotentials to The Projector Augmented-Wave Method. *Phys. Rev. B*, 59:1758–1775, January 1999. https://link.aps.org/doi/10.1103/PhysRevB.59.1758.

[174] R. W. G. Wyckoff. Crystal Structures, 2nd Edition, Vol. 2. *Interscience Publishers NewYork*, pages 390–395, 1964.

[175] A. J. Smith and A. J. E. Welch. Some Mixed Metal Oxides of Perovskite Structure. *Acta Crystallographica*, 13(8):653–656, August 1960. https://doi.org/10.1107/S0365110X60001540.

[176] A. R. Akbarzadeh, I. Kornev, C. Malibert, L. Bellaiche, and J. M. Kiat. Combined Theoretical and Experimental Study of The Low-Temperature Properties of $BaZrO_3$. *Phys. Rev. B*, 72:205104, November 2005. https://link.aps.org/doi/10.1103/PhysRevB.72.205104.

[177] M. Noh, S. Choi, D. Lee, M. Cho, C. Jeon, and Y. Lee*. Structural and Optical Properties of $AZrO_3$ and $AHfO_3(A = Ca, Sr, and Ba)$. *The Origin of New Physics: Sae Mulli*, 63(8):939–944, August 2013. https://doi.org/10.3938/NPSM.63.939.

[178] A. Togo and I. Tanaka. First Principles Phonon Calculations in Materials Science. *Scr. Mater.*, 108:1–5, November 2015.

[179] X. Gonze and C. Lee. Dynamical Matrices, Born Effective Charges, Dielectric Permittivity Tensors, and Interatomic Force Constants from Density-Functional Perturbation Theory. *Phys. Rev. B*, 55:10355–10368, April 1997. https://link.aps.org/doi/10.1103/PhysRevB.55.10355.

[180] K. Parlinski, Z.Q. Li, and Y. Kawazoe. First-Principles Determination of The Soft Mode in Cubic ZrO_2. *Physical Review Letters*, 78(21):4063–4066, 1997.

[181] C. Toulouse, D. Amoroso, C. Xin, P. Veber, M. C. Hatnean, G. Balakrishnan, M. Maglione, P. Ghosez, J. Kreisel, and M. Guennou. Lattice Dynamics and Raman Spectrum of $BaZrO_3$ Single Crystals. *Phys. Rev. B*, 100:134102, October 2019. https://link.aps.org/doi/10.1103/PhysRevB.100.134102.

[182] J. G. Berryman. Poroelastic Shear Modulus Dependence on Pore-Fluid Properties Arising in A Model of Thin Isotropic Layers. *Geophysical Journal International*, 157(1):415–425, 04 2004. https://doi.org/10.1111/j.1365-246X.2004.02184.x.

[183] C.-S. Man and M. Huang. A Simple Explicit Formula for the Voigt-Reuss-Hill Average of Elastic Polycrystals with Arbitrary Crystal and Texture Symmetries. *Journal of Elasticity*, 105(1):29–48, November 2011.

[184] Z.-J. Wu, E.-J. Zhao, H.-P. Xiang, X.-F. Hao, X.-J. Liu, and J. M. Crystal Structures and Elastic Properties of Superhard IrN_2 and IrN_3 from First Principles. *Phys. Rev. B*, 76:054115, August 2007. https://link.aps.org/doi/10.1103/PhysRevB.76.054115.

[185] M. A. Rahman, M. Z. Rahaman, and M. A. Rahman. The Structural, Elastic, Electronic and Optical Properties of *MgCu* under Pressure: A First-Principles Study. *International Journal of Modern Physics B*, 30(27):1650199, October 2016. http://dx.doi.org/10.1142/S021797921650199X.

[186] X.-Q. Chen, H. Niu, D. Li, and Y. Li. Modeling Hardness of Polycrystalline Materials and Bulk Metallic Glasses. *Intermetallics*, 19(9):1275 – 1281, 2011. http://www.sciencedirect.com/science/article/pii/S0966979511000987.

[187] S. Ranganathan and M. Ostoja-Starzewski. Universal Elastic Anisotropy Index. *Physical review letters*, 101:055504, 09 2008.

[188] X. Liu and H. Fan. Electronic Structure, Elasticity, Debye Temperature and Anisotropy of Cubic WO_3 from First-Principles Calculation. *Royal Society Open Science*, 5:171921, 06 2018.

[189] F. Mouhat and F.-X. Coudert. Necessary and Sufficient Elastic Stability Conditions in Various Crystal Systems. *Physical Review B*, 90(22), December 2014. http://dx.doi.org/10.1103/PhysRevB.90.224104.

[190] G. Wang, S. Schönecker, S. Hertzman, Q.-M. Hu, B. Johansson, S. Kwon, and L. Vitos. Ab Initio Prediction of The Mechanical Properties of Alloys: The Case of Ni/Mn-Doped Ferromagnetic Fe. *Phys. Rev. B*, 91:224203, June 2015. https://link.aps.org/doi/10.1103/PhysRevB.91.224203.

[191] H. Niu, X.-Q. Chen, P. Liu, W. Xing, X. Cheng, D. Li, and Y. Li. Extra-Electron Induced Covalent Strengthening and Generalization of Intrinsic Ductile-to-Brittle Criterion. *Scientific reports*, 2:718, 10 2012.

[192] D. de Ligny and P. Richet. High-Temperature Heat Capacity and Thermal Expansion of $SrTiO_3$ and $SrZrO_3$ Perovskites. *Phys. Rev. B*, 53:3013–3022, Febuary 1996. https://link.aps.org/doi/10.1103/PhysRevB.53.3013.

[193] M. L. Ali and M. Rahaman. Variation of The Physical Properties of Four Transition Metal Oxides $SrTMO_3$ ($TM = Rh, Ti, Mo, Zr$) Under Pressure: An Ab Initio Study. *Journal of Advanced Physics*, 6:197–205(9), 06 2017.

[194] S. Yamanaka, M. Fujikane, T. Hamaguchi, H. Muta, T. Oyama, T. Matsuda, S. Kobayashi, and K. Kurosaki. Thermophysical Properties of $BaZrO_3$ and $BaCeO_3$. *Journal of Alloys and Compounds*, 359(1):109 – 113, 2003.

[195] X. Yang, Y. Wang, Q. Song, Y. Chen, and Y. Xue. Pressure Effects on Structural, Electronic, Elastic, and Optical Properties of Cubic and Tetragonal Phases of $BaZrO_3$. *Acta Physica Polonica A*, 133:1138–1143, 05 2018.

[196] I. L. V. Rosa, M. C. Oliveira, M. Assis, M. Ferrer, R. S. André, E. Longo, and M. F. C. Gurgel. A Theoretical Investigation of The Structural and Electronic Properties of Orthorhombic $CaZrO_3$. *Ceramics International*, 41(2, Part B):3069 – 3074, 2015. https://doi.org/10.1016/j.ceramint.2014.10.149.

[197] Y. S. Lee, J. S. Lee, T. W. Noh, Douck Young Byun, Kwang Soo Yoo, K. Yamaura, and E. Takayama-Muromachi. Systematic Trends in The Electronic Structure Parameters of The 4*d* Transition-Metal Oxides $SrMO_3(M = Zr, Mo, Ru, Rh)$. *Phys. Rev. B*, 67:113101, March 2003.

[198] J. Robertson. Band Offsets of Wide-Band-Gap Oxides and Implications for Future Electronic Devices. *Journal of Vacuum Science & Technology B: Microelectronics and Nanometer Structures Processing, Measurement, and Phenomena*, 18(3):1785–1791, 2000. https://avs.scitation.org/doi/abs/10.1116/1.591472.

[199] A. Roy, S. Mukherjee, R. Gupta, S. Auluck, R. Prasad, and A. Garg. Electronic Structure, Born Effective Charges and Spontaneous Polarization in Magnetoelectric Gallium Ferrite. *Journal of Physics: Condensed Matter*, 23(32):325902, July 2011. https://doi.org/10.1088

[200] J. C. Phillips. Ionicity of the Chemical Bond in Crystals. *Rev. Mod. Phys.*, 42:317–356, July 1970. https://link.aps.org/doi/10.1103/RevModPhys.42.317.

[201] S. H. Wemple. Effective Charges and Ionicity. *Phys. Rev. B*, 7:4007–4009, April 1973. https://link.aps.org/doi/10.1103/PhysRevB.7.4007.

[202] K. Fajans. Struktur und Deformation der Elektronenhüllen in ihrer Bedeutung für die chemischen und optischen Eigenschaften anorganischer Verbindungen. *Naturwissenschaften*, 11(10):165–172, March 1923.

[203] D. M. Hoat, J. F. Rivas Silva, and A. Méndez Blas. First Principles Study of Structural, Electronic and Optical Properties of Perovskites $CaZrO_3$ and $CaHfO_3$ in Cubic Phase. *Solid State Communications*, 275:29 – 34, 2018.

[204] M. P. Prange, J. J. Rehr, G. Rivas, J. J. Kas, and J. W. Lawson. Real Space Calculation of Optical Constants from Optical to X-Ray Frequencies. *Physical Review B*, 80(15), October 2009.

[205] D. J. Cirilo-Lombardo. Semiconductor Dielectric Function, Excitons and The Penn Model. *Philosophical Magazine*, 95(9):1007–1015, February 2015.

[206] Y. H. Duan and Y. Sun. First-Principles Calculations of Optical Properties of Mg_2Pb. *Science China Physics, Mechanics and Astronomy*, 57:233–238, 02 2013.

[207] S. Karazhanov, P. Ravindran, A. Kjekshus, H. Fjellvåg, and B. Svensson. Electronic Structure and Optical Properties of ZnX (X= O, S, Se, Te): A Density Functional Study. *Phys. Rev. B*, 75, 05 2007.

[208] R. John and S. V. Padmavathi. Ab Initio Calculations on Structural, Electronic and Optical Properties of *ZnO* in Wurtzite Phase. *Crystal structure theory and applications*, 5:24–41, 2016.

[209] S. Pitchaiya, N. Eswaramoorthy, M. Natarajan, A. Santhanam, V. Asokan, V. Madurai Ramakrishnan, B. Rangasamy, S. Sundaram, P. Ravirajan, and D. Velauthapillai. Perovskite Solar Cells: A Porous Graphitic Carbon based Hole Transporter/Counter Electrode Material Extracted from An Invasive Plant Species Eichhornia Crassipes. *Scientific Reports*, 10(1):6835, April 2020.

[210] A.B. Djurišić, F.Z. Liu, H.W. Tam, M.K. Wong, A. Ng, C. Surya, W. Chen, and Z.B. He. Perovskite Solar Cells - An Overview of Critical Issues. *Progress in Quantum Electronics*, 53:1 – 37, 2017.

[211] L. Meng, J. You, and Y. Yang. Addressing The Stability Issue of Perovskite Solar Cells for Commercial Applications. *Nature Communications*, 9(1):5265, Dec 2018.

[212] Y. Rong, Y. Hu, A. Mei, H. Tan, M. I. Saidaminov, S. I. Seok, M. D. McGehee, E. H. Sargent, and H. Han. Challenges for Commercializing Perovskite Solar Cells. *Science*, 361(6408), 2018.

[213] C. Quarti, E. Mosconi, and F. De Angelis. Interplay of Orientational Order and Electronic Structure in Methylammonium Lead Iodide: Implications for Solar Cell Operation. *Chemistry of Materials*, 26(22):6557–6569, November 2014.

[214] J. H. Noh, I. S. Hyuk, H. J. Hyuck, M. Tarak N., and S. S. Il. Chemical Management for Colorful, Efficient, and Stable Inorganic–Organic Hybrid Nanostructured Solar Cells. *Nano Letters*, 13(4):1764–1769, April 2013.

[215] T. Ava, A. Mamun, S. Marsillac, and G. Namkoong. A Review: Thermal Stability of Methylammonium Lead Halide Based Perovskite Solar Cells. *Applied Sciences*, 9:188, 01 2019.

[216] A. F. Akbulatov, L. A. Frolova, N. N. Dremova, I. Zhidkov, V. M. Martynenko, S. A. Tsarev, S. Y. Luchkin, E. Z. Kurmaev, S. M. Aldoshin, K. J. Stevenson, and P. A. Troshin. Light or Heat: What Is Killing Lead Halide Perovskites under Solar Cell Operation Conditions? *The Journal of Physical Chemistry Letters*, 11(1):333–339, January 2020.

[217] S. Zou and F. Li. Efficient All-Inorganic $CsPbBr_3$ Perovskite Solar Cells by Using CdS/CdSe/CdS Quantum Dots as Intermediate Layers. *Journal of Nanomaterials*, 2020:7946853, May 2020.

[218] M. Konstantakou and T. Stergiopoulos. A Critical Review on Tin Halide Perovskite Solar Cells. *J. Mater. Chem. A*, 5:11518–11549, 2017.

[219] P. Boix, S. Agarwala, T. M. Koh, N. Mathews, and S. Mhaisalkar. Perovskite Solar Cells: Beyond Methylammonium Lead Iodide. *The Journal of Physical Chemistry Letters*, 6:150213091342008, 02 2015.

[220] Z. Shi, J. Guo, Y. Chen, Q. Li, Y. Pan, H. Zhang, Y. Xia, and W. Huang. Lead-Free Organic–Inorganic Hybrid Perovskites for Photovoltaic Applications: Recent Advances and Perspectives. *Advanced Materials*, 29(16):1605005, 2017.

[221] L. Serrano-Luján, N. Espinosa, T. Trofod, J. Abad, A. Urbina, and F. Krebs. Tin- and Lead-Based Perovskite Solar Cells under Scrutiny: An Environmental Perspective. *Advanced Energy Materials*, pages n/a–n/a, 09 2015.

[222] F. Gao, C. Li, L. Qin, L. Zhu, X. Huang, H. Liu, L. Liang, Y. Hou, Z. Lou, Y. Hu, and F. Teng. Enhanced Performance of Tin Halide Perovskite Solar Cell by Addition of Lead Thiocyanate. *RSC Adv.*, 8:14025–14030, 2018.

[223] P. Billen, E. Leccisi, S. Dastidar, S. Li, L. Lobaton, S. Spatari, A. T. Fafarman, V. M. Fthenakis, and J. B. Baxter. Comparative Evaluation of Lead Emissions and Toxicity Potential in The Life Cycle of Lead Halide Perovskite Photovoltaics. *Energy*, 166:1089 – 1096, 2019.

[224] S. A. U. Hasan, D. S. Lee, S. H. Im, and K.-H. Hong. Present Status and Research Prospects of Tin-based Perovskite Solar Cells. *Solar RRL*, 4(2):1900310, 2020.

[225] X. Li, Y. Tan, H. Lai, S. Li, Y. Chen, S. Li, P. Xu, and J. Yang. All-Inorganic $CsPbBr_3$ Perovskite Solar Cells with 10.45% Efficiency by Evaporation-Assisted Deposition and Setting Intermediate Energy Levels. *ACS Applied Materials & Interfaces*, 11(33):29746–29752, August 2019.

[226] J. Li, R. Gao, F. Gao, J. Lei, H. Wang, X. Wu, J. Li, H. Liu, X. Hua, and S. (Frank) Liu. Fabrication of Efficient $CsPbBr_3$ Perovskite Solar Cells by Single-Source Thermal Evaporation. *Journal of Alloys and Compounds*, 818:152903, 2020.

[227] J. Zeng, H. Zhou, R. Liu, and H. Wang. Combination of Solution-Phase Process and Halide Exchange for All-Inorganic, Highly Stable $CsPbBr_3$ Perovskite Nanowire Photodetector. *Science China Materials*, 62(1):65–73, January 2019.

[228] T. Niu, H. Ren, B. Wu, Y. Xia, X. Xie, Y. Yang, X. Gao, Y. Chen, and W. Huang. Reduced-Dimensional Perovskite Enabled by Organic Diamine for Efficient Photovoltaics. *The Journal of Physical Chemistry Letters*, 10(10):2349–2356, May 2019.

[229] Y. Lekina and Z. X. Shen. Excitonic States and Structural Stability in Two-Dimensional Hybrid Organic-Inorganic Perovskites. *Journal of Science: Advanced Materials and Devices*, 4(2):189 – 200, 2019.

[230] D. Marongiu, M. Saba, F. Quochi, A. Mura, and G. Bongiovanni. The Role of Excitons in 3D and 2D Lead Halide Perovskites. *J. Mater. Chem. C*, 7:12006–12018, 2019.

[231] W. Li, J. Ma, X. Cheng, and D. Li. Giant Enhancement of Photoluminescence Quantum Yield in 2D Perovskite Thin Microplates by Graphene Encapsulation. *Nano Research*, July 2020.

[232] S. N. Ruddlesden and P. Popper. New Compounds of The K_2NiF_4 Type. *Acta Crystallographica*, 10(8):538–539, 1957.

[233] Y. Yu, D. Zhang, and P. Yang. Ruddlesden–Popper Phase in Two-Dimensional Inorganic Halide Perovskites: A Plausible Model and the Supporting Observations. *Nano Letters*, 17(9):5489–5494, September 2017.

[234] K.-H. Wang, L. Wu, L. Li, H.-B. Yao, H.-S. Qian, and S.-H. Yu. Large-Scale Synthesis of Highly Luminescent Perovskite-Related $CsPb_2Br_5$ Nanoplatelets and Their Fast Anion Exchange. *Angewandte Chemie International Edition*, 55(29):8328–8332, 2016.

[235] X. Zhang, B. Xu, J. Zhang, Y. Gao, Y. Zheng, K. Wang, and X. W. Sun. All-Inorganic Perovskite Nanocrystals for High-Efficiency Light Emitting Diodes: Dual-Phase $CsPbBr_3$-$CsPb_2Br_5$ Composites. *Advanced Functional Materials*, 26(25):4595–4600, 2016.

[236] G. Li, H. Wang, Z. Zhu, Y. Chang, T. Zhang, Z. Song, and Y. Jiang. Shape and Phase Evolution from $CsPbBr_3$ Perovskite Nanocubes to Tetragonal $CsPb_2Br_5$ Nanosheets with An Indirect Bandgap. *Chem. Commun.*, 52:11296–11299, 2016.

[237] J. Li, H. Zhang, S. Wang, D. Long, M. Li, Y. Guo, Z. Zhong, K. Wu, D. Wang, and T. Zhang. Synthesis of All-Inorganic $CsPb_2Br_5$ Perovskite and Determination of Its Luminescence Mechanism. *RSC Adv.*, 7:54002–54007, 2017.

[238] J. P. Perdew, K. Burke, and M. Ernzerhof. Generalized Gradient Approximation Made Simple. *Phys. Rev. Lett.*, 77:3865–3868, Oct 1996.

[239] K. Momma and F. Izumi. *VESTA3* for Three-Dimensional Visualization of Crystal, Volumetric and Morphology Data. *Journal of Applied Crystallography*, 44(6):1272–1276, December 2011.

[240] V. Wang, N. Xu, J. Cheng Liu, G. Tang, and W.-T. Geng. VASPKIT: A User-friendly Interface Facilitating High-Throughput Computing and Analysis Using VASP Code. 2019.

[241] A. Ganose, A. Jackson, and D. Scanlon. Sumo: Command-Line Tools for Plotting and Analysis of Periodic Ab Initio Calculations. *Journal of Open Source Software*, 3:717, 08 2018.

[242] M. Rodová, J. Brožek, K. Knížek, and K. Nitsch. Phase Transitions in Ternary Caesium Lead Bromide. *Journal of Thermal Analysis and Calorimetry*, 71(2):667–673, February 2003.

[243] J. Li, Q. Yu, Y. He, C. C. Stoumpos, G. Niu, G. G. Trimarchi, H. Guo, G. Dong, D. Wang, L. Wang, and M. G. Kanatzidis. $Cs_2PbI_2Cl_2$, All-Inorganic Two-Dimensional Ruddlesden–Popper Mixed Halide Perovskite with Optoelectronic Response. *Journal of the American Chemical Society*, 140(35):11085–11090, 2018. PMID: 30081628.

[244] I. Dursun, M. De Bastiani, B. Turedi, B. Alamer, A. Shkurenko, J. Yin, A. M. El-Zohry, I. Gereige, A. AlSaggaf, O. F. Mohammed, M. Eddaoudi, and O. M. Bakr. $CsPb_2Br_5$ Single Crystals: Synthesis and Characterization. *ChemSusChem*, 10(19):3746–3749, 2017.

[245] Q. Meng, Y. Chen, Y. Y. Xiao, J. Sun, X. Zhang, C. B. Han, H. Gao, Y. Zhang, and H. Yan. Effect of Temperature on The Performance of Perovskite Solar Cells. *Journal of Materials Science: Materials in Electronics*, February 2020.

[246] C. M. M. Soe, G. P. Nagabhushana, R. Shivaramaiah, H. Tsai, W. Nie, J.-C. Blancon, F. Melkonyan, D. H. Cao, B. Traoré, L. Pedesseau, M. Kepenekian, C. Katan, J. Even, T. J. Marks, A. Navrotsky, A. D. Mohite, C. C. Stoumpos, and M. G. Kanatzidis. Structural and Thermodynamic Limits of Layer Thickness in 2D Halide Perovskites. *Proceedings of the National Academy of Sciences*, 116(1):58–66, 2019.

[247] S. Hirotsu, J. Harada, M. Iizumi, and K. Gesi. Structural Phase Transitions in $CsPbBr_3$. *Journal of the Physical Society of Japan*, 37(5):1393–1398, 1974.

[248] C. C. Stoumpos, C. D. Malliakas, J. A. Peters, Z. Liu, M. Sebastian, J. Im, T. C. Chasapis, A. C. Wibowo, D. Y. Chung, A. J. Freeman, B. W. Wessels, and M. G. Kanatzidis. Crystal Growth of The Perovskite Semiconductor $CsPbBr_3$: A New Material for High-Energy Radiation Detection. *Crystal Growth & Design*, 13(7):2722–2727, July 2013.

[249] Z.-P. Huang, B. Ma, H. Wang, N. Li, R.-T. Liu, Z.-Q. Zhang, X.-D. Zhang, J.-H. Zhao, P.-Z. Zheng, Q. Wang, and H.-L. Zhang. In Situ Growth of 3D/2D ($CsPbBr_3$/$CsPb_2Br_5$) Perovskite Heterojunctions toward Optoelectronic Devices. *The Journal of Physical Chemistry Letters*, 11(15):6007–6015, August 2020.

[250] J.-H. Yang, Q. Yuan, and B. I. Yakobson. Chemical Trends of Electronic Properties of Two-Dimensional Halide Perovskites and Their Potential Applications for Electronics and Optoelectronics. *The Journal of Physical Chemistry C*, 120(43):24682–24687, November 2016.

[251] Z. Zhang, Y. Zhu, W. Wang, W. Zheng, R. Lin, and F. Huang. Growth, Characterization and Optoelectronic Applications of Pure-Phase Large-Area $CsPb_2Br_5$ Flake Single Crystals. *J. Mater. Chem. C*, 6:446–451, 2018.

[252] S. Sanguinetti, M. Guzzi, and M. Gurioli. 6 - Accessing Structural and Electronic Properties of Semiconductor Nanostructures via Photoluminescence. In Carlo Lamberti, editor, *Characterization of Semiconductor Heterostructures and Nanostructures*, pages 175 – 208. Elsevier, Amsterdam, 2008.

[253] N. Ashari-Astani, S. Meloni, A. H. Salavati, Giulia Palermo, M. Grätzel, and U. Rothlisberger. Computational Characterization of the Dependence of Halide Perovskite Effective Masses on Chemical Composition and Structure. *The Journal of Physical Chemistry C*, 121(43):23886–23895, November 2017.

[254] H. M. Ghaithan, Z. A. Alahmed, S. M. H. Qaid, M. Hezam, and A. S. Aldwayyan. Density Functional Study of Cubic, Tetragonal, and Orthorhombic $CsPbBr_3$ Perovskite. *ACS Omega*, 5(13):7468–7480, 2020.

[255] M. Jin, Z. Li, F. Huang, and W. Wang. Electronic and Optical Properties of $CsPb_2Br_5$: A First-Principles Study. *Modern Physics Letters B*, 33(22):1950266, 2019.

[256] T.-W. Lee. Emerging Halide Perovskite Materials and Devices for Optoelectronics. *Advanced Materials*, 31(47):1905077, 2019.

[257] C. Grote and R. F. Berger. Strain Tuning of Tin–Halide and Lead–Halide Perovskites: A First-Principles Atomic and Electronic Structure Study. *The Journal of Physical Chemistry C*, 119(40):22832–22837, 2015.

[258] U.-G. Jonga, C.-J. Yu, Y.-H. Kye, Y.-G. Choe, H. Wei, and S. Li. Structural and Optoelectronic Properties of The Inorganic Perovskites $AGeX_3$ (A = Cs, Rb; X = I, Br, Cl) for Solar Cell Application, 2018.

[259] S. Meloni, G. Palermo, N. Ashari-Astani, M. Grätzel, and U. Rothlisberger. Valence and Conduction Band Tuning in Halide Perovskites for Solar Cell Applications. *J. Mater. Chem. A*, 4:15997–16002, 2016.

[260] N. Jeon, J. Noh, W. Yang, Y. Kim, S. Ryu, J. Seo, and S. H. Im. Compositional Engineering of Perovskite Materials for High-Performance Solar Cells. *Nature*, 517, 01 2015.

[261] F. Hao, C. C. Stoumpos, R. P. H. Chang, and M. G. Kanatzidis. Anomalous Band Gap Behavior in Mixed Sn and Pb Perovskites Enables Broadening of Absorption Spectrum in Solar Cells. *Journal of the American Chemical Society*, 136(22):8094–8099, 2014. PMID: 24823301.

[262] H. J. Snaith. Perovskites: The Emergence of a New Era for Low-Cost, High-Efficiency Solar Cells. *The Journal of Physical Chemistry Letters*, 4(21):3623–3630, 2013.

[263] V. D'Innocenzo, G. Grancini, M. Alcocer, A. Srimath Kandada, S. Stranks, M. Lee, G. Lanzani, H. Snaith, and A. Petrozza. Excitons Versus Free Charges in Organo-Lead Tri-Halide Perovskites. *Nature communications*, 5:3586, 04 2014.

[264] S. Sun, T. Salim, N. Mathews, M. Duchamp, C. Boothroyd, G. Xing, T. C. Sum, and Y. M. Lam. The Origin of High Efficiency in Low-Temperature Solution-Processable Bilayer Organometal Halide Hybrid Solar Cells. *Energy Environ. Sci.*, 7:399–407, 2014.

[265] J. Bisquert and E. J. Juarez-Perez. The Causes of Degradation of Perovskite Solar Cells. *The Journal of Physical Chemistry Letters*, 10(19):5889–5891, 2019. PMID: 31536358.

[266] D. B. Mitzi. Introduction: Perovskites. *Chemical Reviews*, 119(5):3033–3035, 2019.

[267] Q. Wali, F. J. Iftikhar, M. E. Khan, A. Ullah, Y. Iqbal, and R. Jose. Advances in Stability of Perovskite Solar Cells. *Organic Electronics*, 78:105590, 2020.

[268] D. Wang, M. Wright, N. K. Elumalai, and A. Uddin. Stability of Perovskite Solar Cells. *Solar Energy Materials and Solar Cells*, 147:255 – 275, 2016.

[269] R. Wang, M. Mujahid, Y. Duan, Z.-K. Wang, J. Xue, and Y. Yang. A Review of Perovskites Solar Cell Stability. *Advanced Functional Materials*, 29(47):1808843, 2019.

[270] Q. Zhao, A. Hazarika, L. T. Schelhas, J. Liu, E. A. Gaulding, G. Li, M. Zhang, M. F. Toney, P. C. Sercel, and J. M. Luther. Size-Dependent Lattice Structure and Confinement Properties in $CsPbI_3$ Perovskite Nanocrystals: Negative Surface Energy for Stabilization. *ACS Energy Letters*, 5(1):238–247, 2020.

[271] M. V. Talanov, V. B. Shirokov, and V. M. Talanov. Anion Order in Perovskites: A Group-Theoretical Analysis. *Acta Crystallographica Section A*, 72(2):222–235, March 2016.

[272] G. King and P. M. Woodward. Cation Ordering in Perovskites. *J. Mater. Chem.*, 20:5785–5796, 2010.

[273] F. Wang, M. Tan, C. Li, C. Niu, and X. Zhao. Unusual Pressure-Induced Electronic Structure Evolution in Organometal Halide Perovskite Predicted from First-Principles. *Organic Electronics*, 67:89 – 94, 2019.

[274] N. V. Ter-Oganessian and V. P. Sakhnenko. Effect of Pressure on The Order–Disorder Phase Transitions of B cations in $AB'_1/2B''_1/2O_3$ Perovskites. *Acta Crystallographica Section B*, 75(6):1034–1041, December 2019.

[275] J. Lin, H. Chen, Y. Gao, Y. Cai, J. Jin, A. S. Etman, J. Kang, T. Lei, Z. Lin, M. C. Folgueras, L. N. Quan, Q. Kong, M. Sherburne, M. Asta, J. Sun, M. F. Toney, J. Wu, and P. Yang. Pressure-Induced Semiconductor-to-Metal Phase Transition of A Charge-Ordered Indium Halide Perovskite. *Proceedings of the National Academy of Sciences*, 116(47):23404–23409, 2019.

[276] X. Mao, L. Sun, T. Wu, T. Chu, W. Deng, and K. Han. First-Principles Screening of All-Inorganic Lead-Free ABX_3 Perovskites. *The Journal of Physical Chemistry C*, 122(14):7670–7675, April 2018.

[277] H. Jin, J. Im, and A. J. Freeman. Topological Insulator Phase in Halide Perovskite Structures. *Phys. Rev. B*, 86:121102, September 2012.

[278] D. Z. Metin and N. Gaston. Internal and External Pressure in Cubic Perovskites: Electronic Structure Effects and Systematic Accuracy from First Principles. *Electronic Structure*, 1(3):035001, July 2019. https://doi.org/10.1088%2F2516-1075%2Fab2833.

[279] J. P. Perdew and Y. Wang. Accurate and Simple Analytic Representation of The Electron-Gas Correlation Energy. *Phys. Rev. B*, 45:13244–13249, June 1992. https://link.aps.org/doi/10.1103/PhysRevB.45.13244.

[280] M. Jong, W. Chen, T. Angsten, A. Jain, R. Notestine, A. Gamst, M. Sluiter, C. Krishna, C. K. Ande, S. Zwaag, J. Plata, C. Toher, S. Curtarolo, G. Ceder, K. Persson, and M. Asta. Charting The Complete Elastic Properties of Inorganic Crystalline Compounds. *Scientific Data*, 2, 03 2015.

[281] M. Rahman, M. Rahaman, and M. A. Rahman. The Structural, Elastic, Electronic and Optical Properties of MgCu under Pressure: A First-Principles Study. *International Journal of Modern Physics B*, 30, 10 2015.

[282] T. Katsura and Y. Tange. A Simple Derivation of the Birch–Murnaghan Equations of State (EOSs) and Comparison with EOSs Derived from Other Definitions of Finite Strain. *Minerals*, 9(12), 2019. https://www.mdpi.com/2075-163X/9/12/745.

[283] S. Boucetta. Theoretical Study of Elastic, Mechanical and Thermodynamic Properties of MgRh Intermetallic Compound. *Journal of Magnesium and Alloys*, 2(1):59 – 63, 2014.

[284] J. Mistrik, S. Kasap, H. E. Ruda, C. Koughia, and J. Singh. *Optical Properties of Electronic Materials: Fundamentals and Characterization*, pages 1–1. Springer International Publishing, Cham, 2017.

[285] L. Huang and W. R. L. Lambrecht. Electronic Band Structure Trends of Perovskite Halides: Beyond Pb and Sn to Ge and Si. *Phys. Rev. B*, 93:195211, May 2016. https://link.aps.org/doi/10.1103/PhysRevB.93.195211.

[286] S. Kondo, T. Sakai, H. Tanaka, and T. Saito. Amorphization-Induced Strong Localization of Electronic States in $CsPbBr_3$ and $CsPbCl_3$ Studied by Optical Absorption Measurements. *Phys. Rev. B*, 58:11401–11407, November 1998.

[287] M. Roknuzzaman, K. Ostrikov, H. Wang, A. Du, and T. Tesfamichael. Towards Lead-Free Perovskite Photovoltaics and Optoelectronics by Ab-Initio Simulations. *Scientific Reports*, 7:14025, 10 2017.

[288] T. Zhang, M. I. Dar, G. Li, F. Xu, N. Guo, M. Grätzel, and Y. Zhao. Bication Lead Iodide 2D Perovskite Component to Stabilize Inorganic α-$CsPbI_3$ Perovskite Phase for High-Efficiency Solar Cells. *Science Advances*, 3(9), 2017.

[289] T. Krishnamoorthy, H. Ding, C. Yan, W. L. Leong, T. Baikie, Z. Zhang, M. Sherburne, S. Li, M. Asta, N. Mathews, and S. G. Mhaisalkar. Lead-Free Germanium Iodide Perovskite Materials for Photovoltaic Applications. *J. Mater. Chem. A*, 3:23829–23832, 2015.

[290] L. Peedikakkandy and P. Bhargava. Composition Dependent Optical, Structural and Photoluminescence Characteristics of Cesium Tin Halide Perovskites. *RSC Adv.*, 6:19857–19860, 2016.

[291] S. Yalameha, P. Saeidi, Z. Nourbakhsh, A. Vaez, and A. Ramazani. Insight into The Topological Phase and Elastic Properties of Halide Perovskites $CsSnX_3$ (X = I, Br, Cl) under Hydrostatic Pressures. *Journal of Applied Physics*, page 85102, 02 2020.

[292] P. Pitriana, T. Wungu, R. Hidayat, and H. Herman. Ab-Initio Calculation of $APbI_3$ (A=Li, Na, K, Rb and Cs) Perovskite Crystal and Their Lattice Constants Optimization using Density Functional Theory. *Journal of Physics: Conference Series*, 1170:012023, 03 2019.

[293] R. Thompson and W. (Bill) Clegg. Predicting Whether A Material is Ductile or Brittle. *Current Opinion in Solid State and Materials Science*, 22, 04 2018.